Search for New Physics in Signatures of Soft Unclustered Energy Patterns with the ATLAS Detector

Dissertation an der Fakultät für Physik
der
Ludwig–Maximilians–Universität München

vorgelegt von
Alexander Mario Lory
aus Zürich

München, den 23.08.2022

Erstgutachter: PD Dr. Sascha Mehlhase
Zweitgutachter: Prof. Dr. Thomas Kuhr
Tag der mündlichen Prüfung: 13.10.2022

Zusammenfassung

Typischerweise wird an Teilchenbeschleunigerexperimenten nach neuer Physik in Endzuständen gesucht, die eine kleine Anzahl an hochenergetischen Teilchen beinhalten. Soft Unclusted Energy Patterns (SUEPs) sind Endzustände, die aus einer sehr hohen Anzahl von sphärisch verteilten, niederenergetischen Teilchen bestehen und sind charakteristisch für stark wechselwirkende, quasi-konforme Hidden Valley Modelle.

Die Analyse solch einer Signatur aus den Protonenkollisionen des Large Hadron Collider (LHC) ist herausfordernd, da sie dem diffusen Hintergrund ähnelt, der von der Vielzahl simultan stattfindenden Streuungen stammt, die in jedem Kollisionsereignis vorhanden sind. Zudem sind die Detektoren am LHC nicht dafür optimiert Objekte unterhalb eines bestimmten Impulsbereiches zu rekonstruieren. Jedoch bietet diese Signatur eine Möglichkeit nach neuer Physik in bislang wenig untersuchten Bereichen des kinematischen Phasenraums zu suchen.

In dieser Arbeit wird eine Suche nach neuer Physik in SUEP-Signaturen mit Myonen im Endzustand vorgestellt. Die Suche analysiert einen Datensatz von 139 fb^{-1} Proton-Proton-Kollisionen mit 13 TeV Schwerpunktsenergie, der mit dem ATLAS-Detektor am LHC aufgenommen wurde. Die Suche verspricht Sensitivität auf Signalmodelle mit Mediatormassen von 125 GeV, 400 GeV und 750 GeV mit Produktionswirkungsquerschnitten größer als 32 fb, bzw. 0.6 fb und 0.04 fb zu gewähren.

Zusätzlich werden Studien zu einer Analyse basierend auf rekonstruirten Clustern im Pixeldetektor vorgestellt. Diese verspricht Sensitivät auf Signalmodelle zu gewähren, deren Endzustände mehrheitig aus Teilchen mit so niegrigen Impulsen bestehen, dass diese nicht einmal rekonstruirbare Spuren im inneren Detektor produzieren.

Abstract

Most searches for new physics at collider experiments target final states containing a small number of high-momentum particles. A Soft Unclusted Energy Pattern (SUEP) is a signature of very high multiplicity of spherically distributed, soft objects, which can arise from strongly coupled, quasi-conformal Hidden Valley models.

The analysis of such a signature in proton–proton collision data at the Large Hadron Collider (LHC) is a challenge, as it resembles the diffuse background coming from the multitude of simultaneous hadronic interactions occurring in each collision event. Furthermore, the detectors at the LHC are not optimised for the reconstruction of objects with very small momenta. However, these signatures offer an opportunity to probe new physics in regions of the kinematic phase space not explored by collider searches so far.

In this thesis, a search for new physics in signatures of SUEPs containing muons in the final state is presented. The search analyses 139 fb^{-1} of proton–proton collisions at 13 TeV centre-of-mass energy, recorded with the ATLAS detector at the LHC. The search is expected to provide sensitivity to signal models with mediator masses of 125 GeV, 400 GeV and 750 GeV for cross-sections down to 32 fb, 0.6 fb and 0.04 fb, respectively.

In addition, preliminary studies for a pixel-cluster based search are presented. This search targets final states composed primarily of particles whose momenta are too low to even produce reconstructable tracks in the inner detector.

To my beloved wife Katrin.

Contents

Introduction

The Large Hadron Collider (LHC) has allowed for great progress to be made in particle physics during the last thirteen years. Most notably, the proton–proton (pp) collisions recorded by the ATLAS and CMS collaborations led to the discovery of the Higgs boson in 2012 [1, 2], a central piece of the Standard Model (SM) of particle physics. Many other measurements validated the predictions made by the SM and determined its parameters with great precision [3]. However, the SM is generally considered as incomplete, as it lacks a description of Dark Matter (DM) and gravity, and the mass of the Higgs boson can be regarded as unnatural [4]. Besides confirming the predictions of the SM through high-precision measurements and observations of rare processes, another main goal of the LHC is to probe extensions of the SM that address the issues mentioned above. Many of these extensions include new particles with masses at or above the weak scale. Both these new particles and the heavy particles of the SM tend to decay into final-state objects of high momentum, typically in the range of $10 - 100$ GeV. The design of the ATLAS detector was naturally guided towards the detection of these objects. For example, the magnetic field in the tracking detectors is very strong in order to bend the trajectory of charged particles as much as possible and therefore increase the precision with which their momentum can be measured. Today, large portions of the parameter spaces of many of the popular extensions of the SM have been probed, without evidence for new physics (see e.g. Ref. [5] for the status of searches for supersymmetry). However, evidence for new physics might be there, yet in an unexpected form. In order to make the most out of the data, it is important to know what kind of signatures new physics might manifest itself in and which of these signatures are possible to probe at the LHC.

Hidden Valley (HV) models [6] extend the SM by a gauge group that is hidden to the SM and includes new light states and a multi-particle production mechanism. They have been found to lead to a plethora of striking, exotic signatures at the LHC [7–11], for which new search strategies have been – or still need to be – developed. Strongly coupled HV models are well motivated: A strongly self-interacting particle in a hidden sector is a viable DM candidate and even fits rotational curves of galaxies and small-scale galactic structures better than the collisionless Cold Dark Matter (CDM) envisioned by the standard model of cosmology [12]. Besides appearing naturally in string theory models [13], HV models can also be incorporated into other popular extensions of the SM [14–16]. Their presence might hide one of the typically expected signatures of supersymmetry, missing energy [17], making HV models even more important to consider.

A Soft Unclusted Energy Pattern (SUEP) [18] is a signature of a very high multiplicity ($10 - 1000$) of objects of very low momenta ($0.1 - 10$ GeV) that are spherically distributed in the reference frame of the collision. They can arise from a strongly coupled HV model whose dynamics are inspired by those of low-energy quantum chromodynamics (QCD). Hadrons produced in particle

collisions at centre-of-mass energies $\sqrt{s} \lessapprox 5$ GeV are spherically distributed [19] and their momentum follows a Maxwell–Boltzmann distribution [20]. This behaviour was found to be a generic feature of gauge theories with a strong coupling in the non-perturbative regime [20]. Therefore, it would also be expected – at LHC centre-of-mass energies – from a gauge group that has a coupling that remains strong up to that scale. If, additionally, the coupling is close to scale invariant and the hadronisation scale is low, the shower is expected to produce a high multiplicity of soft objects. SUEPs might therefore be produced at the LHC if such a gauge group exists in a HV. Such signal models have not yet been probed at collider experiments. The main goal of the work presented in this thesis is to explore to which extent this is possible in the pp collisions recorded with the ATLAS detector during Run 2.

Detecting a SUEP is challenging. Triggers and object-reconstruction algorithms commonly used at ATLAS are not efficient for the low momenta of the final-state particles involved. These might not even traverse much of the detector as they can be trapped in its magnetic fields. Moreover, all SM events are themselves flooded with low-momentum particles stemming from QCD showers occurring simultaneously at multiple interaction vertices. However, depending on the nature of the particles composing the SUEP and on the particle multiplicity and momentum distribution, several search strategies can be envisioned. If the final state contains muons and if their momentum is above a couple of GeV, a muon-based search strategy, which is the main subject of this thesis, is possible.

The muon-based search presented uses a multi-muon trigger at the lower end of its momentum acceptance, a muon reconstruction algorithm optimised for low momenta and an event selection targeting high muon and track multiplicities. The tag-and-probe technique is used to measure trigger efficiencies. The contribution from pile-up interactions to the track multiplicity is studied thoroughly and corrected for. One of the unique features of the search is the inclusion of a selection requiring the momenta of the muons to be low. As a result, the background is composed of processes that have been of little interest for most analyses in ATLAS so far and the statistics of existing background simulations are low. Furthermore, the dominant background is the QCD-induced production of jets, which is is difficult to model accurately at the LHC [21]. Therefore, a data-driven approach, the ABCD-method [22], is used to estimate the background. Signal leakage in the regions designed to accept mostly background events is accounted for by using a likelihood-based approach to the ABCD-method. As this is a novel search, no region of the signal parameter space has yet been excluded. Therefore, the variety of signal models in which new physics might be found is high. In order to cope with the diversity of targeted signal models, an incremental unblinding strategy that successively probes parts of the phase space is proposed.

The thesis is structured as followed: In Chapter 1, a brief overview of the SM is given, the theoretical landscape around HV models is presented, and the considerations motivating SUEP signal models are given. In Chapter 2, the experimental setup is presented and in Chapter 3, the main aspects of the methodology are introduced. In Chapter 4, the muon-based search is presented. The results of this search are discussed in Chapter 5. Finally, preliminary studies on a potential search that uses pixel-cluster multiplicity as a discriminating variable are presented in Chapter 6.

Chapter 1

Theory

1.1 The Standard Model of particle physics

The Standard Model (SM) [23, 24] of particle physics describes the fundamental constituents of the Universe and their interactions. The fundamental interactions relevant on small scales are the electromagnetic, the strong and the weak interactions. In the SM, the particles that make up matter are spin-$\frac{1}{2}$ fermions and interactions between them are described by the exchange of spin-1 gauge bosons. Table 1.1 shows the list of known fermions in the SM together with their masses and electric charges. They can be grouped into quarks, that take part in strong interactions, and leptons, that do not. All fermions are affected by weak interactions and only neutrinos are not affected by electromagnetic interactions. Fermions can also be grouped in three generations, which are copies of each other, but with different masses. This pattern is not explained by the SM, as the particle masses are free parameters of the theory. Table 1.2 shows the relevant forces of the SM and their corresponding gauge bosons. The photon (γ) mediates electromagnetic interactions, eight gluons (g) mediate strong interactions and the W^+, W^- and Z bosons mediate weak interactions. The gauge bosons of the weak interaction are the only massive ones, resulting in the short range of the interaction. Strong interactions are also short-ranged, but in that case, as discussed in more detail in Section 1.1.3, the cause is gluon self-interactions. Weak and electromagnetic interactions can only be described consistently in a unified theory of *electroweak interactions* [25]. The mass of the fundamental particles of the SM is caused by the non-vanishing vacuum expectation value of the only elementary scalar field of the SM, the Higgs field. This mechanism, called Brout–Englert–Higgs mechanism [26, 27], also hides the gauge symmetry that describes electroweak interactions. Since gravity is extremely weak on the scales of elementary particles compared to the other interactions, its fundamental interactions have not yet been observed.

Table 1.1: Fermions in the SM with their masses and electric charges [28]. Upper limits on electron and muon neutrino masses at 90% Confidence Level (CL) and tau neutrino at 95% CL.

	Leptons				Quarks			
Generation	Particle		Charge	Mass (GeV)	Particle		Charge	Mass (GeV)
1	electron	(e^-)	-1	0.51×10^{-3}	down	(d)	$-1/3$	4.67×10^{-3}
	neutrino	(μ_e)	0	$< 1.1 \times 10^{-9}$	up	(u)	$+2/3$	2.16×10^{-3}
2	muon	(μ^-)	-1	0.106	strange	(s)	$-1/3$	0.093
	neutrino	(ν_μ)	0	$< 0.19 \times 10^{-3}$	charm	(c)	$+2/3$	1.27
3	tau	(τ^-)	-1	1.78	bottom	(b)	$-1/3$	4.18
	neutrino	(ν_τ)	0	< 0.018	top	(t)	$+2/3$	173

Table 1.2: Forces and associated gauge bosons in the SM with their masses [28].

Force	Gauge boson(s)		Charge	Mass (GeV)
Strong	gluons	(g)	0	0
Electromagnetic	photon	(γ)	0	0
Weak	W bosons	($W^\pm$)	± 1	80.4
	Z boson	(Z)	0	91.2

1.1.1 Theoretical description

From a theoretical point of view, the SM is a set of gauge quantum field theories (QFTs) [29]. QFT unifies quantum mechanics and special relativity by describing nature's fundamental objects with fields, and particles as disturbances in the fields. A field theory can be described with the expression of a Lagrangian density $\mathcal{L}(\phi, \partial_\mu)$ that depends on the fields ϕ and their spacetime derivatives. The equations of motion for each field are given by the Euler–Lagrange equations:

$$\partial_\mu \left(\frac{\partial \mathcal{L}}{\partial \left(\partial_\mu \phi_i \right)} \right) - \frac{\partial \mathcal{L}}{\partial \phi_i} = 0. \tag{1.1}$$

Unfortunately, in QFT, only a theory without interactions can be solved analytically and therefore, perturbative expansion is required to predict quantities like decay rates or interaction cross-sections. In perturbation theory, the transition matrix element is expanded into a polynomial of the coupling constant. Feynman diagrams and rules are an essential tool for visualising and computing the perturbative expansions. One diagram, representing one term of the expansion, is a set of propagators and interaction vertices that transform the initial state into the final state. Which vertices and propagators are allowed is defined by the Lagrangian of the theory. As an example, Figure 1.1(a) shows the leading-order diagram for the process $e^+e^- \to \mu^+\mu^-$ and Figure 1.1(b) one of several diagrams that contribute at the next order. A physical process can then be seen as the weighted sum of all allowed diagrams that lead to the desired final state. When a computation is done at the leading order (LO), only the diagram with the least vertices is considered. An additional vertex is considered at the next-to-leading order (NLO), two additional vertices are considered at the next-to-next-to-leading order (NNLO), and so on. For perturbation theory to be applicable, the contribution from higher orders is required to be small compared to the lower orders. Issues arise with diagrams including loops of particles, which is the case for the diagram shown in Figure 1.1(b). The momentum of the virtual particles in loops is arbitrary and therefore they contribute as integrals over momenta that diverge to infinity. Fortunately, the SM is renormalisable [30]. In a renormalisable theory, these diverging contributions can be absorbed into a redefinition of masses and coupling constants. As a result, the theory has a coupling constant that depends on the energy scale considered. The interaction strength of the physical process is then different from the unphysical, bare interaction strength used to describe the interactions between particles at a given order of perturbation theory.

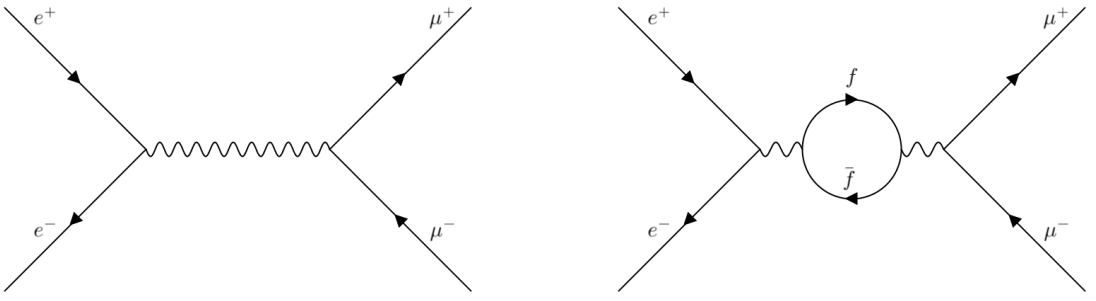

(a) Leading order diagram. **(b)** Higher order diagram. f represents any fermion.

Figure 1.1: Feynman diagrams of $e^+e^- \to \mu^+\mu^-$.

The SM is guaranteed to be renormalisable, if it is symmetric under local gauge transformations [30]. Local gauge invariance was introduced by Yang and Mills in 1954 as a generalisation of global gauge invariance [31] with the goal of describing strong interactions. It provides a common framework to describe the fundamental interactions in a unified way. In a gauge theory, instead of postulating interaction terms in a Lagrangian, they can be inferred from the requirement to be invariant under local gauge transformations within an abstract symmetry group. The symmetry group of the SM is

$$\mathrm{SU}(3) \times \mathrm{SU}(2) \times \mathrm{U}(1),$$

which is the convolution of the Lie groups of SU(3), that generates quantum chromodynamics (QCD), and $\mathrm{SU}(2) \times \mathrm{U}(1)$ that generates electroweak interactions.

In order to illustrate how local gauge invariance holds, it helps to consider the free fermionic fields first. These obey the free-particle Dirac equation [32]:

$$i\gamma^\mu \partial_\mu \psi = m\psi\,, \tag{1.2}$$

in which ψ is a four-component wave function called Dirac spinor and, in Dirac–Pauli representation,

$$\gamma_0 = \begin{pmatrix} \mathbb{1}_2 & 0 \\ 0 & -\mathbb{1}_2 \end{pmatrix} \quad \text{and} \quad \gamma_i = \begin{pmatrix} 0 & \sigma_i \\ -\sigma_i & 0 \end{pmatrix}, \tag{1.3}$$

where σ_i are the Pauli spin-matrices.

Applying the U(1) local phase transformation $\psi \longrightarrow \psi' = e^{iq\phi(x)}\psi$, the Dirac equation is transformed to

$$i\gamma^\mu(\partial_\mu + iq\partial_\mu\phi(x))\psi = m\psi\,, \tag{1.4}$$

which is different from the original Equation 1.2. But when adding an interaction term

$$q\gamma^\mu A_\mu \psi\,, \tag{1.5}$$

the Dirac equation becomes

$$i\gamma^\mu(\partial_\mu + iqA_\mu)\psi = m\psi\,, \tag{1.6}$$

which is invariant under local phase transformations if A_μ transforms as

$$A_\mu \longrightarrow A'_\mu = A_\mu - \partial_\mu\phi(x) \tag{1.7}$$

simultaneously. The required term 1.5 corresponds to the interaction term of QED, where A_μ is the four-potential describing an electromagnetic field. This shows that electromagnetic interactions are tied to U(1) local phase transformations.

It should be noted that local gauge invariance is spoiled if gauge bosons have mass. Indeed, a massive vector field is described by the Proca Lagrangian:

$$\mathcal{L}_{\text{Proca}} = -\frac{1}{4}F_{\mu\nu}F^{\mu\nu} + \frac{1}{2}m_A^2 A_\nu^\nu, \tag{1.8}$$

in which the term A_ν^ν is not invariant under local gauge transformations.

1.1.2 Electroweak interactions

Two types of interactions take place in the weak sector: The Z boson can couple to a fermion and its anti-particle, leading to the flavour-conserving neutral current of the weak interactions. The $W^\pm$ bosons, on the other hand, couple to fermions of different fermion flavours, leading to flavour changing charged currents. The charged weak interactions only affect chirally left-handed particles and right handed anti-particles. The structure of weak interactions mentioned above suggest the construction of the weak isospin doublets

$$\begin{pmatrix}\nu_e\\ e\end{pmatrix}_L, \begin{pmatrix}\nu_\mu\\ \mu\end{pmatrix}_L, \begin{pmatrix}\nu_\tau\\ \tau\end{pmatrix}_L, \begin{pmatrix}u\\ d\end{pmatrix}_L, \begin{pmatrix}c\\ s\end{pmatrix}_L, \begin{pmatrix}t\\ b\end{pmatrix}_L,$$

such that the Pauli spin matrices generate the allowed transformations of the weak interactions within the $\mathrm{SU}(2)_L$ symmetry group; $\sigma_{1,2}$ generating flavour changing charged currents and σ_3 flavour-conserving neutral currents. All doublets have weak isospin $I = \frac{1}{2}$. By convention, the upper components of the doublets have the third component of the weak isospin $I_3 = \frac{1}{2}$ and the lower components $I_3 = -\frac{1}{2}$, such that I and I_3 are conserved. The chirally right-handed states, which are unaffected by charged weak interactions, are placed in weak isospin $I = I_3 = 0$ singlets

$$e_R,\ \mu_R,\ \tau_R,\ u_R,\ d_R,\ c_R,\ s_R,\ t_R,\ b_R.$$

The charged current of the weak interaction always couples leptons and neutrinos of the same generation, yet this is not the case for quarks, for which weak eigenstates are mixtures of the mass eigenstates. The relation between both can be expressed with the Cabbibo–Kobayashi–Maskawa matrix V_{CKM} that transforms down-type quarks of the weak eigenstates (labelled with a prime below) into down-type quarks of the mass eigenstates

$$\begin{pmatrix}d'\\ s'\\ b'\end{pmatrix} = V_{\text{CKM}}\begin{pmatrix}d\\ s\\ b\end{pmatrix} \tag{1.9}$$

Three quark mixing parameters and one CP-violating phase are necessary to describe the mixing. These are free parameters that have to be determined experimentally.

Weak and electromagnetic interactions can be treated in a unified model of electroweak interactions [25] with a gauge group $\mathrm{SU}(2)_L \times \mathrm{U}(1)_Y$. $\mathrm{SU}(2)_L$ local gauge transformations require three (massless) gauge fields W_μ^1, W_μ^2 and W_μ^3 and U_Y one gauge field B_μ, which couples to the hypercharge $Y = 2(Q - I_3)$, where Q is the electric charge.

In the presence of an additional complex doublet scalar field, called Higgs field, with a potential

$$V(\phi) = \mu^2(\phi^\dagger\phi) + \lambda(\phi^\dagger\phi)^2, \tag{1.10}$$

where $\mu^2 < 0$, the Brout–Englert–Higgs mechanism [26, 27] hides the electroweak gauge symmetry. As a result, the physical gauge bosons of the electroweak sector, the photon A, $W^\pm$ and Z bosons are linear combinations of the gauge bosons of the electroweak symmetry:

$$\begin{aligned} A_\mu &= +B_\mu \cos\theta_W + W^3_\mu \sin\theta_W, \\ Z_\mu &= -B_\mu \sin\theta_W + W^3_\mu \cos\theta_W, \\ W^\pm_\mu &= \frac{1}{\sqrt{2}}(W^1_\mu \mp iW^2_\mu), \end{aligned} \tag{1.11}$$

where θ_W is the Weinberg angle, and the $W^\pm$ and Z bosons acquire mass by absorbing the degenerate degrees of freedom of the Higgs field.

1.1.3 Quantum Chromo Dynamics

The theory of QCD [33, 34] describes the strong interactions based on the gauge group SU(3). QCD acts on the colour quantum number, which can take three values. In contrast to weak interactions, the SU(3) gauge symmetry is non-chiral and unbroken. As a results, the eight gauge bosons of the theory, called gluons, are massless. QCD being non-abelian, the gluons themselves also carry colour charge and therefore interact with themselves.

As in the electroweak sector, terms of the perturbative expansion containing loops are divergent and regularisation and renormalisation allows for them to be absorbed into a running coupling constant that depends on the normalisation scale. For all interactions in the SM, a fermion loop can enter the propagator describing the exchange of a gauge boson, resulting in a *screening* effect of the charge when looking at small momentum transfers or long distances. For interactions in abelian theories, loops of bosons can also enter the propagator. So besides the screening contributions, there are *anti-screening* contributions to the exchange of gauge bosons, as illustrated in Figure 1.2. The anti-screening contributions have the opposite effect of screening contributions. For a SU(3) theory with eight massless gauge bosons and six quark flavours, the anti-screening effect from gluons dominates over the screening effect from quarks, which leads to a running of the coupling that is opposite to that of weak interactions and QED.

Using the regularisation group equations to express an effective coupling running with the scale Q and with the boundary condition $\alpha_s(\Lambda^2) = \infty$, the running of the coupling at leading order becomes

$$\alpha(Q^2) = \frac{g_S^2}{4\pi} = \frac{12\pi}{(33 - 2N_f)\ln(\frac{Q^2}{\Lambda^2})}, \tag{1.12}$$

where N_f is the number of quark flavours [33]. Equation 1.12 shows that indeed strong interactions become stronger at lower momentum transfers. Below Λ, quarks are confined into colour

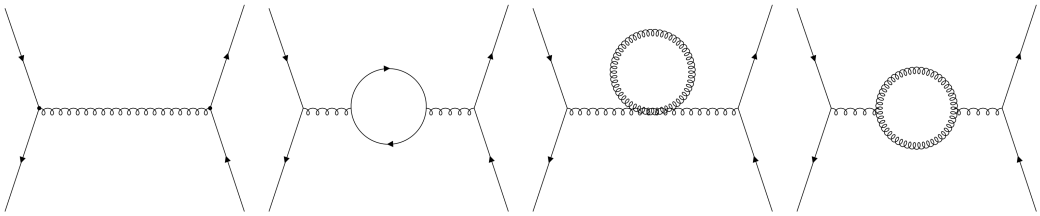

Figure 1.2: Diagrams contributing to a QCD interaction between quarks. Straight lines are quark propagators and curly lines gluon propagators. The first diagram from the left is the leading order contribution. The second diagram involves a quark loop and has a screening effect. The third and fourth diagrams involve a gluon loop and have an anti-screening effect.

singlet hadrons and alternatives to perturbation theory, like lattice QCD [35], are required. Conversely, strong interactions become weaker at high momentum. This asymptotic freedom [36] allows perturbation theory to be used to make predictions about the hard scattering event in a particle collision that produces partons (quarks or gluons) when the energy scale of the interaction is sufficiently above the scale of hadronisation.

A QCD process in a particle collision contains jets in the final state if the centre-of-mass energy of the collision is high compared to the hadronisation scale [19]. Qualitatively, the formation of jets involves the production of asymptotically free quarks in the hard scattering process that have high relative velocities and, as the distance between them increases, the increasing energy of the colour field connecting them leads to the formation of new quark pairs. This process repeats until the relative velocities between all partons are sufficiently low for them to combine into hadrons. The quantitative description of jets is complicated since it involves the transition from the scale of asymptotically free partons to the scale of confined ones. However, from a perturbative calculation it can be shown that radiation of gluons from asymptotically free quarks is enhanced for soft or colinear radiation, which gives an explanation for the formation of jets.

Jets are not formed in collisions below approximately 5 GeV of centre-of-mass energy. This is illustrated by the sphericity distribution of $ee \rightarrow$ hadrons events recorded by the SLAC-LBL magnetic detector at the SPEAR storage ring of the Stanford Linear Accelerator Center, shown in Figure 1.3. The event sphericity is an event-shape observable that uses the momenta of all final state particles in the event and is defined such that it approaches 0 for events in which all particles are colinear and 1 for completely isotropic events. As shown in Figure 1.3, the event shape of $ee \rightarrow$ hadrons differs from an isotropic phase-space model for collisions at 6.2 or 7.4 GeV, but not for collisions at 3 GeV centre-of-mass energy.

Another interesting feature of hadron production is that the momenta of hadrons produced in a shower follow a Maxwell-Boltzmann distribution with a Hagedorn temperature of about ~ 160 MeV [37]. This behaviour is predicted by the statistical hadronisation model, first developed by Fermi in 1950 [38] and adapted by Hagedorn in 1965 [39]. In this model, extended clusters are produced in particle collisions which decay into multihadronic states and all multihadronic states within the cluster compatible with its quantum numbers are equally likely. The reason for the apparent equilibrium between hadrons is unknown [40]. However, using a correspondence between anti-de Sitter space and conformal field theory (AdS/CFT correspondence) [41], it can be shown that this thermal behaviour is a generic feature of strong coupling dynamics of gauge theories in the non-perturbative regime [20].

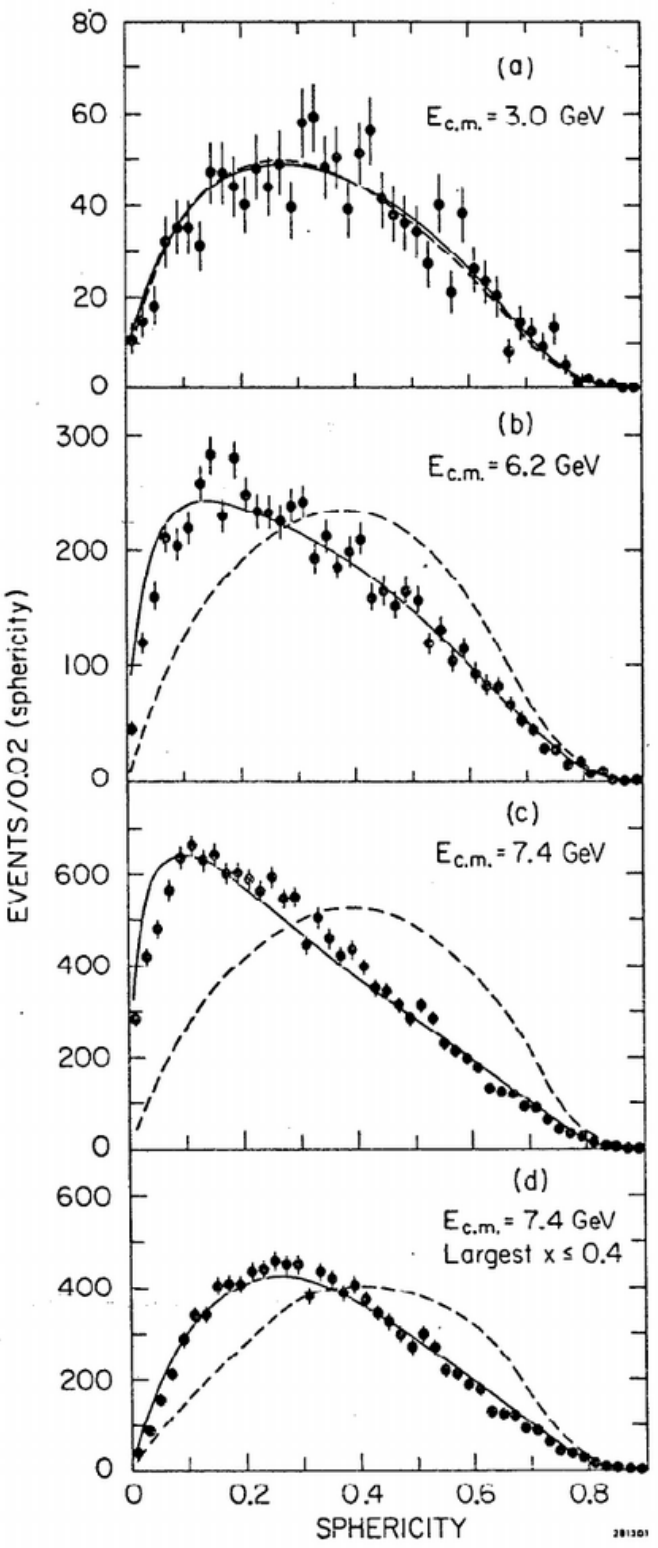

Figure 1.3: Observed sphericity distributions for data, jet model (solid lines), and phase-space model (dashed lines) for various centre-of-mass energies of $e^+e^- \rightarrow$ hadrons events recorded with the SLAC-LBL magnetic detector at the SPEAR storage ring of the Stanford Linear Accelerator Center [19].

1.2 Shortcomings of the Standard Model

Although the SM successfully describes interactions between elementary particles with high precision, it has several shortcomings. First of all, it does not describe gravity. To date, there is no data against which one could test a theory of quantum gravity, which is believed to become relevant at the Planck scale $m_p \approx 10^{19}$ GeV [42]. However, to describe all fundamental forces, the SM will have to include gravity. The immense gap between the Planck scale and the scale of electroweak interactions is a concern in itself. The Higgs boson receives corrections to its bare mass from loops in its propagator which are at least proportional to the scale at which new physics would become relevant. In this light, the Higgs mass of 125 GeV is not natural, as it requires a lot of fine-tuning to cancel $\mathcal{O}(10^{19}$ GeV) contributions.

Furthermore, some measurements are in significant tension with SM expectations. Several B-physics measurements indicate that the lepton flavour universality predicted by the SM might not always hold [43]. The muon $g-2$ experiment at the Fermi National Accelerator Laboratory (FNAL) [44] measured the anomalous magnetic moment of the muon with a very high precision. Their result deviates by 3.3 σ from the SM expectation. Recently, the Collider Detector at Fermilab (CDF) collaboration published a new measurement of the W-boson mass based on data from the Tevatron collider, which shows a 7 σ deviation from the SM expectation [45].

Finally, the SM does not explain the presence of Dark Matter (DM), which is discussed in the next section.

1.2.1 Dark Matter

Since Zwicky's postulation of DM in 1933 [46], with which he explained the discrepancy between the observed and predicted rotation curves of galaxies in the Coma cluster, the evidence for the presence of such non-luminous matter in the Universe fortified through a long series of observations. Besides the rotation curves, the velocity dispersion of elliptical galaxies does not match their light-to-mass ratios [47] and the gravitational lensing of some galaxy clusters is too strong to be explained by the luminous matter they contain [48, 49]. Moreover, DM is needed to explain the formation of the large-scale structures in the Universe [50].

If DM is a particle, its coupling to other particles is required to be weak and it is required to be stable on cosmological time scales. The only candidate fulfilling these requirements in the SM is the neutrino. Non-zero neutrino masses are required to explain their flavour oscillations [51], but the upper limit on their masses is too low for them to explain the clustering scale of galaxies [52]. The Cold Dark Matter (CDM) hypothesis states that the velocity of DM particles in the early Universe was sufficiently small for galactic structure to remain intact. CDM was shown to be compatible with observed anisotropies in the cosmic microwave background [53] and the formation of galaxies [54] and galaxy clusters [55]. In this scenario, structure in the Universe today is a preserved structure from fluctuations in the early Universe. Together with a description of gravity by general relativity [56] with a cosmological constant Λ, the assumptions of a flat, isotropic and homogeneous Universe and a primordial phase of cosmic inflation [57], these hypotheses form the ΛCDM model [58], which is considered as the standard model of cosmology. The density of DM can be inferred from the cosmic-microwave-background anisotropies [59].

According to ΛCDM, the Universe is composed of about 69% Dark Energy, 26% DM and 5% baryonic matter.

The most prominent candidate for CDM are weakly interacting massive particles (WIMPs), which are massive non-composite particles that only interact weakly. If DM is a thermal relic, then the abundance of DM today is given by its self-annihilation cross-section [60] and it just so happens that the correct cross-section is obtained for a weak interaction coupling strength and a DM mass of 100 – 1000 GeV, which is the scale of electroweak symmetry breaking [61] and is relevant in many extensions of the SM, e.g. supersymmetry [62]. This *WIMP miracle* is another further motivation for CDM. However, CDM is in tension with simulations of small-scale structures in the Universe, which show that the shape of CDM halos in galaxies is expected to be *cuspy*, i.e. the mass density is expected to peak at the centre of the galaxy [63]. Observations of rotation curves, however, favour constant-density cores. Moreover, in a CDM scenario, DM halos are expected to exhibit a large amount of sub-structure, but the number of sub-halos observed in the Milky Way halo does not match the amount obtained from simulation [64].

One way of addressing these issues is to assume DM is warm, i.e. that its velocity in the early Universe was sufficiently large to erase some of the structure [65]. However, the suppression of small scale structure does not fit well with the observations of the Lyman-α forest, which sets strong limits on the mass of warm DM [66].

Better agreement is achieved with Strongly-Interacting Dark Matter (SIDM). Theories of SIDM state that, while DM interacts weakly with the SM, it interacts strongly with itself. SIDM can lead to the correct DM halo density profile, while the large-scale behaviour is similar to CDM and therefore is in good agreement with observations [12]. If DM interacts strongly with itself, then a new force, that doesn't affect the SM, is required in the dark sector to mediate that interaction.

Besides SIDM, there is another argument that motivates a DM sector with an additional force. In the WIMP-paradigm, DM is a relic from a freeze-out process and baryonic matter is produced in baryogenesis [67]. Since these two mechanisms are unrelated, it is quite surprising to observe that the DM and baryonic matter densities, Ω_{DM} and Ω_{B}, are of the same order of magnitude ($\Omega_{\mathrm{DM}} \approx 5\Omega_B$). This is either a coincidence or suggests that their densities are related in another way. Another approach is given by the *asymmetric dark matter* [68] hypothesis, in which it is assumed that the matter–anti-matter asymmetry we observe for ordinary matter is shared between dark and baryonic matter, which would lead both to have similar number densities. In that case, the masses of dark (m_{DM}) and baryonic matter particles should also be similar. Such theories require a mechanism which effectively annihilates the symmetric part of DM. This can be achieved with a new dark force. Since the mass of the proton m_p is given by the QCD confinement scale, $m_{\mathrm{DM}} \simeq 5m_p$ is obtained in a straightforward way if there is a force similar to QCD in the dark sector [69].

1.3 Hidden Valley Models

As discussed in Section 1.2.1, the possibility that a more complex hidden sector is associated with DM deserves our attention. Such hidden sectors are further motivated by their appearance in theories that try to solve the naturalness problem of the Higgs-boson mass [14–16] and in string-theory models [13].

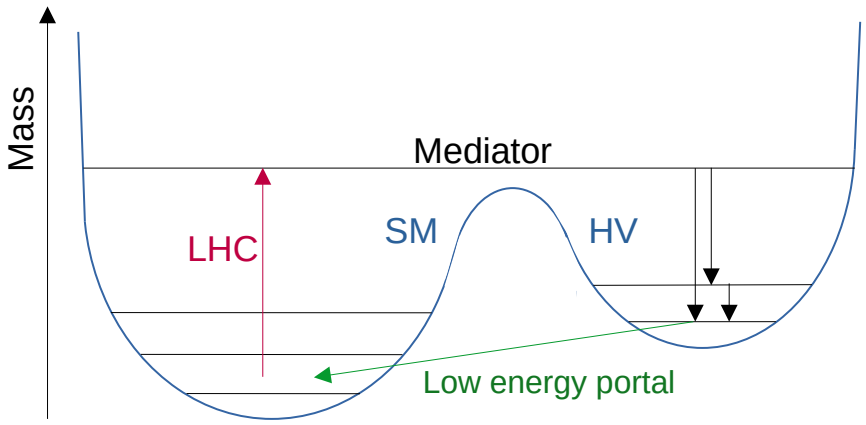

Figure 1.4: Schematic description of a hidden valley model.

A hidden sector translates to a Hidden Valley (HV) [6] in the context of collider physics, if the hidden sector is accessible at collider experiments and if the hidden sector contains light new states. HVs extend the SM by an additional gauge group, which is neutral under the SM. The SM itself is also neutral under the new gauge group. The HV contains a spectrum of new particles, of which the lightest typically have masses of the order $\mathcal{O}$(1 GeV) and are stable within the HV gauge group. The HV, schematically described in Figure 1.4, can be accessed through a heavy mediator of mass $\mathcal{O}$(TeV), which is assumed to be produced at an appreciable rate at the LHC. The mediator can be a known SM particle, like the Higgs, W, or Z boson, or a new particle like a Z' [70]. Decays in the HV then distribute the available energy to the particles at the bottom of the HV spectrum, which typically leads to a high multiplicity of soft particles in the final state. In the presence of a decay portal, the particles at the bottom of the HV can decay to the SM, promptly or at detector time scales, leaving a detectable signature. The decay portal may be induced by the same massive mediator that gives access to the HV, but various decay portals are possible and well motivated [71], each leading to potentially different final-state particle compositions.

While the final-state particle composition is dictated by the decay portal, the event shape of the signature is mostly dictated by the nature of the hidden gauge group. As discussed in Ref. [6], non-abelian confining HV models have a complex phenomenology that leads to a large variety of possible signatures. In the case of dark QCD, the HV would behave very similarly to the SM QCD and one could therefore expect the formation of jets in the HV. This can lead to a signature of jets whose constituents progressively decay from the HV to the SM as they propagate through the detector (*emerging jets* [7]). If part of the spectrum in the HV is stable and therefore invisible, *semi-visible jets* [8] might be formed. For HV models with hadronisation scales of $\gtrapprox$ 30 GeV, jets might be broader, more massive and composed of a higher multiplicity of particles than QCD jets [9].

Non-confining and abelian HV models and their phenomenology have been studied as well, for example, in a case which produces lepton-jets when DM radiates dark photons [10] or in the case

of *stealth supersymmetry*, in which the typical signature of missing energy in supersymmetry is significantly reduced due to the presence of a hidden sector [17].

The phenomenology of confining HVs might differ even more substantially to SM QCD than the cases above. An extreme example is *quirky* phenomenology [11], which occurs when the scale at which the coupling becomes strong is much smaller than the mass of the lightest hidden quark. In this case, pairs of *quirks* might be produced, that are bound to each other on macroscopic distances. If they are electrically charged, tracks that oscillate in tandem might be an observable signature. Another extreme case are soft unclustered energy patterns (SUEPs), which are the subject of this thesis.

1.3.1 The SUEP Case

A Soft Unclusted Energy Pattern (SUEP) [18], also called *soft-bomb*, is a signature of a very high multiplicity of very soft, spherically distributed particles. Such a signature can be produced by a confining HV whose coupling remains strong far above the hadronisation scale, which results in a large energy window for a showering process and a very high multiplicity of particles at the bottom of the HV. Qualitatively, as described by Strassler who introduced the idea in collider phenomenology [72], a coupling which is strong throughout the whole showering process would result in the radiation of dark gluons of a significant fraction of the initial parton's energy, without preferred directions. This is in contrast to QCD, in which soft and colinear gluon emissions are enhanced. In the SUEP case, the direction of the initial parton is lost and the final state is isotropic in the frame of reference of the mediator. [†] For this to occur, the coupling needs to remain in the non-perturbative regime throughout the shower and hadronisation process. This is achieved in a quasi-conformal theory, in which the coupling is nearly scale invariant. In this case, AdS/CFT correspondence can be used to infer some of the characteristics of the event, as discussed in Ref. [18]. In particular, it is expected that the average particle multiplicity should be approximately given by [73]

$$\langle n(Q)\rangle \propto \left(\frac{Q}{\Lambda}\right)^{1+\mathcal{O}(\lambda^{-\frac{1}{2}})} \tag{1.13}$$

for $\lambda \gg 1$, where Q is the scale of the hard process, Λ the hadronisation scale and $\lambda = g^2 N_c$ the 't Hooft coupling for N_c colours. It is also expected that the momenta of dark hadrons formed at the bottom of the HV follow a Maxwell-Boltzmann distribution

$$\frac{dN}{d^3\boldsymbol{p}} \propto e^{-\frac{\sqrt{\boldsymbol{p}^2+m^2}}{T}}, \tag{1.14}$$

where T, a generalised temperature [20], is expected to be of the order of m, the mass of dark hadrons formed by the dark shower.

[†] The mediator can be boosted in any direction due to initial state radiation (ISR) and additionally longitudinally due to an imbalance in the momenta of the colliding parton.

Chapter 2

Experiment

2.1 The Large Hadron Collider

The Large Hadron Collider (LHC) [74] is the world's largest particle accelerator. It is situated at the Centre Européen pour la Recherche Nucléaire (CERN), near Geneva, in a tunnel of 26.7 km circumference, in which the Large Electron Positron (LEP) accelerator previously was in operation. It can provide proton–proton (pp) and heavy-ion collisions. The LHC consists of two rings each hosting a beam of hadrons travelling in opposite direction. It is composed of eight straight and eight curved sections. Particle collisions can take place at one of the so-called *points* in the straight sections. The ATLAS (A Toroidal LHC ApparatuS) [75] detector is a multi-purpose detector situated at point 1. On the other side of the ring, at point 5, collisions take place at a second multi-purpose detector, CMS (Compact Muon Solenoid) [76]. LHCb (LHC beauty) [77], located at point 8, is an asymmetric detector designed to explore b-physics and ALICE (A Large Ion Collider Experiment), located at point 2, is specialised in heavy-ion physics. Three smaller experiments also use the LHC: TOTEM (Total Elastic and Diffractive Cross Section Measurement) [78] and LHCf [79] study forward physics and MoEDAL (The Monopole and Exotics Detector at the LHC) [80] searches for magnetic monopoles.

The main limiting factor for achieving high energies at the LHC is the strong magnetic field required to curve the trajectory of the beams. To obtain the 8.33 T required for an operation at 7 TeV beam energy, superconducting dipole magnets are used that are cooled to 1.4 K. Quadrupole magnets are used to keep the beams focused. Acceleration within the LHC is provided by radio-frequency cavities. This acceleration also groups the protons longitudinally in *bunches*, each containing approximately 10^{11} protons. Protons are required to be accelerated to 450 GeV before entering the LHC. The injection energy is obtained by using accelerators built for previous experiments. Figure 2.1 shows a schematic overview of the CERN accelerator complex. Protons are successively accelerated in LINAC 2 (Linear Accelerator 2) [†], in the Booster, the PS (Proton Synchrotron) and the SPS (Super Proton Synchrotron).

[†] LINAC 2 was replaced by LINAC 4 [81] for Run 3.

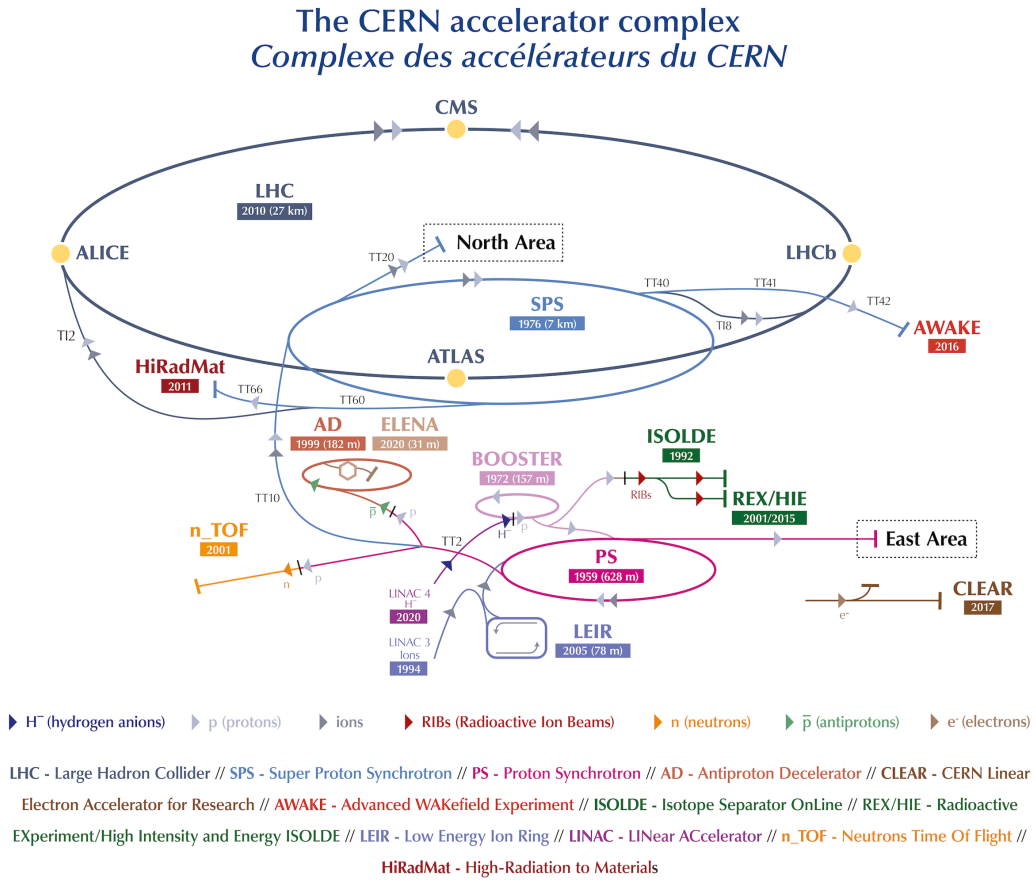

Figure 2.1: CERN accelerator complex. [82]

In order to quantify the amount of data delivered by a collider, the luminosity L is used. The total number of events N_i of a process i expected to occur in a given time-interval Δt is given by

$$N_i = \sigma_i L = \sigma_i \int_{\Delta t} L_{\text{inst}} \mathrm{d}t \,,$$

where σ_i is the cross-section of the process i, a measure of its probability to occur with units of surface and L_{inst} is the instantaneous luminosity, given by

$$L_{\text{inst}} = \frac{N_p^2 n_b f}{4\pi\sigma_x\sigma_y} F, \tag{2.1}$$

where N_p is the number of protons inside a bunch, n_b the number of bunches in each beam, which circulate in the LHC at frequency f, σ_x and σ_y are the transverse bunch sizes, and F a correction factor accounting for the geometry of the bunch crossing.

At ATLAS the luminosity measurement, described in more detail in Ref. [83], mainly relies on the measurement of the number of visible inelastic interactions per bunch crossing μ_{vis} done by Luminosity Cherenkov Integrating Detector 2 (LUCID-2) [84]. By monitoring μ_{vis}, relative variations of the luminosity can be determined. The absolute luminosity is determined by a measurement of the visible inelastic cross-section σ_{vis}, which is done in van der Meer (vdM) scans [85] during dedicated periods of data-taking at low luminosities.

The LHC operates in cycles called fills, lasting typically several hours to one day. In one fill, a dose of protons is accelerated through the accelerator complex and once the desired energy is reached, collisions are recorded by the detectors. During data-taking, the intensity of the beams gradually declines. After some time, the beams are dumped and a new fill starts. On longer time-scales, the LHC operates in *runs* separated by long shutdown periods used for maintenance and upgrades of both the detectors and accelerators. Run 1 [86], which operated at a centre-of-mass energy of $\sqrt{s} = 7$ TeV, began in 2009 and ended in 2013. The approximately 30 fb^{-1} delivered in this run allowed for, e.g., the discovery of the Higgs boson in 2012 by both ATLAS [1] and CMS [2]. Run 2 [83] comprised four years of data-taking between 2015 and 2018. During this period, ATLAS recorded 139 fb^{-1} of data at 13 TeV centre-of-mass energy. Figure 2.2 shows the growth of the integrated luminosity in Run 2. In total, 156 fb^{-1} were delivered by the LHC, of which 147 fb^{-1} were recorded by ATLAS and 139 fb^{-1} are deemed to be of sufficient quality to be used by physics analyses. The flat regions in Figure 2.2 correspond to shorter shutdown periods. During Run 3, which started in July 2022, the LHC operates at 13.6 TeV, a slight increase compared to Run 2. It will last until 2025 and deliver approximately 250 fb^{-1}. After Run 3 the LHC will be upgraded to operate at much higher instantaneous luminosities in order to deliver several thousands of fb^{-1} from 2029 to 2038 [87].

The crossing angle of the beams and the shape of the bunches lead to a Beam-Spot (BS) in the shape of an ellipsoid, in which the probability density of a collision occurring is maximal at the centre and gradually declines the larger the distance from the centre. This is illustrated by Figure 2.3, which shows the distribution of the position of reconstructed vertices in the transverse direction x and longitudinal direction z for one fill of the LHC.[†] As can be seen, collisions are restricted to a few mm in transverse direction from the centre, but occur for a

[†] The distribution along the y-direction is similar to that of the x-direction.

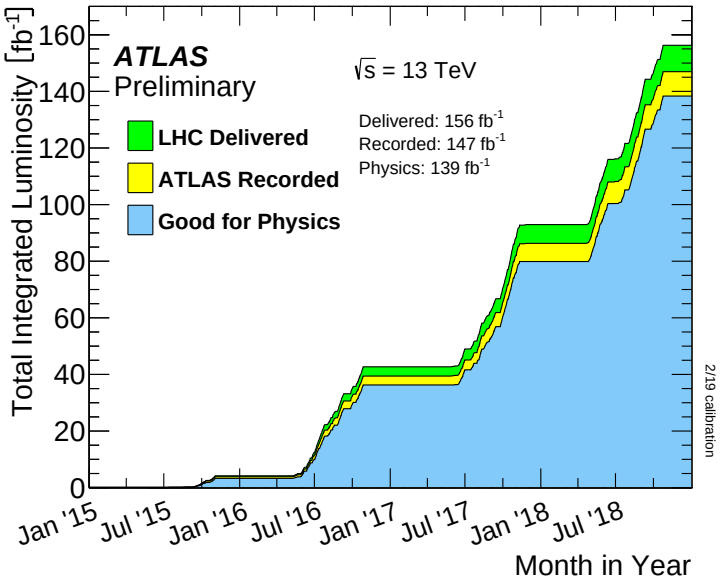

Figure 2.2: Integrated luminosity delivered by the LHC (green), recorded by ATLAS (yellow) and deemed of sufficient quality for physics analysis (blue) for Run 2. [88]

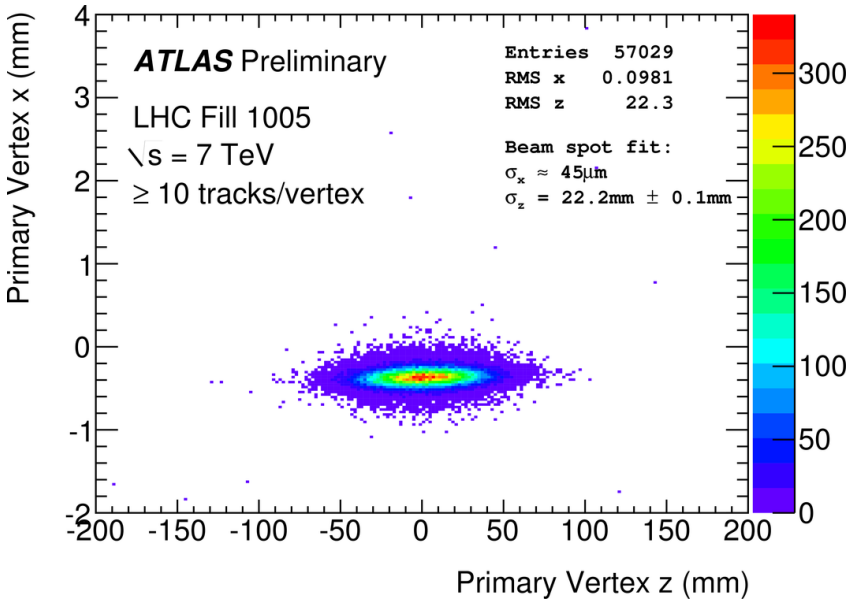

Figure 2.3: x–z-distribution of primary vertices with at least ten tracks, reconstructed by the High-Level Trigger (HLT) for one LHC fill at $\sqrt{s} = 7$ TeV. [89]

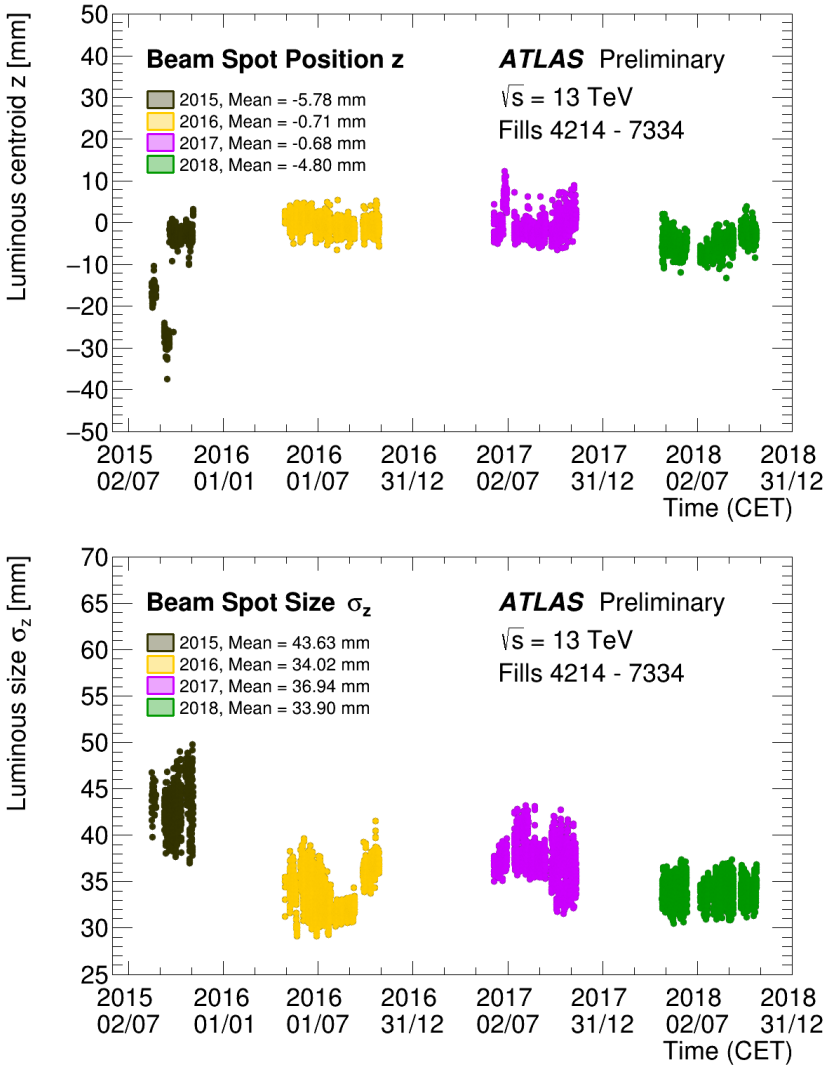

Figure 2.4: Position and size of the BS in z-direction over time. [89]

wide range of longitudinal positions. The parameters of the BS are monitored online by the HLT system, described in Section 2.2.5, and reported to the LHC control system every few minutes. Both the position and size of the BS vary over time due to varying beam conditions, which is illustrated in Figure 2.4 for the z-coordinate.

The vast majority of collisions occurring at the LHC are of low interest for most physics analyses. They consist mostly of elastic and inelastic QCD processes that involve relatively low momentum transfers. Physics analyses, however, are usually interested in events involving the production of heavy SM particles or new heavy states beyond the SM, which lead to final states including high-momentum particles or jets in most cases. The total elastic and inelastic cross-section for a pp-collision at 13 TeV is approximately 110 mb [90], while the cross-sections for the production of $W^{\pm}$ or Z bosons are $\mathcal{O}$(nb), which is eight orders of magnitude smaller.

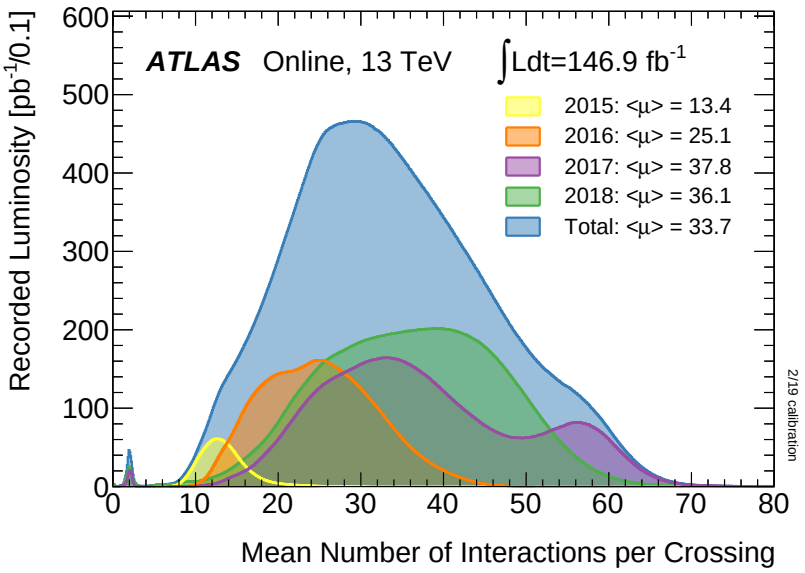

Figure 2.5: Luminosity-weighted distribution of the mean number of interactions per bunch crossing for Run 2. [88]

This has several consequences. In order to get statistically significant results for interesting processes, a high luminosity is required. This means that the detector has to withstand a high amount of radiation coming from all the unwanted scattering events. It also means that the data acquisition system, which is described in Section 2.2.5, has to filter out most events in order for the amount of stored data and computation power required to process the data to stay manageable. Finally, as a result of the high beam intensity required to obtain a high instantaneous luminosity, several collisions that are spread out within the BS usually take place simultaneously. An event therefore typically contains one collision of interest which fired a trigger and several other collisions which exhibit lower activity. This effect, called *in-time pile-up* [91], leads to events being filled with noise of low-momentum particles. Figure 2.5 shows the luminosity weighted distribution of the average number of interactions per bunch-crossing μ for the four years of data-taking of Run 2.

2.2 The ATLAS Experiment

The ATLAS detector [75, 92] illustrated in Figure 2.6 is a concentric, cylindrical multi-purpose detector of 44 m in length and 25 m in diameter. It nearly covers 4π of the solid angle surrounding the interaction point. It is required to provide measurements of high resolution while withstanding a high amount of radiation.

The detector can be divided into four main components. The Inner Detector (ID), directly surrounding the beam pipe, measures the path of charged particles inside a magnetic field. This allows tracks, that can be assigned to charged particles, to be reconstructed. The momentum of the particles is determined by measuring the curvature of the tracks. The high resolution of the tracking technology is especially crucial in the innermost layers of the ID, such that interaction

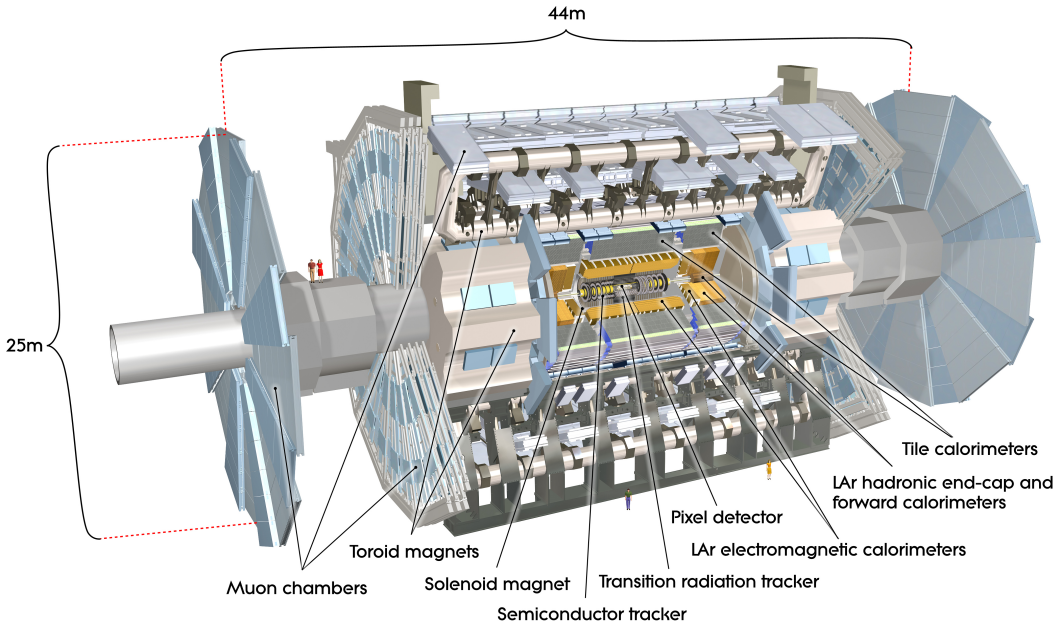

Figure 2.6: The ATLAS detector [93].

vertices can be resolved, which helps identifying displaced vertices arising from particles that decay on detector-scale lengths, like B mesons and τ leptons, and to reject tracks coming from pile-up interactions. The calorimeters, surrounding the ID, measure the energy of particles by inducing showering processes that dissipates their energy. Muons are minimal ionising particles and are therefore much less likely to be affected destructively by the calorimeters than photons, electrons or hadrons. In order to capitalise on that, the calorimeters are surrounded by a Muon Spectrometer (MS), which provides an additional momentum measurement and identification criteria for muons. The magnet system provides magnetic fields necessary for the momentum measurements in the ID and the MS. It is composed of a central solenoid, which provides the magnetic field for the ID, and toroidal magnets, which provide a magnetic field for the MS.

The detector is composed of two longitudinally symmetric halves that come together at the nominal interaction point. Due to the topology of the collisions, all subdetector systems have *barrel* and *end-cap* parts. The barrel parts, covering large deflection angles w.r.t the beams, are concentric cylinders surrounding the beam pipe. For smaller angles of deflection, the detector layers are installed in discs perpendicular to the beam pipe.

2.2.1 Coordinate system

The centre of the ATLAS coordinate system is the centre of the detector, which is also the nominal interaction point, i.e. the point which is designed to be the centre of the BS. The Cartesian coordinate system (x, y, z) has its x-axis pointing towards the centre of the LHC ring, the y-axis pointing upwards and the z-axis parallel to the beam axis such that its unit vector $\vec{e_z} = \vec{e_x} \times \vec{e_y}$. The rapidity y, defined as

$$\mathrm{y} = \frac{1}{2} \ln \left(\frac{E + p_z}{E - p_z} \right), \tag{2.2}$$

where E is a particle's energy and p_z its momentum along the z-direction, is a measure of the polar angle θ. Differences in y are invariant under Lorentz transformations. This property of y is particularly important in hadron–hadron collisions, in which the reference frame of the colliding partons is unknown and is different from the reference frame of the colliding protons and the detector. Using y to measure angles between objects stemming from the collision removes the dependence on the boost of the reference frame of the collision. For the relativistic collisions at the LHC, in which the contribution from the mass to a particle's energy can in general be neglected, $p_z \simeq E \cos\theta$ and the pseudorapidity, defined as

$$\eta = -\ln \tan \theta/2 \simeq \mathrm{y} \tag{2.3}$$

can be used instead of y. The origin of the azimutal angle ϕ is along the positive x-direction. The angular distance between objects is usually measured with

$$\Delta R = \sqrt{(\Delta\eta)^2 + (\Delta\phi)^2}, \tag{2.4}$$

which is invariant under boosts in the z-direction as well.

2.2.2 Inner detector

The ID, shown in Figure 2.7, is a tracking detector covering the region $|\eta| < 2.5$. It is composed of three subsystems that use different tracking technologies. It is immersed in a magnetic field of 2 T generated by the solenoid magnet. The innermost part is a semiconductor pixel detector which is required to withstand a high amount of radiation and process a high rate of hits. The pixel layer closest to the interaction point is the Insertable B-Layer (IBL), which was installed during the long shutdown prior to Run 2, together with a new, smaller beam pipe. The IBL has a pixel size of $(\phi, z) = (50, 250)$ µm, which is significantly smaller than the $(50, 400)$ µm of the three other pixel layers and improves the performance of vertex resolution. The approximately six million pixels of the IBL are placed on 14 staves. Each stave consists of 20 longitudinally assembled modules which host either 336×160 or 336×80 pixels (in ϕ-direction $\times$ η-direction), depending on the module type. The staves are slightly tilted and overlap with each other. As such, the radial distance of the pixels to the interaction point ranges from approximately 32 to 33 mm. The IBL only has a barrel component, but still covers $|\eta| < 2.5$ with its length of 332 mm and proximity to the beam pipe, while the three additional pixel layers are placed both in the barrel and end-cap regions. The pixel detector is surrounded by four Silicon Microstip Tracker (SCT) layers in the barrel and eight SCT layers in the end-cap regions, which provide further precision measurements. The gaseous Transition Radiation Tracker (TRT) surrounding the SCT contributes to momentum measurements, pattern recognition and helps with electron identification. The large amount of hits from the straw tubes of the TRT allow the tracks to be followed at large distances.

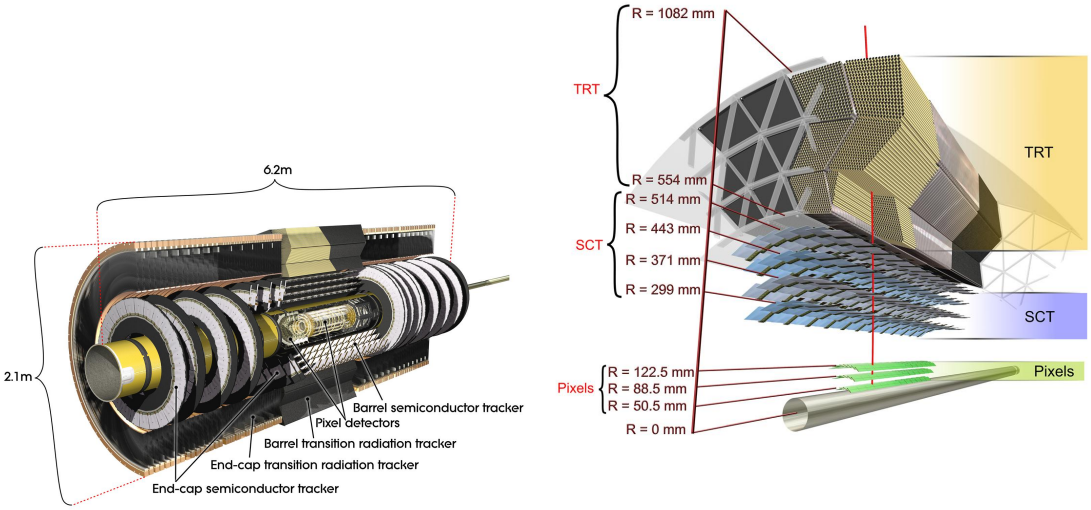

Figure 2.7: Computer generated image of the ID of ATLAS [94].

2.2.3 Calorimeters

The calorimeter system is illustrated in Figure 2.8. A Lead/Liquid Argon (LAr) electromagnetic sampling calorimeter of high granularity provides energy measurement for $|\eta| < 3.2$. It uses liquid argon as active material with accordion-shaped kapton electrodes and lead as absorber. On each side of the detector, it is divided into a barrel ($|\eta| < 1.475$) and two end-cap ($1.375 < |\eta| < 3.2$) parts. It is surrounded by hadronic sampling calorimetry. A scintillator-tile calorimeter that uses steel as absorber and scintillating tiles as active material is used for $|\eta| < 1.7$. LAr is also used for the two end-cap wheels covering $1.5 < |\eta| < 3.2$ on each side. The Forward Calorimeter (FCal) extends both electromagnetic and hadronic energy measurement up to $|\eta| = 4.9$, a region which is affected by high radiation due to the forward nature of hadron collisions. It is made of one module of copper, optimised for electromagnetic measurements and two modules of tungsten, optimised for hadronic measurements. The hadronic calorimeters are designed to limit punch-through to the MS, in which muons are to be identified reliably.

2.2.4 Muon spectrometer

The MS, which surrounds the calorimeters, is illustrated in Figure 2.9. It tracks muons in a magnetic field provided by the barrel and end-cap toroid magnets. The strong bending power, the large spacial extension of the MS and its high spacial resolution allow to greatly improve the momentum measurement of muons compared to a measurement using only the ID.

Four different detector technologies are used in the MS. The Monitored Drift Tubes (MDTs) and Cathode Strip Chambers (CSCs) provide high spacial resolution, while the Resistive Plate Chambers (RPCs) and the Thin Gap Chambers (TGCs) provide very good timing resolutions (< 4.5 ns), which are necessary for triggering purposes and to unambiguously assign a bunch-crossing to muon tracks. Since drift tubes only have a high spacial resolution perpendicular to the direction of the tubes, the RPCs and TGCs are also used to complement the spatial measurement in the

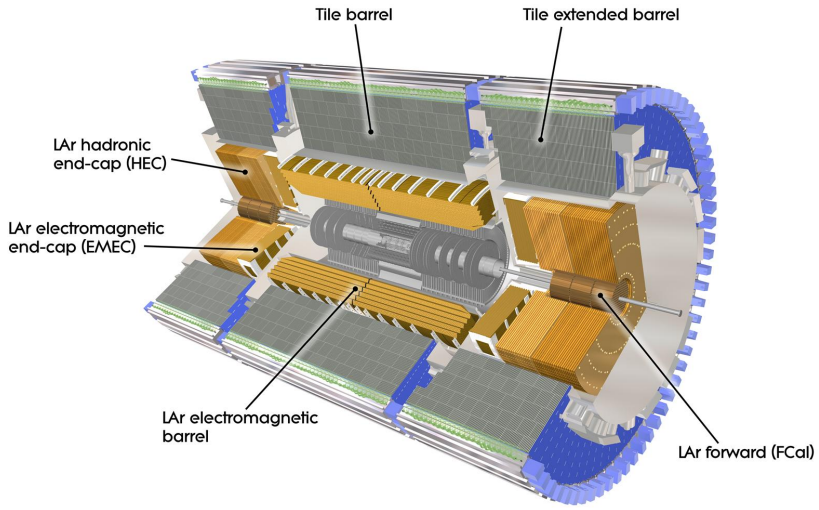

Figure 2.8: Computer generated image of ATLAS calorimeters. [95]

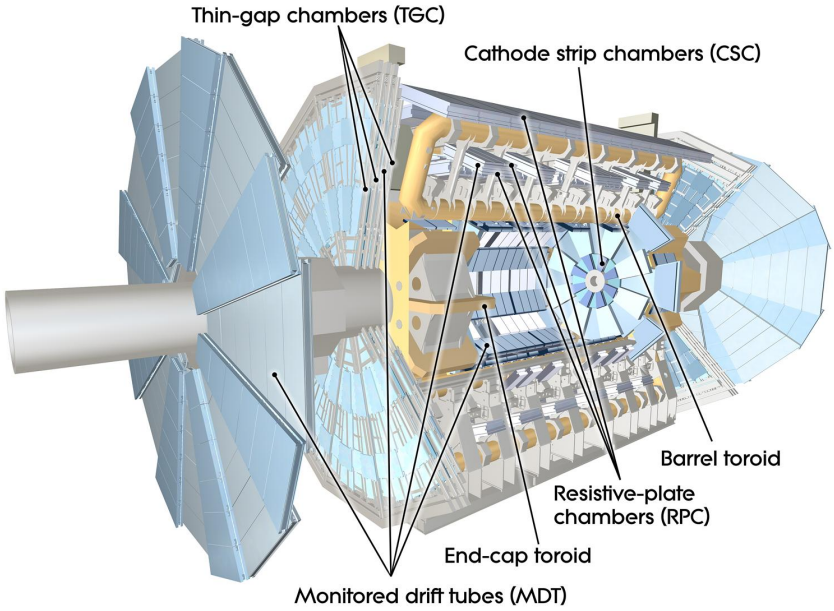

Figure 2.9: Computer generated image of the ATLAS muon spectrometer. [96]

other direction. Four layers of MDTs provide the precise measurements in the η-direction for $|\eta| < 2.7$. For $2.0 < |\eta| < 2.7$, the innermost layer of MDTs is replaced with CSCs, which are better suited to withstand the high radiation in that region. Three cylindrical layers of RPCs cover the region $|\eta| < 1.05$ and two discs of TGCs cover $1.05 < |\eta| < 2.4$ on each side. Additional layers of TGCs, the TGC Forward Inner (TGC-FI) and TGC End-cap Inner (TGC-EI), are situated in the end-cap region between the tile-calorimeter and the end-cap toroid magnet. This improves the rejection of the trigger background stemming from secondary radiation originating from the end-cap toroid magnet and beam shielding. Around $\eta = 0$ the muon system has a gap which is used to provide space for servicing the ID and calorimeters.

2.2.5 Trigger and data acquisition

Although every collision can potentially contain interesting physics, the rate of 40 MHz at which they occur is too high for the available computing resources to process and store them fully. The ATLAS trigger system overcomes this challenge by filtering events in two stages and storing most events only temporarily, except if one of a set of pre-defined requirements is met. The first stage is the Level 1 (L1) trigger system [97]. It is hardware based and has a latency of 2.5 µs. Online reconstruction is triggered with the detector response from energy deposits in the calorimeters and ionisation patterns in the muon system. In order to keep the latency low, only a coarse reconstruction is performed. If the event passes at least one requirement after the fast reconstruction at L1, it is passed to the second trigger system, the High-Level Trigger (HLT) [98], at a rate of approximately 100 kHz. The HLT uses similar reconstruction software as is used in offline reconstruction, but the reconstruction is mostly done only in small portions of the detector, called regions of interest (ROIs), which are determined by the objects reconstructed by the L1 trigger. If the event passes any of the HLT requirements, it is stored permanently. This occurs at a rate of about 1 kHz.

The data is stored long-term in a format containing all details about the events, including for example individual clusters of the pixel detector. The *express stream* processes a small fraction of the data in order to assess the quality and to derive calibration parameters that are required for more accurate reconstruction later-on. Once the calibration is updated, all triggered events are reconstructed again. These events are saved in a data format that can in principle be used by the majority of physics analyses. This central data is reprocessed approximately every year with improved algorithms. However, in Run 2, this is not yet the data-format that physics analysis are performed on. The number of events that would be processed regularly by all physicists would exceed the available computing resources of the experiment. Instead, the data is filtered into roughly 90 much smaller formats that are each specialised for specific purposes.

2.2.6 Monte Carlo simulation

Data is compared to theoretical predictions by modelling the event using Monte Carlo (MC) simulations. MC methods are used throughout the different stages of the event modelling, from the hard scattering process to hadronisation, particle decays and simulation of interactions of the particles with the detector.

The hard scattering process can usually be generated from the matrix element predicted by a limited order of perturbation theory. In hadron collisions, the parton distribution functions

(PDFs) have to be known. These are distributions that describe the probability for the proton's constituent to carry a certain fraction of momentum into the collision. The energy scale of the physics within hadrons is below the perturbative regime. The PDFs are therefore determined experimentally using measurements in deep inelastic scattering [99].

As discussed in Section 1.1.3, parton showers and subsequent hadronisation need to be simulated for all hard partons produced in the event, which includes initial- and final-state radiation and hard pile-up scattering events. The parton shower can be treated perturbatively at the scales close to the hard scattering process, but phenomenological models tuned to observations are needed when approaching the scale of hadronisation. Examples include string models [100] used in the Pythia software [101], cluster models used in the HERWIG software [102] or independent hadronisation models [103]. Subsequently, the decay of non-stable particles and additional radiation from electrically charged particles is simulated. The interaction between the final state particles and the detector is simulated using the Geant4 software [104]. Finally, digitisation transforms the simulated hits into signals that are similar to that of recorded data. The simulated events are then reconstructed in the same way as real data.

Chapter 3

Methodology

The goal of the search is to test the hypothesis of new physics in signatures of SUEPs. In order to achieve this, a counting experiment is performed, that evaluates how well the hypothesis of new physics, the *signal-plus-background* hypothesis (H_{s+b}), fits the observed data, compared to how well the hypothesis of the lack of new physics, the *background-only* hypothesis (H_b), fits the observed data. Statistically significant results are obtained by defining an event-selection for which the expectation on the number of events differs significantly between both hypotheses. The regions designed to have a high ratio of expected signal over background events are called signal regions (SRs). In order to estimate how many background events there are in the SRs, control regions (CRs) are used, in which the number of background events should be high and the expected number of signal events should be low. By knowing the shape of the background distribution, i.e., the relative number of background events between regions, the number of background events in the SRs can be inferred from the number of events in the CRs. The shape can either be taken from the background MC simulation or be based on other assumptions, in which case the background estimate is said to be done in a fully data-driven way. In the case where two observables can be found for which the distributions are uncorrelated, the ABCD-method [22] can be used. A data-driven approach is especially useful to estimate backgrounds that are not well modelled in simulations. This is generally the case for the multijet background, which is the dominant background of this search.

Additionally, validation regions (VRs) are defined, which are in regions of phase-space situated between the CRs and the SRs. These are used to verify that the background estimation method works as intended, by comparing the predicted background to data. In order to avoid being biased by the results, the search is blinded during its design until the method is fully validated, meaning that the number of events observed in the SRs is kept hidden until the background estimate is validated in the VRs. Once unblinded, the strategy should not be altered again.

For the ABCD-method to work, the CRs used to estimate the background should have negligible signal contributions. Otherwise, the prediction is spoiled when evaluating H_{s+b}. As shown in Chapter 4, with the design of CRs chosen in this analysis, significant contributions are expected for some of the signal models. In principle, one can account for this leakage simply by subtracting the contribution from the number of observed events before applying the ABCD-method. However, the signal strength is a free parameter in the likelihood fits performed to evaluate the test statistic. The background estimate is therefore entangled with the evaluation of hypotheses.

To overcome this, instead of applying the standard ABCD-method, the assumption made for the method to work (the low correlation between two observables), is included as constraint into the fits used to evaluate hypotheses.

In the following, the statistical framework used to evaluate the results of the search is introduced. Then, the standard ABCD-method and its likelihood-based variant are presented.

3.1 Statistical Analysis

The analysis presented in this thesis is a counting experiment in a set of bins. The expected number of events in each bin i can be expressed as

$$E[n_i] = \mu s_i(\boldsymbol{\alpha}) + b_i(\boldsymbol{\alpha}, \boldsymbol{\tau}), \tag{3.1}$$

where the model parameter μ is the *signal strength*, an overall normalisation factor of the signal and s_i and b_i are the mean values of expected events in each bin, for the signal and the background contributions, respectively. $\mu = 0$ corresponds to H_b and $\mu = 1$ to the nominal H_{s+b} hypothesis. Both s_i and b_i can depend on a set of additional parameters called nuisance parameters. These can be normalisation factors $\boldsymbol{\tau}$ or parametrisations of systematic uncertainties $\boldsymbol{\alpha}$. The parameters of the model can be estimated by fitting the model to data. This is done by maximising a likelihood function $L(n|\boldsymbol{\alpha}, \boldsymbol{\tau})$, which assigns a probability to obtain the set of observed number of events n for given values taken by the parameters. Since events are expected to occur independently at constant mean rates, data is expected to be Poisson distributed in each bin. The likelihood function therefore takes the form:

$$L(n|\boldsymbol{\alpha}, \boldsymbol{\tau}) = \prod_i \text{Pois}(n_i|\mu s_i(\boldsymbol{\alpha}) + b_i(\boldsymbol{\alpha}, \boldsymbol{\tau})) \prod_{\alpha \in \boldsymbol{\alpha}} f_\alpha(a_\alpha|\alpha), \tag{3.2}$$

where constrain terms f are added to describe the probability distributions associated to systematic uncertainties. For every systematic uncertainty, there is a global observable a, which can only take one value for the whole counting experiment. It is the estimated value which is observed when the systematic uncertainty is evaluated. For all systematic uncertainties used in this thesis, Gaussian distributions are chosen as constraint terms f. For practical purposes, the parameters $\boldsymbol{\alpha}$ are defined such that f_α are unit Gaussian distributions given by

$$G(\alpha) = \frac{1}{\sqrt{2\pi}} e^{-\frac{1}{2}\alpha^2}.$$

And therefore $a_\alpha = 0$ and $\sigma = 1$ for all α. In order to evaluate the effect of the systematic uncertainties on the event rates for all values each α can take, the effects of ± 1 variations on each bin are first evaluated and polynomial interpolations are made for $\alpha \in [-1; 1]$ while exponential extrapolations are made for $|\alpha| > 1$.

The frequentist approach presented in Ref. [105, 22] is used to evaluate the result of the counting experiment. As such, we want to assess the probabilities of observing the given result of the counting experiment under certain hypotheses. The agreement can be expressed in terms of a

p-value, which gives the probability of the outcome to be at least as extreme as the one observed. For this, a test statistic q is defined, which is a single-valued function of the observed data, such that the p-value is

$$p = \int_{q^{\text{obs}}}^{\infty} f(q|H)dq. \tag{3.3}$$

The p-value can be converted into a *significance* Z, the quantile of a unit Gaussian, which is given by

$$Z = \Phi^{-1}(1-p)\,,$$

where Φ^{-1} is the inverse of the cumulative distribution function for a unit Gaussian. By convention, a p-value of 0.05 ($Z = 1.64$), corresponding to the 95% CL, is chosen as threshold to exclude new-physics models. In order to exclude H_b and therefore claim that new physics is found, a threshold of $Z = 3$ counts as *evidence* while $Z = 5$ counts as *discovery*.

The standard test-statistic used at LHC experiments is the *negative log-likelihood ratio*

$$\lambda(\mu) = -2\ln\frac{L(\mu,\hat{\hat{\boldsymbol{\theta}}}(\mu))}{L(\hat{\mu},\hat{\boldsymbol{\theta}})}, \tag{3.4}$$

where $\hat{\hat{\boldsymbol{\theta}}}(\mu)$ denotes the maximum likelihood estimate of $\boldsymbol{\theta}$ for fixed μ while $\hat{\boldsymbol{\theta}}$ and $\hat{\mu}$ denote the *unconditional* maximum likelihood estimates of $\boldsymbol{\theta}$ and μ, respectively. Equation 3.4 is slightly modified depending on whether it is used to exclude H_b or H_{s+b}. When excluding H_b, the test-statistic used is:

$$q_0 = \begin{cases} \lambda(0) & \hat{\mu} \geq 0 \\ 0 & \hat{\mu} < 0. \end{cases} \tag{3.5}$$

Fixing $q_0 = 0$ for $\hat{\mu} < 0$ ensures that under-fluctuations w.r.t. the H_b prediction are not used to reject H_b. When excluding H_{s+b} with signal strength μ, the test-statistics used is:

$$q_\mu = \begin{cases} \lambda(\mu) & \hat{\mu} \leq \mu \\ 0 & \hat{\mu} > \mu, \end{cases} \tag{3.6}$$

which ensures that an over-fluctuation w.r.t. the H_{s+b} prediction is not used to exclude H_{s+b}.

In order to compute the p-values using Eqn. 3.3, the probability density functions (pdfs) of the test-statistic have to be known. This can be obtained by generating a set of random fake datasets. Alternatively, the asymptotic formulae shown in Ref. [106] can be used to approximate the significance of the result. These are valid for sufficiently large background contributions. When excluding H_{s+b}, instead of using the p-value p_{s+b} directly, in order to avoid excluding signals when the sensitivity of the experiment is low, the quantity

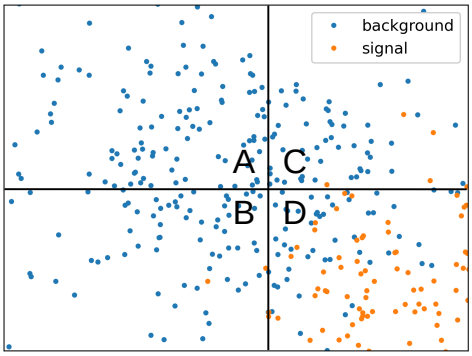

(a) Schematic description of an ABCD-plane with four regions.

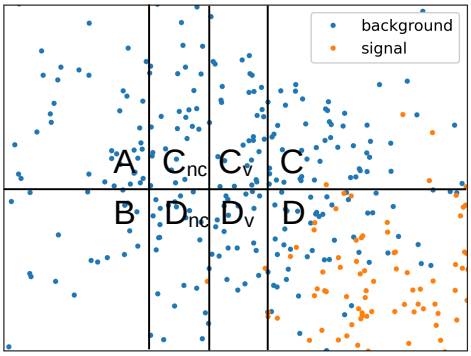

(b) Schematic description of an ABCD-plane with additional regions used to measure non-closure and to validate the method.

Figure 3.1: Schematic descriptions of ABCD-planes.

$$CL_s = \frac{p_{s+b}}{p_b} \tag{3.7}$$

is used, where the p-value p_b is computed using q_μ for $\mu = 0$.

3.2 ABCD-Method

Figure 3.1(a) shows schematically the distribution of background and signal in a plane spanned by two variables that are uncorrelated for the background. Omitting signal contamination in the control regions A, B, and C, the expected background yield in the signal region D is given by

$$N_D^{\text{exp}} = \frac{N_B N_C}{N_A}, \tag{3.8}$$

where N_i are the observed yields in the control regions. The statistical uncertainty on N_D^{exp} is given by

$$\sigma_{\text{stat}}(N_D^{\text{exp}}) = \sqrt{N_D^{\text{exp}}}.$$

Additionally, there is the uncertainty caused by the propagation of the statistical uncertainties on N_A, N_B and N_C, which are given by $\sigma(N_i)_{\text{stat}} = \sqrt{N_i}$. This uncertainty, which we will call the systematic uncertainty related to the ABCD-method, is given by:

$$\begin{aligned}\sigma_{\text{sys}}(N_D^{\text{exp}}) &= \sqrt{\left(\frac{\partial N_D^{\text{exp}}}{\partial N_A}\right)^2 \sigma(N_A)^2 + \left(\frac{\partial N_D^{\text{exp}}}{\partial N_B}\right)^2 \sigma(N_B)^2 + \left(\frac{\partial N_D^{\text{exp}}}{\partial N_C}\right)^2 \sigma(N_C)^2} \\ &= \sqrt{\frac{N_B^2 N_C^2}{N_A^3} + \frac{N_C^2 N_B}{N_A^2} + \frac{N_B^2 N_C}{N_A^2}},\end{aligned} \tag{3.9}$$

In its simplest form this is all that is required to predict the background with this method. Additionally, we can verify if the yield predicted by the ABCD-method matches the observed number of events in additional region(s) in which the signal contribution is small and add a non-closure uncertainty in case there is a statistically significant deviation observed. There are several ways in which these additional regions can be defined, but they should be inserted close to the SR in order to capture as much as possible of potential effects that play a role there. Figure 3.1(b) shows schematically a setup in which this is done. D_{nc}, is the region in which the non-closure will be measured and it has an associated control region C_{nc}. In a first step, the ABCD-method is evaluated using A, B, $C_{\text{nc}} \cup C_{\text{v}}$ and $D_{\text{nc}} \cup D_{\text{v}}$. If the expected number of events is further away from the observed number of events, i.e.

$$\left| \frac{N_B(N_{C_{\text{nc}}} + N_{C_{\text{v}}})}{N_A} - (N_{D_{\text{nc}}} + N_{D_{\text{v}}}) \right| > \sqrt{\sigma^2_{\text{stat}} + \sigma^2_{\text{sys}}},$$

then the *relative* non-closure uncertainty

$$\sigma^r_{\text{nc}} = \frac{\left| N_{D_{\text{nc}}} - N^{\text{exp}}_{D_{\text{nc}}} \right|}{N^{\text{exp}}_{D_{\text{nc}}}}, \tag{3.10}$$

where

$$N^{\text{exp}}_{D_{\text{nc}}} = \frac{N_B N_{C_{\text{nc}}}}{N_A},$$

is computed, such that the non-closure uncertainty in the SR is $\sigma_{\text{nc}}(N^{\text{exp}}_D) = \sigma^r_{\text{nc}} N^{\text{exp}}_D$.

Finally, the method is validated in D_{v} with the additional non-closure uncertainty, which ensures that the unforeseen effect caught in the non-closure regions does not grow towards the signal region.

3.2.1 Likelihood-based ABCD-method

In the likelihood-based ABCD-method, the assumption made about the background distribution in the ABCD-plane is incorporated into the background model given by Eqn. 3.1. In order to achieve this, four background processes, b_A, b_B, b_C and b_D, are defined. Each of them populates only the respective regions A, B, C or D. Furthermore, the normalisation of these processes is defined in the following way:

$$\begin{aligned} b_A &= \mu_A \\ b_B &= \mu_A \epsilon_{AB} \\ b_C &= \mu_A \epsilon_{AC} \\ b_D &= \mu_A \epsilon_{AB} \epsilon_{AC}. \end{aligned} \tag{3.11}$$

In this way, $\frac{b_A}{b_B} = \frac{b_C}{b_D}$. The expected rates in all four regions are then given by

$$\begin{aligned} E[n_A] &= \mu s_A(\boldsymbol{\theta}) + b_A \\ E[n_B] &= \mu s_B(\boldsymbol{\theta}) + b_B \\ E[n_C] &= \mu s_C(\boldsymbol{\theta}) + b_C \\ E[n_D] &= \mu s_D(\boldsymbol{\theta}) + b_D, \end{aligned} \tag{3.12}$$

A non-closure uncertainty can be added with a multiplicative factor affecting the background rate in the signal region; i.e.

$$b_D = \mu_A \epsilon_{AB} \epsilon_{AC} (1 + \alpha_{\text{nc}} \sigma^r_{\text{nc}}),$$

where σ^r_{nc} is the relative non-closure uncertainty defined by Eqn. 3.10. The likelihood function then becomes:

$$L(\boldsymbol{\theta}) = \prod_{i \in A,B,C,D} \text{Pois}(n_i | \mu s_i(\boldsymbol{\theta}) + b_i(\mu_A, \epsilon_{AB}, \epsilon_{AC}, \alpha_{\text{nc}})) \prod_{\alpha \in \boldsymbol{\alpha}} G(\alpha). \tag{3.13}$$

Multiple SR-bins

The SR can be split into several bins in order to gain additional sensitivity from the difference in shape between background and signal within the SR. For m bins in the SR, the definitions in Eqn. 3.11 are extended to:

$$\begin{aligned} b_A &= \mu_A \\ b_B &= \mu_A \epsilon_{AB} \\ b_{C_1} &= \mu_A \epsilon_1 \\ b_{D_1} &= \mu_A \epsilon_{AB} \epsilon_1 (1 + \alpha_{\text{nc},1} \sigma^r_{\text{nc}}) \\ &\vdots \\ b_{C_m} &= \mu_A \epsilon_m \\ b_{D_m} &= \mu_A \epsilon_{AB} \epsilon_m (1 + \alpha_{\text{nc},m} \sigma^r_{\text{nc}}). \end{aligned} \tag{3.14}$$

Here we allow an uncorrelated fluctuation of the non-closure uncertainty between bins. Alternatively, one could use the same parameter for all bin fluctuations. Allowing the parameters to fluctuate independently in each of the bins is the most conservative choice, since it relaxes the likelihood more than having correlated parameters.

Chapter 4

Analysis

4.1 Introduction

The general SUEP case encompasses a wide variety of signatures. The signature is always a high multiplicity of soft final state particles that are spherically distributed in the reference frame of the mediator, but depending on the particle composition of the final state and the distribution of their momenta, which dictates how efficiently they can be reconstructed, the possible analysis strategies differ. The ATLAS detector has great muon reconstruction capabilities. Prompt muons can be reconstructed within $|\eta| < 2.5$ at about 95% efficiency for transverse momenta $p_{\mathrm{T}} > 5$ GeV and at about 70% efficiency for $p_{\mathrm{T}} \simeq 3$ GeV without significant misidentification of in-flight decays of light hadrons [107]. In contrast, the reconstruction efficiency of electrons already starts to drop for transverse momenta below approximately 60 GeV and lies between 65% and 85% for $p_{\mathrm{T}} = 20$ GeV, depending on the quality working point [108]. Therefore, electron reconstruction is not helpful in the p_{T}-regime we are interested in, which is $\mathcal{O}(1\text{ GeV})$. One could, of course, also design strategies targeting SUEPs with final states of higher momenta, but then the signature would resemble that of microscopic black holes, which already have been searched for at the LHC [109, 110].[†] If the SUEP contains muons in the final state, they can be selected by a multi-muon trigger that has low per-muon p_{T} thresholds. Together with the possible reconstruction of muons down to $p_{\mathrm{T}} = 3$ GeV, it allows for a muon-based search strategy.

Other strategies, that do not involve any lepton identification, are also conceivable. These would be useful to target signal models that do not contain any muons in the final state, or signal models of lower temperatures or dark-meson masses, for which muon reconstruction is inefficient. Using tight selection criteria, ID tracks can be reconstructed with about 70% efficiency for $p_{\mathrm{T}} = 0.5$ GeV, with fake rates below approximately 1% [112]. Since the number of particles stemming from a SUEP decay is proportional to $\frac{1}{\Lambda}$ and $\Lambda \sim T \sim p_{\mathrm{T}}$, the number of tracks in the SUEP signal is high for the range of temperatures in which muon reconstruction is not available. Therefore, the SUEP signal can be separated efficiently from background using the track multiplicity as an observable. However, there are no adequate triggers available for such a signature in Run 2. One would have to restrict the search to target signal models in which the mediator is the Higgs

[†] The microscopic black holes that have been searched for in References [109, 110] emit all kinds of SM particles isotropically through Hawking radiation [111]. The final state objects have transverse momenta $\mathcal{O}(10\text{ GeV})$.

boson, which can be produced in association with a vector boson. The decay products of vector bosons can be triggered on efficiently with the use of single or di-lepton triggers. The advantage of this approach is that the dominant background (V+jets) is well known.

For signal models of even lower temperatures, for which the majority of particles have $p_{\mathrm{T}} < 0.5$ GeV, track reconstruction is inefficient as well. However, a charged particle in a magnetic field of 2 T can still reach the IBL if its p_{T} is above approximately 10 MeV.[†] Since at these low temperatures, the particle multiplicity is extremely high, the number of pixel clusters in the IBL can be used as a discriminating variable. At very low temperatures, another characteristic feature of the signature is the possible presence of an imbalance of energy deposits in the calorimeters, i.e. missing transverse energy ($E_{\mathrm{T}}^{\mathrm{miss}}$), which might be used for triggering purposes.

Preliminary studies on elements of a pixel-cluster based strategy are given in Chapter 6. In the next section, an overview of the muon-based search strategy is given, after which the analysis is presented in detail.

4.1.1 Muon-based strategy

The premise of the muon-based search strategy is that the signal model contains a sufficient amount of muons in the final state in order for events to pass a multi-muon trigger. After the online event selection, a preselection is applied: A requirement on muon multiplicity is used to increase the overall signal-to-background ratio. Additionally, the average p_{T} of all muons in the event is required to be low. Besides increasing the overall signal-to-background ratio, this removes contributions containing prompt, high-p_{T} muons, like the pair production of top quarks ($t\bar{t}$), where subsequently $t \to b\mu\nu_{\mu}$. After this preselection, the dominant background is expected to be heavy-flavour multijet events. Since heavy-flavour mesons have detector scale lifetimes, the heavy-flavour multijet background is distinguishable from the prompt SUEP signal by the presence of displaced muons. Moreover, the SUEP signal is expected to contain a higher number of ID tracks. For the heavy-flavour multijet background, the total track multiplicity in the event is expected to be largely uncorrelated to the displacement of muons. Therefore, the ABCD-method can be used to estimate the background in a region of high track multiplicity and low muon displacement, which forms the SR of the search.

The object selection is tailored to the needs of the analysis. Tight requirements are made on the impact parameters of tracks, in order to reject the contribution from pile-up as much as possible, and a recently-developed muon selection prescription [113], which is well suited for low-p_{T} muons, is used for muon identification.

Since the simulation of MC samples in ATLAS starts before data is taken, some features of real data are not reflected correctly in the simulations. The operational status of detector components, for example, changes over time, which means that object reconstruction and trigger selection efficiencies vary as a function of η and ϕ and over the periods of data-taking. This is accounted for by measuring the efficiencies separately in data and MC and applying scale factors as event weights to MC. For muon reconstruction, the required studies on reconstruction efficiencies have been performed by the ATLAS Muon Performance Group. The corrections and associated systematic uncertainties are provided automatically using software tools. Although similar

[†] Obtained using $p = rqB$, with B the magnetic field, q the electron charge, and $r = \frac{32}{2}$ mm, the required radius to reach the IBL.

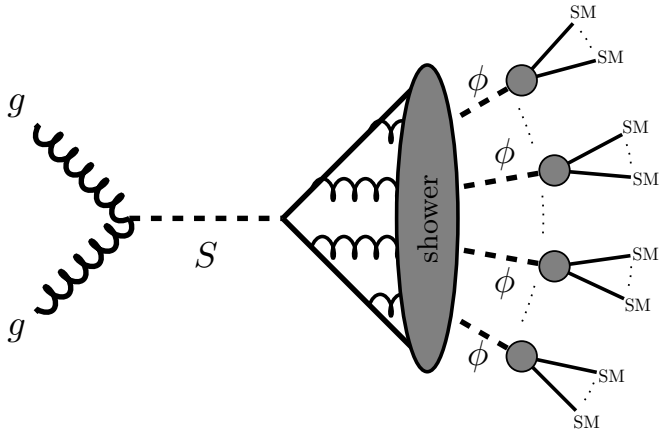

Figure 4.1: Schematic description of the SUEP process with the production of the mediator S through gluon–gluon fusion, a shower and hadronisation in the HV and subsequent decay of dark mesons ϕ into SM particles. [18]

measurements and tools are in general provided for the muon trigger performance, they were not available for the multi-muon trigger used in this analysis. Moreover, since the trigger is used at the lower end of its p_{T} acceptance, an additional dependence on the p_{T} of muons has to be taken into account when measuring the trigger efficiency. Therefore, a dedicated measurement of the trigger efficiency is performed. Another aspect that is mismodelled in MC is the pile-up density within the BS, which varies over time with the shape of the BS and with the number of simultaneous interactions per bunch-crossing. A measurement is performed to estimate the contribution from pile-up to the track multiplicity.

The design of SRs, CRs and VRs needs to account for the wide variety of targeted signal models, which greatly differ in the distribution of track multiplicity. It is not possible to create a setup that is ideal for all possible signal models. For the choice of the setup made here, some of the signal models significantly contribute to the CRs. The likelihood-based ABCD-method presented in Section 3.2.1 is used to account for this.

Ideally, a SR is designed such that the background estimate can be validated in a region close to it. At the same time, the SR should have a high ratio of expected signal over background events. Due to the diversity of signal models targeted here, both requirements cannot be fulfilled simultaneously with a static definition of the regions. Therefore, an incremental unblinding strategy, in which portions of data are unblinded step-by-step, is presented. With this unblinding strategy, different signal models can be probed at different stages of the unblinding procedure and the region definitions can be adapted to be better suited for the remaining signal models.

4.2 Signal model

The signal model used in this work is based on the assumptions and approximations made in Ref. [18]. In particular, it is assumed that the bottom of the HV consists of only one dark-meson species ϕ of mass m and that the momenta of the dark mesons follow a Boltzmann distribution. The process is described schematically in Figure 4.1. The mediator S is a scalar particle of mass M that is produced via gluon–gluon fusion. The mediator masses considered are $M = 125$ GeV,

Table 4.1: Benchmarks used for dark-meson masses m and temperatures T.

m (GeV)	T (GeV)		
1.5	1.0	1.5	2.25
3.0	2.0	3.0	4.5
5.0	3.33	5.0	7.5

in which case it is assumed to be the Higgs boson, and $M = 400, 750$ GeV. As discussed in Section 1.3.1, simulations based on perturbative QCD calculations can only be used for the production of the heavy mediator and for the decay of the dark mesons to the SM. For the shower and hadronisation in the HV, a dedicated Pythia plugin [114] is used. From a mediator S, it generates a set of dark mesons such that they are spherically distributed in the centre-of-mass frame of S, that their momenta follow a Boltzmann distribution of temperature T and the total energy M is conserved. The dark-meson masses considered are $m = 1.5$ GeV, $m = 3$ GeV and $m = 5$ GeV. Since it is expected that $T \simeq \Lambda \simeq m$, values of $T = 0.5\ m$, $1.0\ m$ and $1.5\ m$ are considered. The set of parameters m and T used are summarised in Table 4.1.

A decay back to the SM is required in order to get a detectable signal. Kinematic mixing between a dark photon and the SM photon [115] is one option, which is chosen for a practical reason: it allows for various realistic final-state particle compositions. Figure 4.2 shows the branching ratio of dark photons as a function of the dark photon mass. For a big portion of possible dark photon masses, the existing experimental constrains still allow cross-sections to be sufficiently large for the decays to be prompt [116]. Even though the goal of this search is not to probe for dark photons, it should be noted that dark photons are well motivated themselves. They can explain a possible enhanced production of $\mathcal{O}(10\ \text{GeV})$ positrons observed in the galactic vicinity of the solar system [117] as well as the discrepancy measured in the anomalous magnetic moment of the muon [118]. Three benchmarks were used for the branching ratios of dark photon decays and are summarised in Table 4.2. The leptonic–hadronic benchmark (*lep-had*) is used as the baseline benchmark. All variations of m and T have been simulated for this benchmark. The leptonic benchmark (*lep*) is only used for $M = 125$ GeV, which is more challenging to probe than signal models with higher mediator masses due to the reduced total energy available in the SUEP decay. The hadronic benchmark (*had*) has only been simulated for $M = 400$ GeV and $M = 750$ GeV and can be used to see how the sensitivity of the search changes with a reduced number of muons in the final state.

The signal samples are named with the following convention:

$$\text{SUEP(production mechanism, branching ratio benchmark, } M, m, T).$$

In the sample names, *lep-had*, *lep* and *had* are abbreviated to LH, L and H, respectively.

In this search, only gluon–gluon fusion (ggH) is considered as production mechanism.[†]

Figure 4.3 illustrates how variations in the model parameters affect the final-state muon multiplicity and p_{T} spectrum using *lep-had* benchmark signal models. As expected, muon multiplicity

[†] Even though ggH is the only production mechanism considered in this analysis, the reference is kept in the name in order for comparisons with future publications, which might consider other production mechanisms, to be more clear.

Table 4.2: Benchmarks used for branching ratios of the dark photon.

	e	μ	pions
lep-had (LH)	0.4	0.4	0.2
had (H)	0.15	0.15	0.7
lep (L)	0.5	0.5	0.0

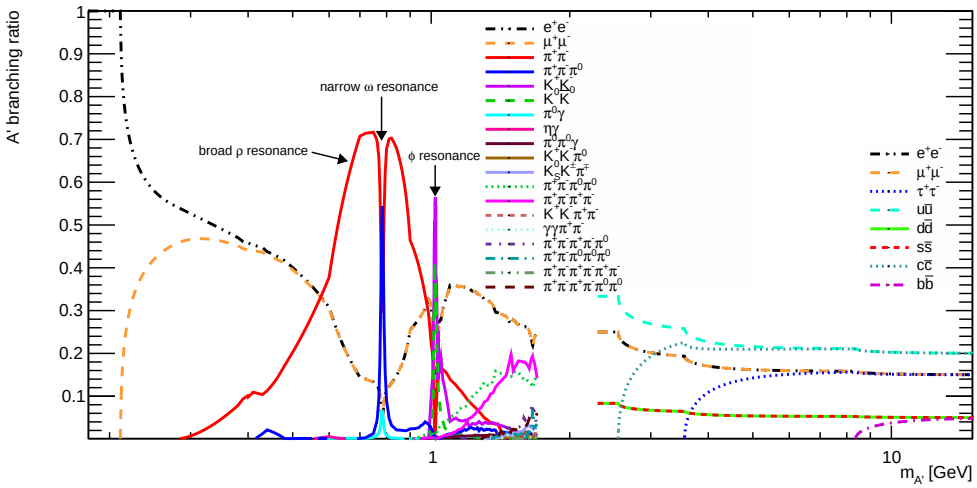

Figure 4.2: Branching ratios for 19 dark photon decay channels. [10]

scales with M. Increasing m or T skews the momentum distribution to higher values and decreases muon multiplicity.

4.3 Monte Carlo samples

The production of the mediator for the signal samples is done with Pythia8 [119] (version 8.244), using the NNPDF 2.3 LO PDF set. As mentioned in the previous section, the shower and hadronisation in the HV is done with a dedicated Pythia plugin [114]. Once dark mesons have decayed to SM particles, Pythia8 with the tune ATLAS A14 is used again, in order to simulate further showering and hadronisation within the SM. Atlfast-II [120] is used to simulate interactions with the detector. It uses Geant4 [104] for most detector components, but a parameterised simulation of the interactions in the calorimeters, which significantly reduces CPU-consumption. The production cross-section of SUEP events is unknown. As benchmarks, the cross-sections of the production of beyond the Standard Model (BSM) Higgs bosons through gluon–gluon fusion are taken for $M = 400$ GeV and $M = 750$ GeV. For $M = 125$ GeV, the mediator is assumed to be the SM Higgs boson. In that case, the production cross-section of the SM Higgs boson is used, but an additional branching ratio of 10% is applied, which is of the order of the current upper limit on the branch ratio of the decay of the Higgs boson into so far undetected final states [121]. The values $\sigma_{125} = 4.2$ pb, $\sigma_{400} = 9.5$ pb, and $\sigma_{750} = 0.64$ pb, used for $M = 125$ GeV, $M = 400$ GeV, and $M = 750$ GeV, respectively, are based calculations provided by the LHC Higgs Cross Section Working Group [122].

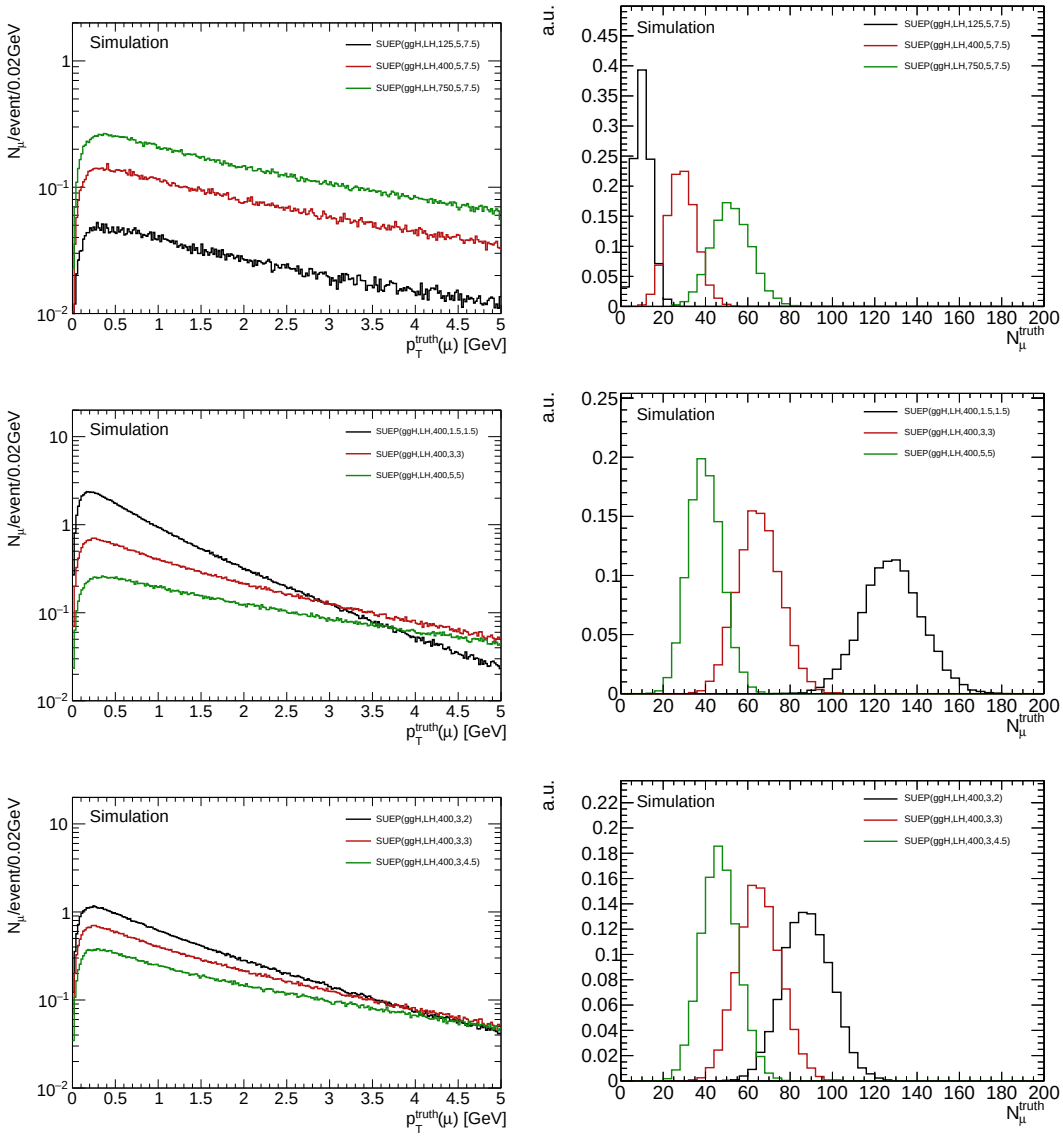

Figure 4.3: True muon multiplicity (left) and p_{T} (right) distributions for varying mediator mass M (top), varying dark pion mass m and temperature $T = m$ (middle), and independent variations of the temperature T (bottom).

Table 4.3: Event generators, tunes and PDF sets used for background MC samples.

Process	Generator(s)	PDF set
multijet	EvtGen 1.2.0 + Pythia 8.186 (tune A14)	NNPDF 2.3 (LO)
$t\bar{t}$	Powheg + EvtGen 1.6.0 + Pythia 8.230 (tune A14)	NNPDF 2.3 (LO)
$t\bar{t} + Z$	MadGraph5_aMC@NLO 2.3.3 + EvtGen 1.2.0 + Pythia 8.210 (tune A14)	NNPDF 2.3 (LO)
$Z \to \mu\mu$	Powheg + EvtGen 1.2.0 + Pythia 8.186 (tune AZNLO) + Photospp	CTEQ6L1 (LO)
$ZZ \to \mu\mu\mu\mu$	aMcAtNlo + EvtGen 1.7.0 + Pythia 8.244 (tune A14)	NNPDF 2.3 (LO)
WWZ	Sherpa 2.22 (Sherpa default tune)	NNPDF 3.0 (NNLO)

No background MC samples are used for the background estimate, which is done in a fully data-driven way. Simulated background samples are only used to confirm that the dominant background after the preselection is multijet events. Furthermore, a $Z \to \mu\mu$ sample is used to estimate the parameters needed to correct the track multiplicity in signal MC samples and to measure the trigger efficiency for MC. These background samples that are used are centrally produced samples that are used in many analyses in ATLAS. Table 4.3 summarises the generators and PDF sets used for each sample. The list of dataset identifiers and sample names are given in Appendix B. Detailed descriptions of the simulations can be found in Refs. [123–126]. All simulated events are overlaid with a Pythia8 pile-up simulations, generated following the prescription described in Ref. [127]. In order to increase the statistics for the multijet background, a sample which is filtered to contain at least one muon is used.

4.4 Online event selection

The trigger strategy for this search is based on the high multiplicity of muons contained in the SUEP events. The multi-muon trigger with the lowest per-muon p_{T}-threshold that was active during the whole period of data-taking is HLT_3mu6, which requires three muons with $p_{\mathrm{T}} > 6$ GeV both at L1 and for the HLT. A more detailed description of the trigger chain can be found in Ref. [128] and a summary is given below.

At L1, the coincidence between hits in different detector layers is required for each muon candidate. In the barrel region, a coincidence of only two of the three RPC layers is required, since for this low p_{T}, muons are less likely to reach the third layer in the barrel region. Hits in all four of the TGC layers are required in the end-cap region, including either the TGC-FI or the TGC-EI, which suppresses the background from secondary radiation stemming from the endcap toroid magnets. Additionally, a coincidence is required in the tile hadronic calorimeter for the region $1.05 < \eta < 1.3$, which mitigates the low MS coverage in that region. The p_{T} estimate at L1 is based on the deviation of the hit pattern from that of muon with infinite momentum. The global L1 decision requires three muons with $p_{\mathrm{T}} > 6$ GeV. After a positive decision at L1, ROIs of dimensions of 0.1×0.1 or 0.3×0.3 in $\Delta\eta \times \Delta\phi$ are saved for patterns stemming from the RPCs or TGCs, respectively.

The HLT first selects events with a fast track-reconstruction algorithm followed by a selection by a precision stage. The fast reconstruction starts with a simple track reconstruction based on MDT hits within the ROIs selected at L1. In order to obtain improved track-parameter resolutions, this MS track is then combined with an ID track by extrapolating the trajectory to the interaction

Table 4.4: Trigger efficiencies [%] for HLT_3mu6 and other trigger chains for a selection of signal benchmark models. Values are rounded to the first decimal. Statistical uncertainties are $\mathcal{O}(10^{-4}\%)$.

	HLT_3mu6	HLT_4mu4	HLT_2e17_lhvloose_nod0_L12EM15VHI	HLT_2e12_lhloose_nod0_mu10	HLT_e12_lhloose_nod0_2mu10
SUEP(ggH,LH,125,1.5,1.5)	3.1	5.3	0.0	0.0	0.1
SUEP(ggH,LH,125,3,2)	6.3	10.9	0.0	0.1	0.5
SUEP(ggH,LH,125,3,3)	12.1	18.7	0.0	0.3	1.1
SUEP(ggH,LH,125,3,4.5)	19.2	23.5	0.1	0.8	2.5
SUEP(ggH,LH,125,5,5)	21.9	26.0	0.3	1.5	4.0
SUEP(ggH,LH,400,1.5,1.5)	5.9	19.9	0.0	0.0	0.0
SUEP(ggH,LH,400,3,2)	25.2	62.8	0.0	0.1	0.8
SUEP(ggH,LH,400,3,4.5)	82.3	93.7	0.4	9.7	20.8
SUEP(ggH,LH,750,1.5,1.5)	10.8	49.3	0.0	0.0	0.1
SUEP(ggH,LH,750,3,2)	54.1	94.6	0.0	0.2	1.2
SUEP(ggH,LH,750,3,3)	90.7	99.5	0.1	4.6	12.1
SUEP(ggH,LH,750,3,4.5)	98.7	99.9	0.7	25.6	48.3
SUEP(ggH,LH,750,5,5)	99.2	99.9	2.6	38.0	63.2
SUEP(ggH,H,750,3,2)	13.4	38.1	0.0	0.0	0.1
SUEP(ggH,H,750,3,3)	38.8	65.7	0.0	0.3	1.5
SUEP(ggH,H,750,3,4.5)	60.8	77.1	0.1	3.0	8.2
SUEP(ggH,L,125,1.5,1)	2.0	3.9	0.0	0.0	0.0
SUEP(ggH,L,125,1.5,1.5)	3.8	7.2	0.0	0.0	0.2
SUEP(ggH,L,125,1.5,2.25)	7.1	13.5	0.0	0.1	0.7

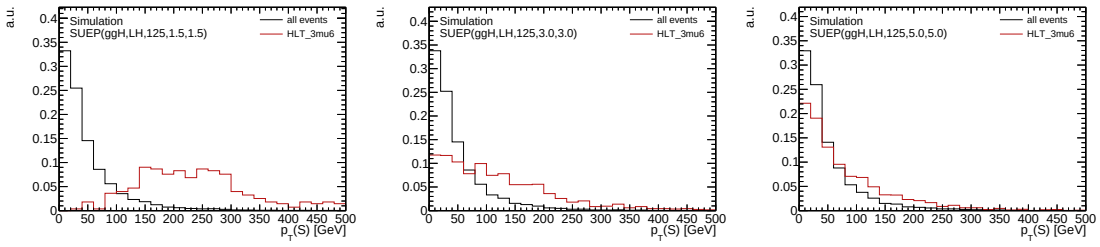

Figure 4.4: Transverse momentum of the mediator S before and after passing the HLT_3mu6 trigger for lep-had SUEP signals with $M = 125$ GeV and $m = T = 1.5$ GeV (left), 3 GeV (middle) and 5 GeV (right).

point. For the HLT_3mu6 chain, the precision stage only uses the fast reconstruction variant called the ROI-based mode, which uses the ROIs defined at L1 and performs less CPU-intensive reconstruction compared to the full-scan mode used for other multi-muon trigger chains. In the ROI-based mode, muon candidates are first reconstructed in the MS and back-extrapolated to the ID, after which a combined fit with hits from both detector systems is performed. If no combined muon is formed in this way for the given ROI, ID tracks are extrapolated and combined with segments in the MS. An isolation criterion is applied, which is based on the ratio of the sum of the transverse momenta of all ID tracks that originate from within a longitudinal distance of 2 or 6 mm, depending on the period of data-taking, over the transverse momentum of the muon. Fortunately, this isolation requirement does not seem to affect the event selection efficiency greatly for the highly populated SUEP events. For example, the signal SUEP(ggH, LH, 750, 5, 7.5) passes HLT_3mu6 with 99% efficiency, according to simulation. The final HLT selection requires three combined muons with $p_{\mathrm{T}} > 6$ GeV.

Table 4.4 shows the efficiency of passing HLT_3mu6 for various signal models together with the efficiencies for other trigger chains that were investigated. HLT_4mu4, which is similar to HLT_3mu6, but requires four muons of $p_{\mathrm{T}} > 4$ GeV, performs better than HLT_3mu6 for all signal models. Unfortunately, this trigger chain is not available during the whole period of data-taking in Run 2. It could be used in conjunction with HLT_3mu6 in order to increase the efficiency when it is available, but for simplicity, only HLT_3mu6 is used in the first iteration of the analysis. The di-electron trigger HLT_2e17_lhvloose_nod0_L12EM15VHI, which will not be described in detail here, is one of the di-electron trigger chains with the lowest threshold that was online during Run 2. It requires two electrons of $p_{\mathrm{T}} > 17$ GeV. The efficiency for SUEP events passing this trigger is very small. The same can be said for HLT_2e12_lhloose_nod0_mu10, which requires two electrons with $p_{\mathrm{T}} > 12$ GeV and a muon with $p_{\mathrm{T}} > 10$ GeV and for HLT_e12_lhloose_nod0_2mu10, which requires one electron with $p_{\mathrm{T}} > 12$ GeV and two muons with $p_{\mathrm{T}} > 10$ GeV. The latter performing best amongst the multi-lepton triggers, due to the lower required p_{T} threshold.

It should be noted that for low dark-meson masses and temperatures, the trigger selection using HLT_3mu6 relies on ISR against which the mediator recoils, giving the muons sufficient momentum to be selected by the trigger. This can be seen in Figure 4.4, which shows the transverse momentum of the mediator before and after the trigger selection for signal models with increasing dark-meson mass and temperature. This greatly affects the event shape of the final state.

4.5 Track reconstruction and selection

Track reconstruction in the ID starts with the construction of segments called *track seeds* from clusters formed by hits in the pixel and SCT detectors [112]. Pixels or strips are grouped in clusters if the energy deposited in them exceeds a threshold and if their edges or corners touch. The intersection point between the particle and the sensor is determined by considering how much charge was deposited for each hit in the cluster, which depends on the path length of the particle in the sensor. The track seeds are built from at least three clusters, which is the minimum number required to estimate the momentum of the particle. The Kalman filtering presented in Ref. [129] is used to extend the track seeds with additional clusters into *track candidates*. A score is then assigned to all track candidates. It is based on the residual of the track fit, the

number of clusters assigned to the track and the number of holes in the track, which are hits that are expected, given the trajectory and operational status of the component, but are missing. Tracks of lower momentum are also penalised since they are more likely to be formed from wrongly assigned clusters. An ambiguity solver then filters tracks based on the score and the number of shared hits. Finally, a complete track fit is performed, including TRT measurements. A requirement of $p_{\mathrm{T}} > 500$ MeV is applied as part of ATLAS' standard track reconstruction. Particles of lower momenta are expected to be trapped within the ID and their tracks are difficult to reconstruct. All tracks within the acceptance of the ID ($|\eta| < 2.5$) are accepted.

A series of requirements on the number of hits within the tracking detectors are used to increase the rejection of combinatorial background (fake tracks). For $|\eta| < 1.65$, at least a total of nine hits are required in the silicon detectors (pixel and SCT). For $1.65 < |\eta| < 2.5$, corresponding to the region covered by the end-cap components of the silicon detectors that have a higher total number of layers, the required minimal number of silicon hits is increased to 11. The required number of silicon hits is reduced by one for every time the track trajectory crosses a non-operational sensor. Tracks with holes in the pixel detector are always rejected and a maximum of two holes are allowed in the SCT in total. A maximum of one cluster is allowed to be shared with another track in the pixel detector. If no cluster is shared in the pixel detector, two clusters are allowed to be shared in the SCT.

Since the search targets SUEP signal models with prompt decays, a tight selection on the impact parameters of the track can be made in order to reduce the contributions from pile-up collisions and further reject combinatorial background. The impact parameters d_0 and Δz_0 are the radial and longitudinal distance between the point of closest approach of the track to the primary vertex, whose reconstruction is described in the next section. The requirement $d_0 < 0.5$ mm and $\Delta z_0 \sin\theta < 0.5$ mm, corresponding to the *tight* working point studied by the ATLAS ID Performance Working Group, is applied. The impact-parameter resolution of track reconstruction for tracks with $p_{\mathrm{T}} < 1$ GeV is $(\sigma(d_0), \sigma(z_0)) \simeq (0.08, 0.14)$ [130]. The selection therefore guarantees that the majority of the prompt tracks are selected. With this selection, approximately five tracks from pile-up vertices are expected to contribute to the track multiplicity for a primary collision in the centre of the BS and $\mu = 25$, as shown in Section 4.9.

4.6 Vertex reconstruction and selection

Vertices are reconstructed using a selection of ID tracks [131]. The selection is based on track quality parameters like the number of hits and holes in detector components and its impact parameter w.r.t. the centre of the BS. First, a seed position is determined from the position of the BS and the impact parameters of all tracks in the selection. Starting from the seed position, an iterative fitting procedure estimates the best vertex position and assigns weights to each track based on the compatibility of the impact parameters with the fitted vertex. Once a vertex is fitted, incompatible tracks are used to repeat the procedure and find additional vertices. The Primary Vertex (PV) is the vertex for which the scalar sum of the square of the transverse momenta of all tracks that are associated to it is maximal.

4.7 Muon reconstruction and selection

Muon reconstruction mainly uses information from the ID and the MS, but information from the calorimeters is also used, mainly to help determine track parameters. Tracking in the MS is described in more detail in Ref. [107]. It starts with the identification of local track segments in individual MS stations by using a Hough transform [132]. Track segments are then combined into track candidates, on which a global χ^2 fit is performed. From the trajectory obtained by the fit, outlier hits are removed and the fit is repeated. Ambiguous tracks that share a large amount of hits with tracks of better quality are removed. A final fit is performed, which includes a constrain on the impact parameter and takes into account energy loss in the calorimeters.

Several types of muon reconstructions can be performed with the ATLAS detector, as described in more detail in Ref. [107]. In this work, only Combined (CB), Inside-Out combined (IO) and Segment-Tagged (ST) muon reconstructions are used. CB muons is the standard muon reconstruction in ATLAS and relies on independent track reconstruction from both the MS and the ID. IO and ST reconstruction do not rely on full track reconstruction in the MS, which is particularly useful for low-p_{T} muons, since muons lose on average 3 GeV of energy when traversing the calorimeters and might not make it through the whole MS.

CB muons are identified by requiring that an MS track matches an ID track. The track parameters are obtained by performing a fit that uses both MS and ID hits. With the new trajectory, outliers in the MS are removed and the combined fit is repeated. For IO muons, ID tracks are extrapolated to the MS, in which at least three hits are required to match the trajectory. The muon track parameters are obtained by a fit using both the hits in the ID and MS and accounting for energy loss in the calorimeters. ST muons are identified by requiring the angle of an ID track to match at least one MS segment. The track parameters are in this case directly taken from the ID track.

The selection of muons follows what is referred to as the *Low-p_{T}* working point in Ref. [107]. At lower p_{T}, the background from non-prompt muons is large. The *Low-p_{T}* working point is optimised to separate between prompt muons and muons from light-hadron decays while maintaining a high reconstruction efficiency for prompt muons.

All muon candidates are required to have at least one hit in the pixel detector and five hits in the SCT and the trajectory is allowed to cross at most two times an active sensor without a hit being registered in it. Only the region covered by the ID ($|\eta| < 2.5$) is considered and only CB and IO muons are considered as candidates. For $|\eta| > 0.1$, muons are required to have two precision stations, which are MS stations with at least three hits in the MDT or CSC. For $|\eta| < 0.1$, muons with only one precision station are accepted, if at most one precision hole is associated to the track. Precision hole stations are MS stations in which, given the trajectory, at least three hits are expected, but are missing. For CB muons, the ratio of charge over momentum q/p measured for the ID and MS tracks are required to be compatible. The q/p compatibility

$$C_{q/p} = \frac{|q/p_{\mathrm{ID}} - q/p_{\mathrm{MS}}|}{\sqrt{\sigma^2(q/p_{\mathrm{ID}}) + \sigma^2(q/p_{\mathrm{MS}})}}, \tag{4.1}$$

where $q/p_{\mathrm{ID(MS)}}$ and $\sigma(q/p_{\mathrm{ID(MS)}})$ are the ratio measured in the ID (MS) and its uncertainty, respectively, is required to be smaller than seven. For muons with $p_{\mathrm{T}} < 18$ GeV, IO muons are required to be reconstructed as an ST muon independently in order to increase the purity and

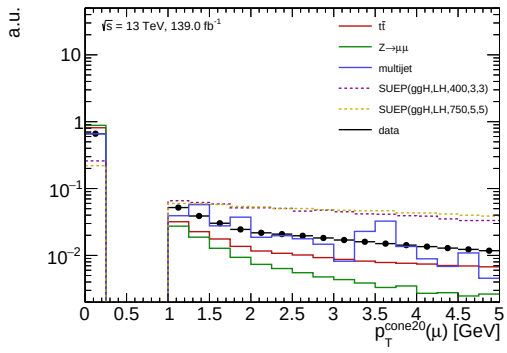

Figure 4.5: p_T^{cone20} distributions of *Low-*p_{T} muons with $|\eta| < 2.5$ and $p_{\text{T}} > 3$ GeV using events that passed the HLT_3mu6 trigger for data and $Z \to \mu\mu$, $t\bar{t}$, multijet and two signal samples.

only one precision station is required for $|\eta| < 1.3$ instead of two, because a significant fraction of muons with this momentum will not reach a second station. For muons with $p_{\text{T}} < 18$ GeV, three variables are defined to help reject muons from hadron decays, which have a kink in the trajectory due to the momentum carried away by the neutrino. The first variable is a measure of an excess of energy loss between the ID and the MS that cannot be explained by the energy loss measured in the calorimeter systems. The second and third variables are designed to spot discontinuities along the tracks by splitting the tracks in halves at hypothetical decay vertices and considering the angular distance in the bending plane between the two half tracks. A more detailed description of the three variables and the selection applied is given in Ref. [107].

A requirement on the isolation of muons can usually be used to reject muons stemming from heavy-flavour mesons like B or C mesons. However, muons are generally not well isolated in SUEP events either. In order to quantify the isolation of an object, p_T^{cone20} can be used, which is defined as the sum of the p_{T} of all tracks with $p_{\text{T}} > 1$ GeV in a cone of $R = 0.2$ around the object. As can be seen in Figure 4.5, which shows the distribution of p_T^{cone20} for muons in events passing HLT_3mu6 for two signal models, some MC background samples and data, muons are well isolated in processes producing prompt muons, like $Z \to \mu\mu$ and $t\bar{t}$, are less isolated in multijet events and are very poorly isolated in SUEP events. The isolation of muons in SUEP events is further reduced by the trigger selection, which introduces a bias towards events that are boosted in the transverse plane, as discussed in Section 4.4, and therefore the final state is compressed slightly towards one direction, increasing the particle density around each muon.

Loose requirements of $|d_0| < 2$ mm and $|\Delta z_0 sin\theta| < 3$ mm are chosen for the impact parameters, even though muons in SUEP events are expected to be prompt. The reason is that the muon displacement is used as an observable to form control regions after the preselection based on muon multiplicity.

The reconstruction efficiency of muons is corrected in simulation using per muon scale factors. Each muon is assigned a scale factor based on the ratio of the reconstruction efficiency measured in data over that measured in a $Z \to \mu\mu$ MC sample. The scale factors are provided by the ATLAS Muon Performance Working Group as a function of p_{T}, η, ϕ and period of data-taking. The scale factors of all muons in an event are multiplied together to get an event weight, which, when applied, corrects the distribution of reconstructed muon multiplicity. No correction is done for the track-to-vertex association selection efficiencies, as the d_0 and z_0 requirements are very

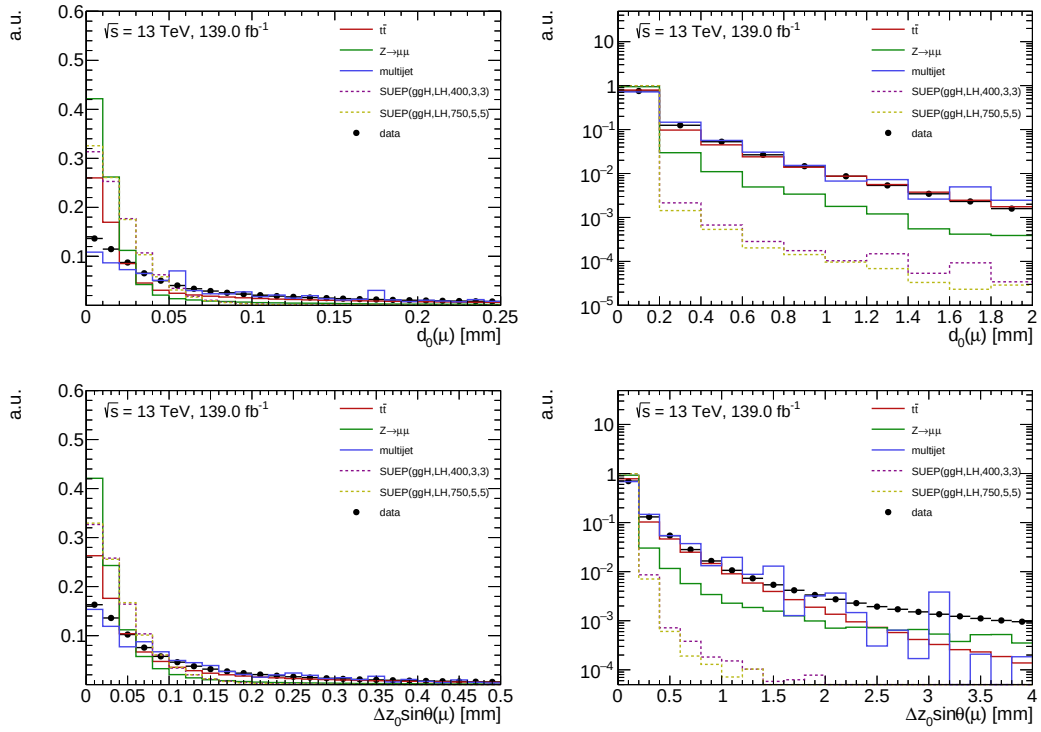

Figure 4.6: d_0 (top) and $\Delta z_0 \sin\theta$ (bottom) distributions of *Low-*p_{T} muons with $|\eta| < 2.5$ and $p_{\mathrm{T}} > 3$ GeV using events that passed the HLT_3mu6 trigger for data and $Z \to \mu\mu$, $t\bar{t}$, multijet and two signal samples on a linear scale (left) and logarithmic scale (right).

loose compared to the expected prompt signal, as can be seen in Figure 4.6. Muon momentum is corrected and smeared in MC based on calibrations provided by the ATLAS Muon Performance Working Group. The systematic uncertainties associated to muon reconstruction-efficiency correction and muon momentum correction are described in Section 4.13.

4.8 Trigger efficiency correction

The mismodelling of trigger efficiency in MC is corrected for with the use of a trigger scale factor to be applied to simulated events. Several factors contribute to the mismodelling. For one, the simulation does not take into consideration the evolution of the operational status of all the detector components involved, leading to different efficiencies as a function of η and ϕ. Furthermore, in MC, a step-function is used for the dependence of the L1 efficiency on the p_{T}. The p_{T}-dependence of the mismodelling in efficiency can in general be avoided by selecting muons that are well above the nominal threshold of the trigger. However, this is not possible for this analysis without severely affecting the sensitivity of the search. Figure 4.7 shows the efficiency measured in data for the single-muon trigger HLT_mu6. This trigger works in the same way as HLT_3mu6, but requires a single muon instead of three. It is only not continuously active, as it would otherwise trigger on much more events than the available computing resources allow for. It can therefore not be used to select events, but its decision is also registered for events that were saved by other triggers. Figure 4.7 indicates that the p_{T}-dependence of the efficiency reaches a plateau around 10 GeV. In SUEP events, muons will typically barely reach the threshold of 6 GeV. The trigger efficiency therefore needs to be corrected as function of the p_{T} of the muons involved.

Ideally, in order to correct the efficiency in MC, we would want to apply a scale factor on MC based on the ratio of efficiency of passing HLT_3mu6 measured in data over the efficiency measured in simulation. But the measurement cannot be performed for every possible combination of muons, each having different η, ϕ and p_{T}. The measurement needs to be parameterised somehow. To my knowledge, there are no suitable parametrisations for a multi-object trigger if the events considered can contain arbitrary number of said objects. What can be done instead is to measure the efficiency for individual muons to pass the single muon trigger HLT_mu6 and then, for an event with a given set of muons, one can calculate the probability of passing HLT_3mu6 from the combination of individual probabilities.

In order to measure the efficiency for HLT_mu6, a tag-and-probe methodology similar to that presented in Ref. [128] is used. An event selection targets $Z \to \mu\mu$ events and one of the muons from the Z-boson decay (the *tag*) is required to pass a common single-muon trigger. The other muon (the *probe*) is reconstructed with similar requirement as the ones used in this search (see Section 4.7). The efficiency is determined by assessing whether there is a muon-trigger object that fired HLT_mu6 and matches the reconstructed probe. Events are required to pass either HLT_mu20_iloose_L1MU15 or HLT_mu26_ivarmedium, which require a muon with $p_{\mathrm{T}} > 20$ GeV or $p_{\mathrm{T}} > 26$ GeV at the HLT, respectively, and are described in more detail in Reference [128]. Tighter requirements than those used in the main muon selection are made for the impact parameters of both the tag and the probe muons in order to increase the purity of $Z \to \mu\mu$ events in the selection. This restriction is not expected to bias the correction, since the scale factors will be applied only to SUEP events, which are prompt as well. However, a variation

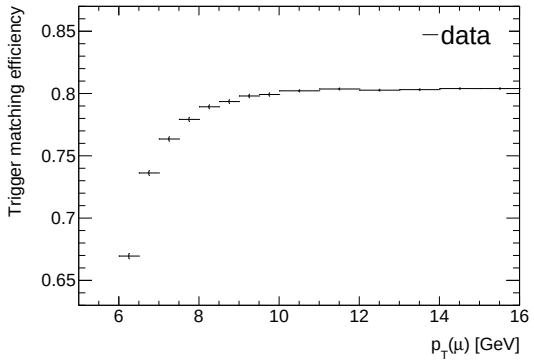

Figure 4.7: Efficiency of muon probes to be matched to HLT_mu6.

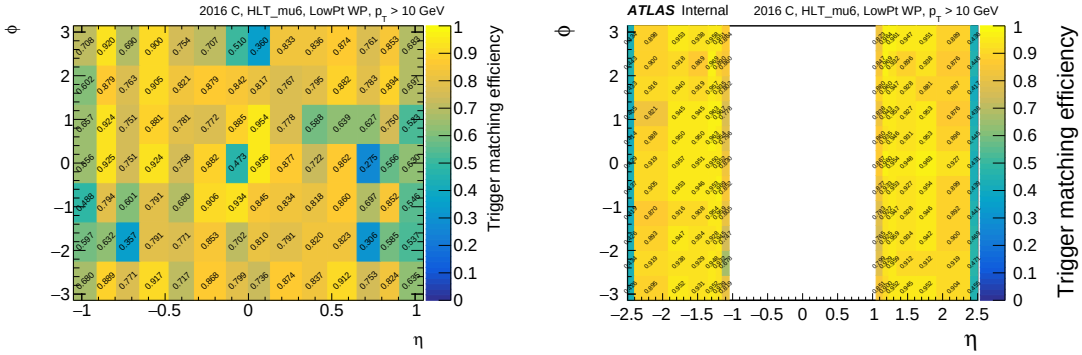

Figure 4.8: Trigger matching efficiencies for period C of 2016 for HLT_mu6 in the barrel region (left) and the end-cap region (right).

without any impact-parameter requirement is made and the difference is applied as a systematic uncertainty, as described in more detail in Section 4.13. As for the main muon selection, no requirement on the isolation is made. However, muons from $Z \rightarrow \mu\mu$ events are expected to be better isolated than muons from a SUEP decay. Once again, a systematic uncertainty is applied to account for the potential bias. The event is required to contain two muons with opposite charge and an invariant mass of within 10 GeV of the mass of the Z boson (91.2 GeV). The tag muon is required to be within $\Delta R = 0.1$ from an object that fired HLT_mu20_iloose_L1MU15 or HLT_mu26_ivarmedium. The quality requirements for the tag muon are suited for muons in the p_{T}-range that is typical for $Z \rightarrow \mu\mu$ and are described in details in Ref. [128]. The probe muon is considered to be matched if it is within $\Delta R = 0.1$ of a trigger object that fired HLT_mu6. The matching efficiency is measured separately for the barrel and end-cap regions, for each period of data-taking and in p_{T}, η and ϕ bins. In order to avoid large statistical uncertainties, only three p_{T}-bins of $[6, 8]$, $[8, 10]$ and $[10, \infty]$ GeV are used. The η and ϕ binning used is the same as in Ref. [128]. As an illustrative example, Figure 4.8 shows the efficiency map obtained in data for period C of 2016 for muons with $p_{\mathrm{T}} > 10$ GeV.

Knowing each of the efficiencies p_i at which the muons in the event are expected to pass HLT_mu6 and be matched to the trigger object, the probability of having at least three muons matched to HLT_mu6 objects, and therefore passing HLT_3mu6, can be calculated by assuming that each HLT_mu6 triggering event is independent. Since the number of successes for a set of

independent but non-identical Bernoulli trials follows Poisson's binomial distribution [133], the probability of obtaining at least three trigger-matched muons is

$$p(N_{\text{matched}\geq 3}) = \sum_{l=3}^{n} \left(\sum_{\substack{\mathcal{A}\subset\{1,\ldots,n\} \\ |\mathcal{A}|=l}} \left(\prod_{i\in\mathcal{A}} p_i \prod_{j\in\{1,\ldots,n\}\setminus\mathcal{A}} (1-p_j) \right) \right), \tag{4.2}$$

where n is the number of muons, the first summation is over the number of possible successes l and the inner summation over the set of possible sub-sets of muons with which the successes can be obtained. For example, an event with four reconstructed muons has a probability of

$$p = p_1p_2p_3(1-p_4) + p_1p_2p_4(1-p_3) + p_1p_3p_4(1-p_2) + p_2p_3p_4(1-p_1) + p_1p_2p_3p_4$$

to have at least three muons trigger-matched. In order to compute the sum in Eqn. 4.2, it is helpful to represent the success of each muon with a bit in an integer of a size of n bits. Then the sum over the set of possible sub-sets can be replaced by a sum over the integers in $\{0; n+1\}$ together with the requirement that the number of active bits in the integer is equal to the number of successes.

Applying this procedure means that the offline event selection also needs to include a requirement of at least three muons being trigger-matched to trigger objects. The scale factor applied as an event-weight to MC is

$$\text{SF} = \frac{p_{\text{Data}}(N_{\text{matched}\geq 3})}{p_{\text{MC}}(N_{\text{matched}\geq 3})}, \tag{4.3}$$

where p_{Data} is the probability obtained by using Eqn. 4.2 with the p_i being the efficiency measured in data, and p_{Data} the probability obtained with the p_i being the efficiency measured in a $Z \longrightarrow \mu\mu$ MC simulation. Both the data and MC samples used for this are in a special format prepared by the ATLAS Muon-trigger Performance Working Group. The MC sample is described in detail in Ref. [128].

4.9 Correction to track multiplicity

Even with tight track-to-vertex association requirements, there is a non-negligible contribution to the track multiplicity from pile-up interactions. This contribution depends on the density of pile-up interactions around the primary interaction vertex and therefore on the current average number of interactions per crossing (μ), the BS size and the position of the PV within the BS. During simulation, which is done before all data is taken, neither μ nor the BS size can be adjusted to the distributions observed in data. μ is corrected for by assigning an LHC fill to each simulated event and reweight all events such that the distribution matches that observed in data. The BS position and size are simulated with constant values for all events and therefore cannot be corrected through a reweighting of events. Instead, the track multiplicity is corrected for pile-up contribution directly. This can be done if the number of expected tracks from pile-up interactions $N^{\text{PU}}_{\text{tracks}}$ for a given z_{PV} and μ is known. Then, the expected pile-up contribution can

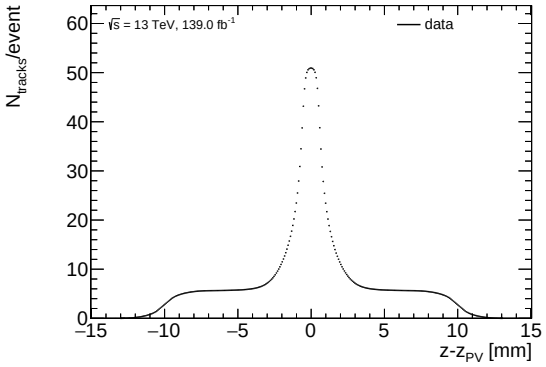

Figure 4.9: Track multiplicity obtained at position $z - z_{\mathrm{PV}}$.

be subtracted from the total number of tracks to obtain a track multiplicity whose average is independent from the pile-up conditions. Doing so for both data and MC removes the effect of mismodelling of the pile-up contribution to track multiplicity.

In order to measure $N^{\mathrm{PU}}_{\mathrm{tracks}}$, the track multiplicity is evaluated additionally at an imaginary primary vertex that is shifted longitudinally from the actual PV. If the shift is sufficiently large, the track multiplicity obtained at the shifted position should be mostly unaffected by the primary interaction and only depend on pile-up interactions from the vicinity of the imaginary PV. Figure 4.9 shows the track multiplicity in data obtained as a function of a shift $z - z_{\mathrm{PV}}$ in the position of the imaginary PV. Near $z - z_{\mathrm{PV}} = 0$ mm, the primary interaction contributes to the multiplicity, as expected. The distribution drops at $z - z_{\mathrm{PV}} = \pm 10$ mm. These are artefacts that are due to a rejection of tracks made during a stage of data-processing meant to reduce the size of datasets. Between roughly $|z - z_{\mathrm{PV}}| = 5$ mm and $|z - z_{\mathrm{PV}}| = 8$ mm, the distribution is almost flat. Only a slight negative slope towards higher shifts is expected in this region, which is due to the fact that the primary interaction vertex is more likely to be near the centre of the BS, where the pile-up density is highest. A shift of $z - z_{\mathrm{PV}} = 6.5$ mm is used to perform the measurement.

As mentioned in Section 2.1 and shown in Figure 2.4, the BS position and size changes for every fill and is monitored by the HLT system. Therefore, measuring $N^{\mathrm{PU}}_{\mathrm{tracks}}$ as a function of z would mean that the measurement has to be done for every fill. Instead, $N^{\mathrm{PU}}_{\mathrm{tracks}}$ is measured as a function of the relative position within the BS $(z - z_{\mathrm{BS}})/\sigma(z_{\mathrm{BS}})$, where z_{BS} is the average centre of the BS in a fill and $\sigma(z_{\mathrm{BS}})$ its standard deviation. Figure 4.10 shows $N^{\mathrm{PU}}_{\mathrm{tracks}}$ as a function of z and $(z - z_{\mathrm{BS}})/\sigma(z_{\mathrm{BS}})$ for two runs with significantly different BS positions and sizes.

Figure 4.11 shows $N^{\mathrm{PU}}_{\mathrm{tracks}}$ measured in data and shows that there is a linear dependence on μ and a Gaussian-shaped dependence on the position within the BS. In order to smooth out local statistical fluctuations, the measurement is fitted using the χ^2-method to

$$N^{\mathrm{PU}}_{\mathrm{tracks}}(z, \mu) = \mu A e^{-\frac{1}{2}\left(\frac{(z - z_{\mathrm{BS}})/\sigma(z_{\mathrm{BS}})}{B}\right)^2} + N_0, \tag{4.4}$$

where A, B and N_0 are free parameters. For MC, a $Z \rightarrow \mu\mu$ sample is used. It has the same simulated BS parameters as the SUEP signal samples, so the result can be used to correct the signal samples as well. Table 4.5 shows the obtained fitted parameters for data and MC, together

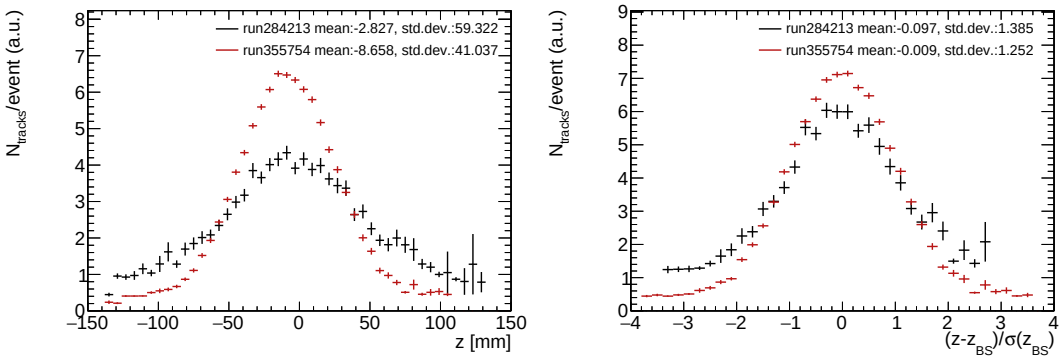

Figure 4.10: $N^{\mathrm{PU}}_{\mathrm{tracks}}$ as a function of z (left) and $(z - z_{\mathrm{BS}})/\sigma(z_{\mathrm{BS}})$ (right) for the 2015 fill 284213 with mean $z_{\mathrm{BS}} = -3.22$ mm and mean $sigma(z_{\mathrm{BS}}) = 42.8$ and the 2018 fill 355754 with mean $z_{\mathrm{BS}} = -8.17$ mm and mean $sigma(z_{\mathrm{BS}}) = 34.0$.

Table 4.5: Fit results for $N^{\mathrm{PU}}_{\mathrm{tracks}}(z, \mu)$ for data (top rows) and $Z \to \mu\mu$ MC (bottom rows) with the fit uncertainties.

	A	B	N_0
data (SUEP selection)	0.2138 ± 0.0002	1.0003 ± 0.0012	0.5092 ± 0.0021
data ($Z \to \mu\mu$ selection)	0.2124 ± 0.0001	1.0050 ± 0.0004	0.5173 ± 0.0007
MC (SUEP selection)	0.1906 ± 0.0012	0.9623 ± 0.0055	0.3236 ± 0.0102
MC ($Z \to \mu\mu$ selection)	0.1918 ± 0.0001	1.0054 ± 0.0003	0.5088 ± 0.0005

with the fitted parameters obtained with an alternative event-selection used for validation and described in Section 4.9.1.

Now, the expected number of pile-up tracks for a given z and μ can be evaluated by using the fitted $N^{\mathrm{PU}}_{\mathrm{tracks}}(z, \mu)$. The corrected track multiplicity is

$$N^{\mathrm{c}}_{\mathrm{tracks}} = N_{\mathrm{tracks}} - N^{\mathrm{PU}}_{\mathrm{tracks}}(z, \mu).$$

Figures 4.12 and 4.13 show that $N^{\mathrm{c}}_{\mathrm{tracks}}$, in contrast to N_{tracks}, is mostly uncorrelated to z_{PV} and μ. By applying the correction, the Pearson correlation coefficient between track multiplicity and μ is reduced from 0.10 to 0.02 in data and 0.09 to 0.007 in MC and between track multiplicity and z_{PV}, measured only for positive z_{PV}, is reduced from −0.10 to −0.008 in data and from −0.10 to −0.007 in MC.

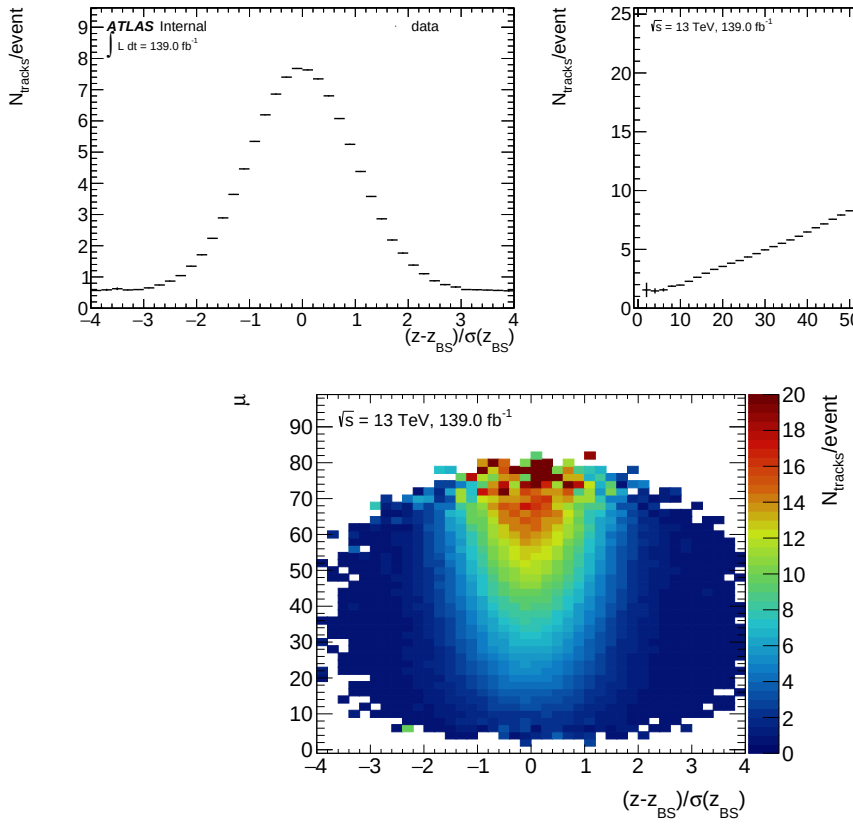

Figure 4.11: $N^{\mathrm{PU}}_{\mathrm{tracks}}$ as a function of $(z_{\mathrm{PV}} - z_{\mathrm{BS}})/\sigma(z_{\mathrm{BS}})$ (top-left), μ (top-right) and both (bottom).

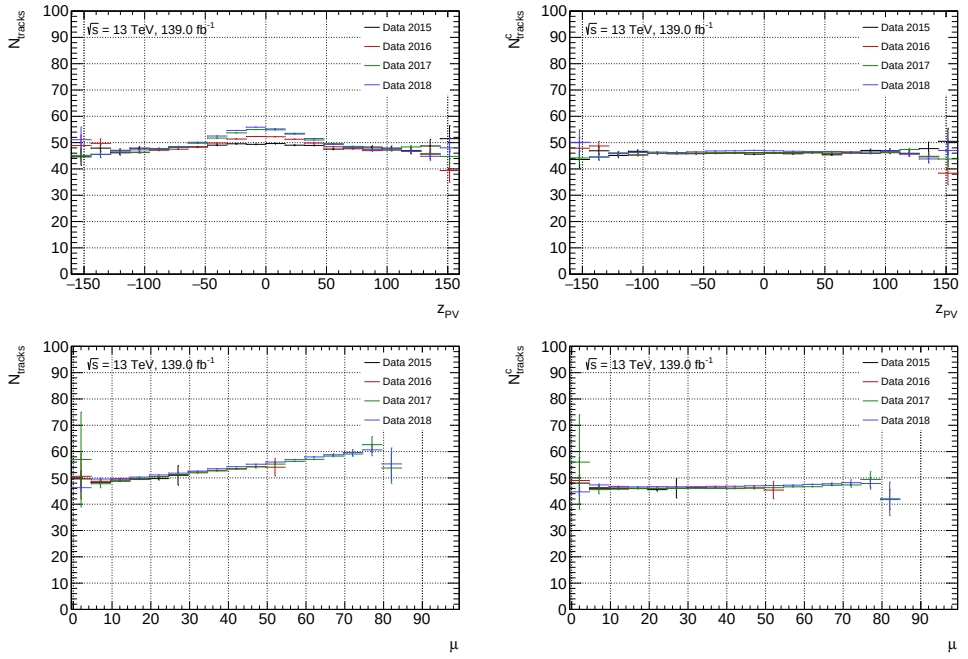

Figure 4.12: N_{tracks} (left) and $N^{\mathrm{c}}_{\mathrm{tracks}}$ (right) as a function of z_{PV} (top) and μ (bottom) for different years of data-taking.

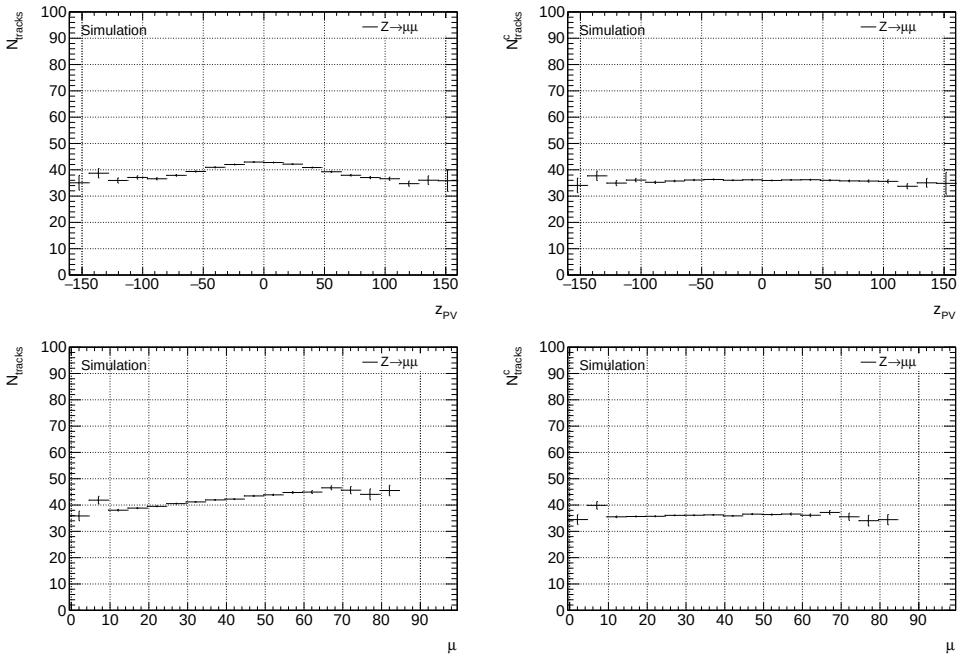

Figure 4.13: N_{tracks} (left) and $N^{\text{c}}_{\text{tracks}}$ (right) as a function of z_{PV} (top) and μ (bottom) for $Z \to \mu\mu$.

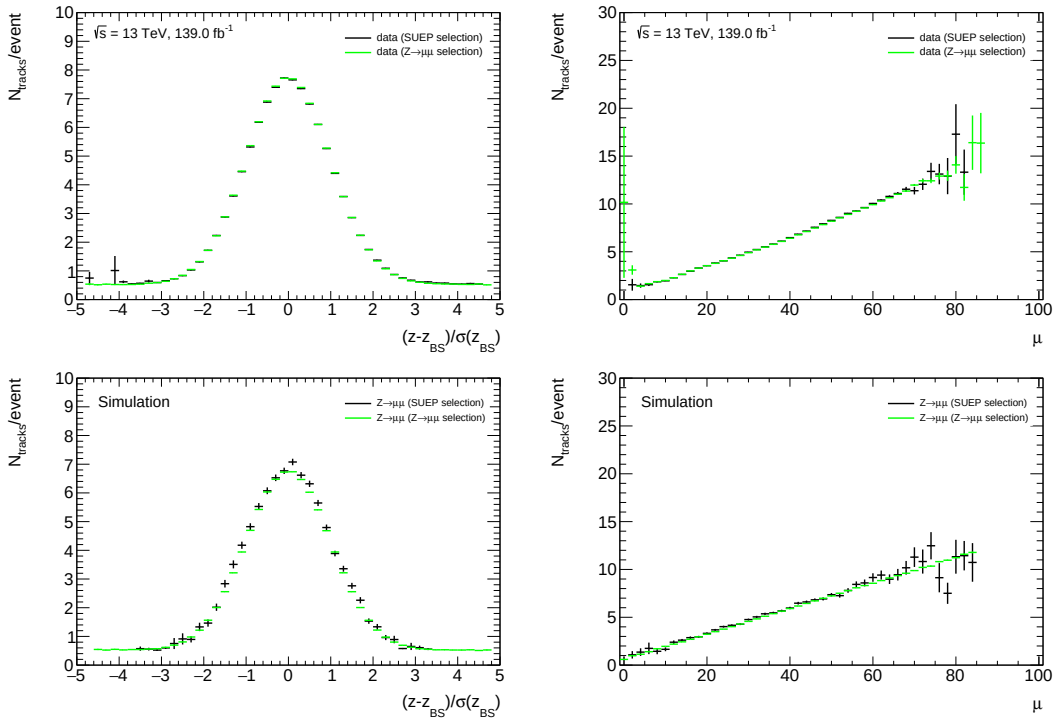

Figure 4.14: $N^{\mathrm{PU}}_{\mathrm{tracks}}$ as a function of $(z_{\mathrm{PV}} - z_{\mathrm{BS}})/\sigma(z_{\mathrm{BS}})$ for $30 < \mu < 35$ (left), as a function of μ for $|(z_{\mathrm{PV}} - z_{\mathrm{BS}})/\sigma(z_{\mathrm{BS}})| < 0.5$ (right) for data (top) and MC (bottom).

4.9.1 Validation of track multiplicity correction

In order to support the validity of the measurements of $N^{\mathrm{PU}}_{\mathrm{tracks}}$ and to derive an uncertainty to be attributed to the measurement, it is repeated with an alternative selection, namely a selection similar to that used to measure the HLT_mu6 efficiency, described in Section 4.8, which targets events with Z bosons decaying to two muons. This selection will be called $Z \rightarrow \mu\mu$ selection in the following. For this selection, the *Medium* quality and *FCTightTrackOnly_FixedRad* isolation working points are used for the muon selection. They are well suited to efficiently select the well isolated prompt muons decaying from Z bosons and are described in Ref. [107]. Furthermore, muons are required to have $p_{\mathrm{T}} > 25$ GeV, $|\eta| < 2.4$, $d_0^{\mathrm{sig}}(\mu_1) < 3$ and $|\Delta z_0 sin\theta| < 0.5$ mm. The data quality requirements for this selection are identical to the ones of the main selection of this analysis, described in Section 4.10. Events that are selected by either of the di-muon triggers HLT_2mu14 or HLT_2mu10, which require muons of $p_{\mathrm{T}} > 14$ and $p_{\mathrm{T}} > 10$, respectively, are selected. Events containing muons with a bad ID–MS compatibility ($C_{q/p} < 0.2$) are vetoed. Events are required to contain exactly two muons of opposite charge and their invariant mass is required to be within $[80, 100]$ GeV. The same measurement of $N^{\mathrm{PU}}_{\mathrm{tracks}}$ as described previously is performed for both data and MC. Figure 4.14 shows that the measurements for both the $Z \rightarrow \mu\mu$ selection described in this section and the selection using three muons described previously give similar results for both data and MC.

The resulting fitted parameters together with the uncertainties on the fitted values are shown in Table 4.5.

4.10 Offline event selection

Only events that are deemed of sufficient quality are selected. The quality requirements, described by the ATLAS data-quality operation [134], are based on the operational status of the sub-detector systems. All events are required to have a primary vertex with at least two associated tracks. In order to apply the trigger scale factor described in Section 4.8, at least three muons need to be trigger-matched. After the online event selection, the processes that are expected to contribute are processes that can contain a high number of muons in the final state. This includes:

- Top-quark pair production ($t\bar{t}$). Top quarks almost always decay to bottom quarks through emission of a W boson. The W bosons can produce prompt muons and one or more additional muons can stem from each of the bottom quarks.
- Top-quark pair production with associated production of a vector boson ($t\bar{t} + V$), where additional prompt muons can stem from the vector boson.
- Z-boson production with decay to two muons ($Z \rightarrow \mu\mu$), where additional muons can stem from additional QCD radiation.
- Diboson and triboson production, but specifically $ZZ \rightarrow \mu\mu\mu\mu$.
- Heavy-flavour multijet.

Two observables, $\overline{p_{\mathrm{T}}}(\mu_i)$, the average p_{T} of all muons in the event, and the muon multiplicity N_μ are used in order to increase the signal-to-background ratio. $\overline{p_{\mathrm{T}}}(\mu_i)$ is required to be below 10 GeV, which reduces drastically contributions from events containing prompt, high-p_{T} muons that originate from the decay of heavy particles like top quarks or Z bosons. In order to verify this claim, MC background samples are used. Only the most relevant subset of the processes listed above have been analysed more closely, namely $t\bar{t}$,$t\bar{t} + Z$, $Z \rightarrow \mu\mu$, $ZZ \rightarrow \mu\mu\mu\mu$, WWZ and multijet. Other triboson processes can also contain a high number muons in the final state, but their production cross-sections are too low to contribute significantly. Figure 4.15 shows the distribution of these observables and the relative contribution for different SM background processes for events passing the trigger and the offline trigger requirement and Table 4.6 shows the cut-flow for data and MC samples for some of the background processes. A multijet sample is not included in the table, as the available statistics is low and the normalisation is not reliable. But it can be assumed that the number of multijet events is the difference between data and the other background processes. The figures and the table confirm that the contributions from processes involving the decay of heavy particles is low for events with $\overline{p_{\mathrm{T}}}(\mu_i) < 10$ GeV. Besides multijet, the only process that might not be negligible after the preselection is $t\bar{t}$ with 200 expected events. The total number of observed events after applying the last selection criteria needs to be blinded, since a potential contribution from a signal would be non-negligible at this point. However, the number of observed events after preselection excluding the SR, defined in Section 4.12, can be given. This gives a lower bound on the number of events observed after preselection for data, which is 27 277. The $t\bar{t}$ contribution after preselection is therefore at most 0.73%.

Muon multiplicity can vary greatly between signal samples. For the lep-had benchmark, it ranges from about 6 per event for signals with $M = 125$ GeV up to around 20 for signals with

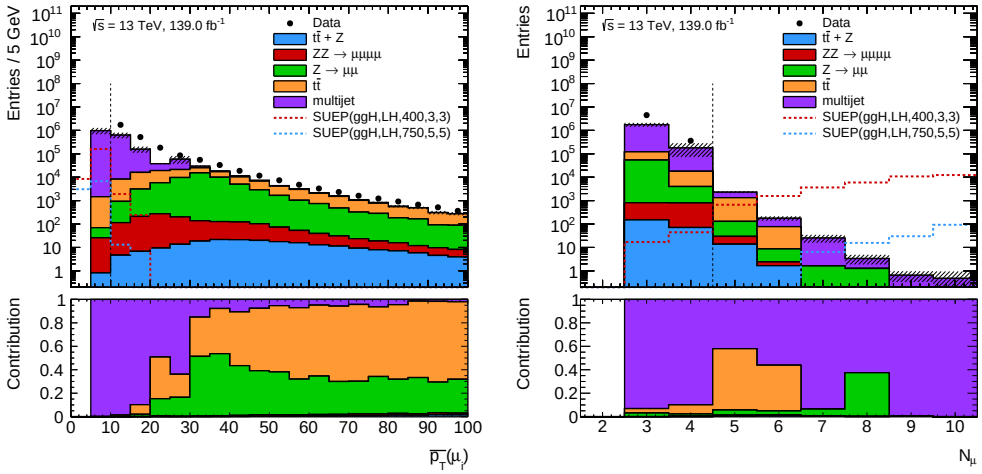

Figure 4.15: Distribution (top) and relative background contributions (bottom) of $\overline{p_T}(\mu_i)$ (left) and N_μ (right).

Table 4.6: Cut-flows for data and background MC expectation. Cuts are applied successively from left to right. Errors are statistical uncertainties and percentages show the efficiency with respect to the previously applied selection.

process	HLT_3mu6	$N_{\mu^{\text{matched}}} \geq 3$		$\overline{p_T}(\mu_i) < 10$ GeV		$N_\mu \geq 5$	
data	43 384 000 ± 7000	17 722 000 ± 4000	(40.9%)	7 988 500 ± 2800	(45.1%)	blinded	
$t\bar{t}$	322 500 ± 900	317 000 ± 900	(98.3%)	5520 ± 120	(1.7%)	200 ± 22	(3.6%)
$Z \to \mu\mu$	219 000 ± 500	217 200 ± 500	(99.2%)	203 ± 16	(0.1%)	2.4 ± 1.7	(1.2%)
$ZZ \to \mu\mu\mu\mu$	5389 ± 11	5343 ± 11	(99.2%)	94.5 ± 0.9	(1.8%)	1.19 ± 0.10	(1.3%)
$t\bar{t} + Z$	911.9 ± 2.9	898.6 ± 2.9	(98.6%)	3.36 ± 0.17	(0.4%)	0.30 ± 0.06	(9.0%)
WWZ	1911 ± 16	1901 ± 16	(99.5%)	0.47 ± 0.25	(0.0%)	0.10 ± 0.10	(22.0%)

$M = 750$ GeV. Requiring at least five muons reduces the contribution from all SM backgrounds while still being very inclusive towards the spectrum of targeted signals models. Tables 4.7 and 4.8 show the cut-flows for signal models. They show that for almost all signal models, only the trigger selection significantly affects the total selection efficiency. Some signal models of high mediator and dark-pion mass and high temperature, like SUEP(ggH, 750, 5, 7.5), pass all selection steps at close to 100% efficiency.

Table 4.7: Cut-flows for signal models of the lep-had branching-ratio benchmark. Cuts are applied successively from left to right. Errors are statistical uncertainties and percentages show the efficiency with respect to the previously applied selection. The percentage in the first column refers to the total initial number of events produced with 139 fb^{-1}.

process	HLT_3mu6		$N_{\mu^{\text{matched}}} \geq 3$		$\overline{p_T}(\mu_i) < 10$ GeV		$N_\mu \geq 5$	
SUEP(ggH,LH,125,1.5,1)	6370 ± 320	(1%)	6370 ± 320	(100%)	6020 ± 310	(94%)	5950 ± 300	(99%)
SUEP(ggH,LH,125,1.5,1.5)	13 100 ± 500	(2%)	13 100 ± 500	(100%)	12 100 ± 500	(93%)	11 800 ± 500	(97%)
SUEP(ggH,LH,125,1.5,2.25)	26 200 ± 700	(4%)	26 100 ± 700	(99%)	22 100 ± 600	(85%)	20 600 ± 600	(94%)
SUEP(ggH,LH,125,3,2)	28 900 ± 800	(5%)	28 700 ± 800	(99%)	24 600 ± 800	(86%)	23 200 ± 700	(94%)
SUEP(ggH,LH,125,3,3)	52 200 ± 1100	(9%)	51 800 ± 1100	(99%)	42 500 ± 1000	(82%)	38 900 ± 900	(92%)
SUEP(ggH,LH,125,3,4.5)	85 900 ± 1400	(15%)	85 300 ± 1400	(99%)	62 500 ± 1200	(73%)	54 200 ± 1100	(87%)
SUEP(ggH,LH,125,5,3.33)	69 200 ± 1200	(12%)	68 800 ± 1200	(100%)	54 500 ± 1100	(79%)	47 600 ± 1000	(87%)
SUEP(ggH,LH,125,5,5)	101 700 ± 1500	(17%)	101 300 ± 1500	(100%)	71 600 ± 1300	(71%)	62 200 ± 1200	(87%)
SUEP(ggH,LH,125,5,7.5)	116 800 ± 1600	(20%)	116 000 ± 1600	(99%)	64 500 ± 1200	(56%)	53 800 ± 1100	(83%)
SUEP(ggH,LH,400,1.5,1)	16 800 ± 1600	(1%)	16 700 ± 1600	(100%)	16 600 ± 1600	(99%)	16 600 ± 1600	(100%)
SUEP(ggH,LH,400,1.5,1.5)	54 400 ± 1400	(4%)	54 000 ± 1400	(99%)	53 300 ± 1400	(99%)	53 200 ± 1400	(100%)
SUEP(ggH,LH,400,1.5,2.25)	225 300 ± 2900	(17%)	223 800 ± 2900	(99%)	221 800 ± 2900	(99%)	221 200 ± 2900	(100%)
SUEP(ggH,LH,400,3,2)	252 000 ± 4000	(19%)	250 000 ± 4000	(99%)	248 000 ± 4000	(99%)	247 000 ± 4000	(100%)
SUEP(ggH,LH,400,3,3)	666 000 ± 6000	(50%)	662 000 ± 6000	(99%)	652 000 ± 6000	(99%)	652 000 ± 6000	(100%)
SUEP(ggH,LH,400,3,4.5)	1 001 000 ± 7000	(76%)	997 000 ± 7000	(100%)	957 000 ± 7000	(96%)	956 000 ± 7000	(100%)
SUEP(ggH,LH,400,5,3.33)	834 000 ± 7000	(63%)	829 000 ± 7000	(99%)	814 000 ± 7000	(98%)	814 000 ± 7000	(100%)
SUEP(ggH,LH,400,5,5)	1 066 000 ± 8000	(81%)	1 063 000 ± 8000	(100%)	991 000 ± 7000	(93%)	990 000 ± 7000	(100%)
SUEP(ggH,LH,400,5,7.5)	1 133 000 ± 8000	(86%)	1 131 000 ± 8000	(100%)	822 000 ± 7000	(73%)	820 000 ± 7000	(100%)
SUEP(ggH,LH,750,1.5,1)	1380 ± 70	(2%)	1350 ± 70	(98%)	1350 ± 70	(100%)	1350 ± 70	(100%)
SUEP(ggH,LH,750,1.5,1.5)	6530 ± 150	(7%)	6470 ± 150	(99%)	6460 ± 150	(100%)	6460 ± 150	(100%)
SUEP(ggH,LH,750,1.5,2.25)	35 470 ± 350	(40%)	35 230 ± 350	(99%)	35 150 ± 350	(100%)	35 150 ± 350	(100%)
SUEP(ggH,LH,750,3,2)	38 800 ± 400	(44%)	38 600 ± 400	(99%)	38 500 ± 400	(100%)	38 500 ± 400	(100%)
SUEP(ggH,LH,750,3,3)	76 500 ± 500	(86%)	76 300 ± 500	(100%)	76 100 ± 500	(100%)	76 100 ± 500	(100%)
SUEP(ggH,LH,750,3,4.5)	86 600 ± 600	(97%)	86 600 ± 600	(100%)	85 300 ± 600	(98%)	85 300 ± 600	(100%)
SUEP(ggH,LH,750,5,3.33)	83 400 ± 600	(94%)	83 300 ± 600	(100%)	82 800 ± 600	(99%)	82 800 ± 600	(100%)
SUEP(ggH,LH,750,5,5)	87 500 ± 600	(98%)	87 500 ± 600	(100%)	85 100 ± 600	(97%)	85 100 ± 600	(100%)
SUEP(ggH,LH,750,5,7.5)	88 200 ± 600	(99%)	88 200 ± 600	(100%)	70 000 ± 500	(79%)	70 000 ± 500	(100%)

Table 4.8: Cut-flows for signal models with ggH production and the lep or had benchmarks for branching ratio. Cuts are applied successively from left to right. Errors are statistical uncertainties and percentages show the efficiency with respect to the previously applied selection. The percentage in the first column refers to the total initial number of events produced with 139 fb^{-1}.

process	HLT_3mu6		$N_{\mu^{\text{matched}}} \geq 3$		$\overline{p_T}(\mu_i) < 10$ GeV		$N_\mu \geq 5$	
SUEP(ggH,H,400,1.5,1)	2800 ± 400	(0%)	2800 ± 400	(100%)	2700 ± 400	(97%)	2600 ± 400	(95%)
SUEP(ggH,H,400,1.5,1.5)	9300 ± 700	(1%)	9300 ± 700	(100%)	8900 ± 700	(95%)	8800 ± 700	(99%)
SUEP(ggH,H,400,1.5,2.25)	30 900 ± 1200	(2%)	30 500 ± 1200	(99%)	28 600 ± 1200	(94%)	27 100 ± 1100	(95%)
SUEP(ggH,H,400,3,2)	45 000 ± 1500	(3%)	44 300 ± 1500	(99%)	41 900 ± 1400	(94%)	38 500 ± 1400	(92%)
SUEP(ggH,H,400,3,3)	137 600 ± 2600	(10%)	136 300 ± 2600	(99%)	126 100 ± 2500	(93%)	117 100 ± 2400	(93%)
SUEP(ggH,H,400,3,4.5)	273 000 ± 4000	(21%)	270 000 ± 4000	(99%)	233 500 ± 3400	(87%)	217 700 ± 3300	(93%)
SUEP(ggH,H,400,5,3.33)	208 700 ± 3200	(16%)	206 400 ± 3200	(99%)	187 400 ± 3000	(91%)	175 800 ± 2900	(94%)
SUEP(ggH,H,400,5,5)	324 000 ± 4000	(24%)	321 000 ± 4000	(99%)	264 000 ± 4000	(82%)	242 900 ± 3500	(92%)
SUEP(ggH,H,400,5,7.5)	380 000 ± 4000	(29%)	377 000 ± 4000	(99%)	221 700 ± 3300	(59%)	197 300 ± 3200	(89%)
SUEP(ggH,H,750,1.5,1)	330 ± 40	(0%)	320 ± 40	(98%)	320 ± 40	(99%)	320 ± 40	(100%)
SUEP(ggH,H,750,1.5,1.5)	980 ± 60	(1%)	960 ± 60	(98%)	950 ± 60	(99%)	950 ± 60	(100%)
SUEP(ggH,H,750,1.5,2.25)	4160 ± 120	(5%)	4080 ± 120	(98%)	4020 ± 120	(98%)	3990 ± 120	(99%)
SUEP(ggH,H,750,3,2)	8210 ± 160	(9%)	8100 ± 160	(99%)	7980 ± 160	(99%)	7910 ± 160	(99%)
SUEP(ggH,H,750,3,3)	26 790 ± 300	(30%)	26 420 ± 300	(99%)	25 990 ± 290	(98%)	25 830 ± 290	(99%)
SUEP(ggH,H,750,3,4.5)	47 000 ± 400	(53%)	46 700 ± 400	(99%)	44 400 ± 400	(95%)	44 100 ± 400	(99%)
SUEP(ggH,H,750,5,3.33)	36 960 ± 350	(42%)	36 560 ± 350	(99%)	35 690 ± 350	(98%)	35 430 ± 350	(99%)
SUEP(ggH,H,750,5,5)	52 900 ± 400	(59%)	52 400 ± 400	(99%)	48 100 ± 400	(92%)	47 700 ± 400	(99%)
SUEP(ggH,H,750,5,7.5)	58 100 ± 500	(65%)	57 700 ± 500	(99%)	39 400 ± 400	(68%)	38 800 ± 400	(98%)
SUEP(ggH,L,125,1.5,1)	7160 ± 350	(1%)	7140 ± 350	(100%)	6710 ± 330	(94%)	6590 ± 330	(98%)
SUEP(ggH,L,125,1.5,1.5)	16 700 ± 500	(3%)	16 700 ± 500	(100%)	15 200 ± 500	(91%)	14 800 ± 500	(98%)
SUEP(ggH,L,125,1.5,2.25)	32 100 ± 800	(5%)	31 900 ± 800	(99%)	27 800 ± 700	(87%)	26 800 ± 700	(96%)
SUEP(ggH,L,125,5,3.33)	78 900 ± 1300	(14%)	78 600 ± 1300	(100%)	65 500 ± 1200	(83%)	61 200 ± 1200	(93%)
SUEP(ggH,L,125,5,5)	123 400 ± 1700	(21%)	122 900 ± 1700	(100%)	95 800 ± 1500	(78%)	88 000 ± 1400	(92%)
SUEP(ggH,L,125,5,7.5)	151 800 ± 1900	(26%)	151 100 ± 1900	(100%)	97 100 ± 1500	(64%)	87 000 ± 1400	(90%)

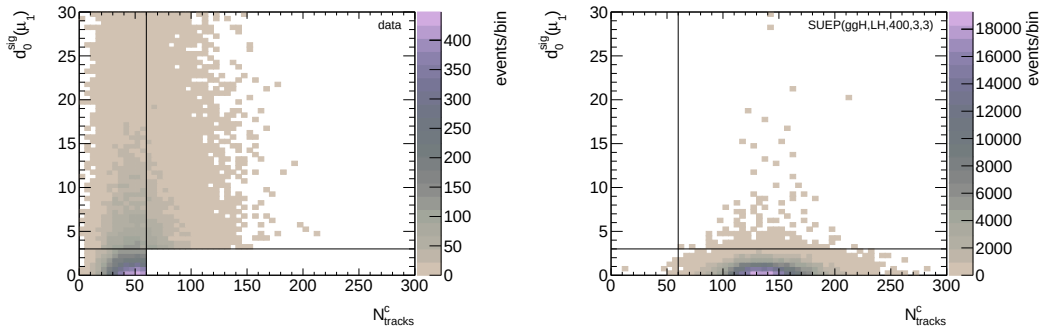

Figure 4.16: Yields for data (left) and expected yield for the signal SUEP(ggH, LH, 400, 3, 3) in the ABCD-plane.

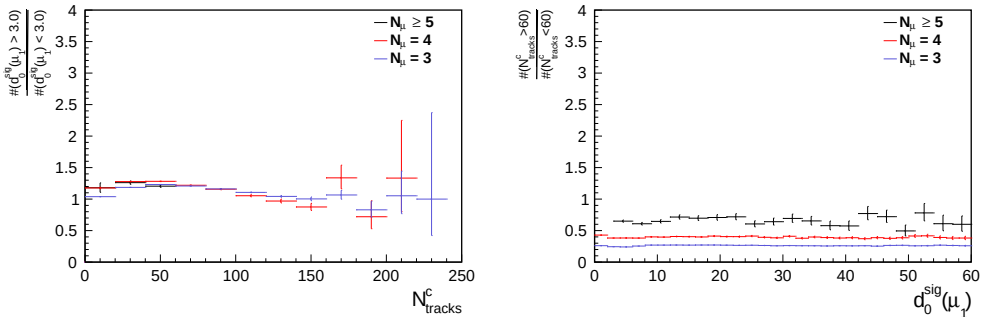

Figure 4.17: Ratio of the number of events with $d_0^{\text{sig}}(\mu_1) > 3$ over the number of events with $d_0^{\text{sig}}(\mu_1) < 3.0$ (left) and ratio of the number of events with $N^{\text{c}}_{\text{tracks}} > 60$ over the number of events with $N^{\text{c}}_{\text{tracks}} < 50$ (right) for data with preselections requiring $N_\mu = 3, 4$ or $N_\mu \geq 5$

4.11 Background estimation

As discussed previously, the expected dominant background after the preselection is heavy-flavour multijet events. Charged pions and kaons can also decay into muons, but with significantly longer lifetimes than heavy-flavour mesons. Heavily displaced decays into muons are rejected by the muon reconstruction algorithm. Light-flavoured mesons are therefore not expected to contribute significantly. Since we target signal models with prompt decays and since B and D mesons have significant lifetimes, muon displacement is a further handle to discriminate signal from background. Apart from some caveats discussed below, the number of tracks in the event is expected to be largely uncorrelated to muon displacement for the heavy-flavour multijet background. An observable measuring the displacement of muons together with track multiplicity could therefore be used as variables for the ABCD-method. In order to measure muon displacement, different variables were considered and the correlation to track multiplicity and the performance at discriminating signal from background were investigated for each of them. The variables considered are based on the components of the impact parameters of muons, either taken as an average over all muons in the event or from a specific muon in the event. No significant difference in terms of background rejection was found between the variables considered. $d_0^{\text{sig}}(\mu_1) = \frac{|d_0|}{\sigma(d_0)}$, the d_0 *significance* of the leading muon, was chosen as the correlation to $N^{\text{c}}_{\text{tracks}}$ was the lowest. Figure 4.16 shows the distributions of events for data and a signal sample

Table 4.9: Yields in regions with $N_\mu = 3, 4$ and $N_\mu \geq 5$. The selection described in Section 4.10 (except the selection on N_μ) is also applied.

	$N_\mu = 3$	$N_\mu = 4$	$N_\mu \geq 5$
data	7 285 500 ± 2700	660 900 ± 800	blinded
$t\bar{t}$	4020 ± 100	1300 ± 60	200 ± 22
$Z \to \mu\mu$	166 ± 14	35 ± 6	2.4 ± 1.7
$ZZ \to \mu\mu\mu\mu$	55.8 ± 0.7	37.5 ± 0.6	1.19 ± 0.10
$t\bar{t} + Z$	1.99 ± 0.13	1.07 ± 0.10	0.30 ± 0.06
WWZ	0.37 ± 0.23	$\lessapprox 0.1$	0.10 ± 0.10

in the plane spanned by $d_0^{\text{sig}}(\mu_1)$ and $N_{\text{tracks}}^{\text{c}}$. The region $d_0^{\text{sig}}(\mu_1) < 3.0 \cap N_{\text{tracks}}^{\text{c}} \geq 60$ is blinded, as it is used as SR. The Pearson correlation coefficient between $N_{\text{tracks}}^{\text{c}}$ and $d_0^{\text{sig}}(\mu_1)$ for the region $N_{\text{tracks}}^{\text{c}} < 60$ is 0.0005. The correlation can be further investigated by considering how the ratio of the number of events passing $N_{\text{tracks}}^{\text{c}} > 60$ ($d_0^{\text{sig}}(\mu_1) > 3.0$) over the number of events passing $N_{\text{tracks}}^{\text{c}} < 60$ ($d_0^{\text{sig}}(\mu_1) < 3.0$) evolves for different bins in $d_0^{\text{sig}}(\mu_1)$ ($N_{\text{tracks}}^{\text{c}}$). This can only be done for the regions in the plane that are not blinded. However, it can be done for the whole plane for events passing alternative preselections. This was done for preselections requiring $N_\mu = 3$ or $N_\mu = 4$, instead of $N_\mu \geq 5$. Table 4.9 shows that the background composition is also dominated by multijet for these preselections. The result is shown in Figure 4.17, which shows that the ratios are altogether relatively flat, indicating a low correlation between both variables. For the selections with $N_\mu = 3$ and $N_\mu = 4$, Figure 4.17 shows that the relative number of events with high $d_0^{\text{sig}}(\mu_1)$ does slightly decrease with increasing $N_{\text{tracks}}^{\text{c}}$. However, the correlation coefficients are still very low with 0.016 for $N_\mu = 3$ and -0.003 for $N_\mu = 4$. A small correlation is to be expected: Even though the number of charged particles stemming from the decay of the hadrons does not depend on the time it took for the hadrons to decay, different hadron species have different lifetimes and, on average, decay into a different number of charged particles. As was shown by the OPAL collaboration at LEP, a c quark adds on average 0.7 charged particles to the event, compared to events containing only light flavoured quarks, whereas a b quark adds on average 2.8 charged particles to the event [135]. Neutral and charged D mesons, for example, have lifetimes of approximately 0.4 and 1 ps, respectively, whereas neutral and charged B mesons have lifetimes of 1.5 and 1.6 ps, respectively [121]. Additional correlation comes from the fact that muons are selected with looser impact parameter requirements than tracks. Tracks that originate from a vertex that is displaced by more than 0.5 mm from the primary vertex, either longitudinally or radially, will not be selected. Therefore, for the same hadron species, a higher $d_0^{\text{sig}}(\mu_1)$ value leads to slightly lower $N_{\text{tracks}}^{\text{c}}$. In order to account for these small correlations, a non-closure uncertainty is added to the background estimate.

4.12 Region definitions

For increasing $N_{\text{tracks}}^{\text{c}}$, the background is expected to drop steeply while most signal models rise steeply. This can be seen in Figure 4.18, which shows the distribution of data, the background expected by applying the ABCD-method bin by bin using the CRs defined below, and some benchmark signal models for events with $d_0^{\text{sig}}(\mu_1) < 3$. In order to capitalise on the difference in shape between the background and signal distributions, multiple SR bins are defined. The region

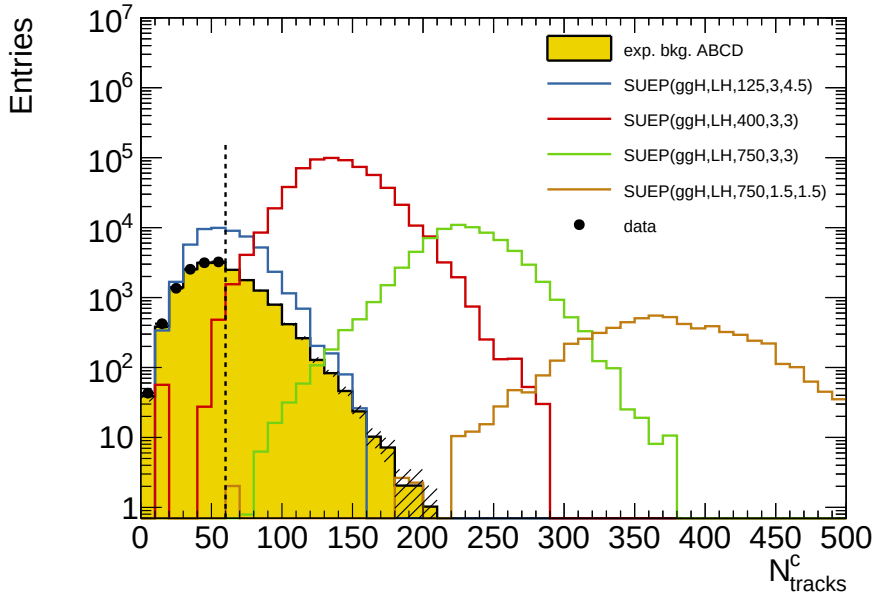

Figure 4.18: N^c_{tracks} distributions for events with $d_0^{sig}(\mu_1) < 3$ of data, some signal benchmark models and the expected background, calculated with $N_{bin}^{d_0^{sig}(\mu_1)<3} = \frac{N_B}{N_A} N_{bin}^{d_0^{sig}(\mu_1)>5}$.

definitions are schematically described in Figure 4.19(a). The region fulfilling $N^c_{tracks} \geq 60$ and $d_0^{sig}(\mu_1) < 3.0$, is used as SR and is split in eight bins. It is split evenly into seven bins of width $\Delta N^c_{tracks} = 20$ between $N^c_{tracks} = 60$ and $N^c_{tracks} = 200$ and the last bin requires $N^c_{tracks} \geq 200$. The regions with $N^c_{tracks} < 50$ or $d_0^{sig}(\mu_1) > 5$ are used as CRs and follow the binning of the SRs. The region with $50 \geq N^c_{tracks} < 55$ and $d_0^{sig}(\mu_1) < 3$, is used to evaluate the non-closure uncertainty. The SR is surrounded by VRs following the same binning. In every SR bin D_i, VR bin V_i and in the non-closure uncertainty region D_{nc}, the expected background can be calculated using Eqn. 3.8 and the appropriate CRs.

Additional VRs, CRs and a non-closure uncertainty region are defined using preselections requiring $N_\mu = 3$ or $N_\mu = 4$ instead of $N_\mu \geq 5$. Figure 4.19(b) schematically describes the regions for both the $N_\mu = 3$ and $N_\mu = 4$ selections. The same binning in N^c_{tracks} is used as for the preselection requiring $N_\mu \geq 5$.

4.13 Systematic uncertainties

Apart from the non-closure uncertainty, which affects the background estimate in the SR, all systematic uncertainties only affect the signal MC samples. They arise from uncertainties related to the reconstruction of muons and tracks, the trigger efficiency, the correction to the track multiplicity and the integrated luminosity. If a quantity is affected by an uncertainty, a variation is applied to the quantity such that the uncertainty is propagated downstream to the reconstruction algorithms, object selections, computation of observables and event selections successively. In the following, an uncertainty is considered to be negligible if the effect on the

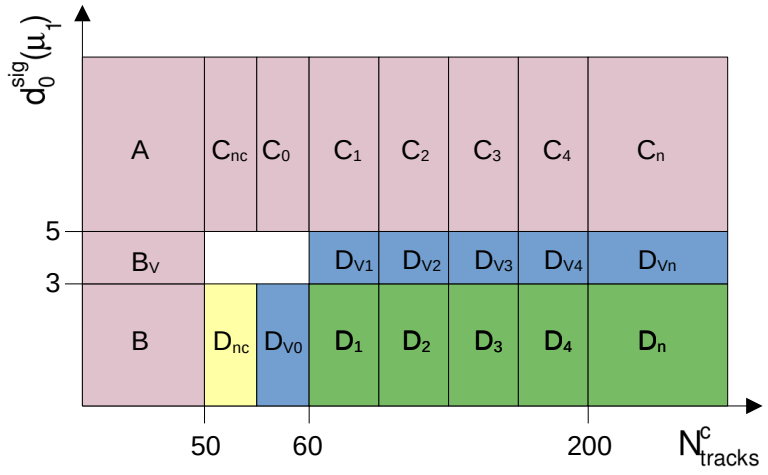

(a) Definition of regions in the $N_\mu \geq 5$ preselection. SRs in green, CRs in red, VRs in blue and the non-closure region in yellow.

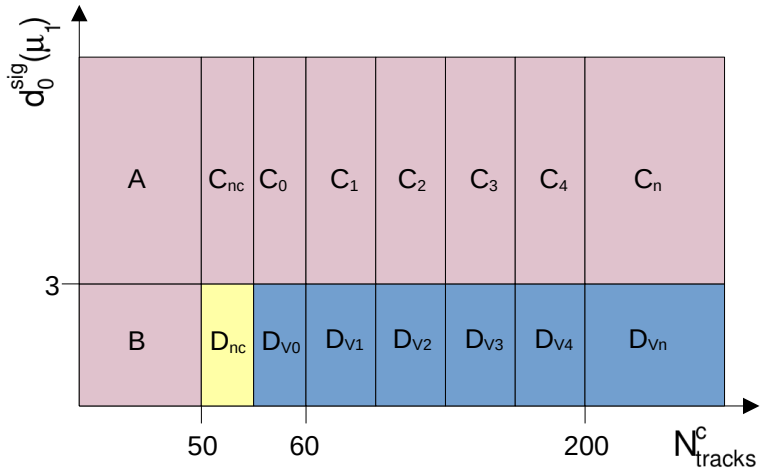

(b) Definition of regions in the $N_\mu = 3$ and $N_\mu = 4$ preselections. CRs in red, VRs in blue and the non-closure region in yellow.

Figure 4.19: Region definitions.

yield in the SR is less that 1% for all signal models. As described in Section 4.9, the two different selections used to measure of the correction term to the track multiplicity give slightly different results. But the difference, and the uncertainty on the fitted parameters are found to be negligible. The systematic uncertainties related to the ABCD-method are described in Section 4.11. The relative non-closure uncertainty in the SRs is 4.2%. The luminosity determination is described in Section 2.1 and is known to an average uncertainty of 1.7% [83]. In the following sections, systematic uncertainties related to track and muon reconstruction and trigger efficiency are described, followed by an overview of all systematic uncertainties.

4.13.1 Track reconstruction

The reconstruction efficiency is affected by the amount of passive material that lies within the ID. The amount of passive material of the ID as a whole is varied by 5%, the passive material of the IBL by 10% and that of the Patch Panel 0 (PP0) region, which is located between the outermost pixel layer and the innermost SCT layer and contains a high amount of passive material, is varied by 25%. The physics model used in the Geant4 simulation also affects the reconstruction efficiency and is varied. The number of fake tracks, i.e., the combinatorial background, was estimated by the ATLAS ID Working Group by observing the non-linear component in the evolution of track multiplicity with increasing number of simultaneous interactions. Any deviation from the linear behaviour is attributed to fake tracks. The number of fake tracks is evaluated for each MC event by assessing, using the truth-record of the event, whether the track was produced by a charged particle. A variation of 100% is applied to the number of fake tracks. The effect of uncertainties due to differences in resolution of the impact parameters between data and MC observed by the ATLAS ID Working Group and of the residual alignment uncertainty are found to be negligible.

4.13.2 Muon reconstruction

Variations are applied to muon track parameters based on the track-parameter resolution and the momentum scale uncertainty. Variations are also applied to the scale factors used to correct for the reconstruction efficiency, which come from statistical or systematic uncertainties affecting the efficiency measurement performed by the ATLAS Muon Working Group [107].

4.13.3 Trigger efficiency

The sources of systematic uncertainties arising from the correction of the trigger efficiency in MC arise from uncertainties in the tag-and-probe method that can be grouped in two categories: the statistical uncertainty, caused by the limited statistics available, and systematic uncertainties, caused by dependencies on the characteristics of the event, that can be different between the events selected to perform the tag-and-probe and the events selected in this analysis. The statistical uncertainties on the efficiencies of passing HLT_mu6 are evaluated for each period and each p_{T}, η and ϕ bin. Systematic uncertainties are evaluated by applying variations in the measurements of the efficiency in a similar way as is done in Ref. [128], except for the p_{T} requirement variation, that needs to be adapted to accommodate the p_{T} binning that is done in this search. The variations account for pile-up dependencies; the correlation in efficiency between tag and probe muons, which is due to the symmetry in ϕ present in both the ATLAS

Table 4.10: Scale factors obtained for individual systematic variations and the total systematic variation. The statistical uncertainty on the nominal value of the scale factor is shown in parentheses.

Systematic	Scale factor value	Diff. [%]
Nominal	0.846 (±0.45%)	-
Tag & probe correlation	0.849	0.36
Muon isolation	0.880	4.03
Background contribution	0.831	-1.72
Positively charged muons	0.838	-0.91
Negatively charged muons	0.853	0.89
No impact paramter requirements	0.830	-1.91
Low μ	0.852	0.73
High μ	0.836	-1.26
Low p_{T}	0.831	-1.77
High p_{T}	0.857	1.33
Total	0.893	5.63

Table 4.11: Total effect of systematic variations on HLT_mu6 scale factors for each detector-region and p_{T}-bin.

Region (p_{T}-bin)	Total systematic variation [%]
Barrel (6 GeV $< p_{\mathrm{T}} <$ 8 GeV)	5.6
Barrel (8 GeV $< p_{\mathrm{T}} <$ 10 GeV)	2.5
Barrel ($p_{\mathrm{T}} >$ 10 GeV)	1.1
End-cap (6 GeV $< p_{\mathrm{T}} <$ 8 GeV)	3.8
End-cap (8 GeV $< p_{\mathrm{T}} <$ 10 GeV)	0.9
End-cap ($p_{\mathrm{T}} >$ 10 GeV)	0.8

detector and the $Z \rightarrow \mu\mu$ decay; the background contribution; the dependence on the charge; the impact parameters; and the isolation of the muons. An uncertainty on the p_{T}-dependence of the selection is introduced by applying a variation requiring $p_{\mathrm{T}} < 7(9)$ GeV for muons in the $[6, 8]$ GeV ($[8, 10]$ GeV) bins and $p_{\mathrm{T}} < 20$ for muons in the $[10, \infty]$ GeV bins. In order to avoid that statistical fluctuations affect the evaluation of the systematic variations, they are evaluated inclusively in η, ϕ and periods of data-taking. The effect of the systematic variations on the HLT_mu6 scale factor is shown as an example in Table 4.10 for the barrel region and the $[6, 8]$ GeV p_{T}-bin. The statistical uncertainty on the nominal value of the scale factor is 0.45%, which does not dominate most systematic variations. The highest effect comes from the variation in isolation requirement. The total effect of all systematic variations are shown for each p_{T}-bin and detector-region in Table 4.11. The total relative effect on the muon scale factor is then applied as a single variation on the efficiencies in data and propagated to the computation of the HLT_3mu6 event-level scale factor.

Table 4.12: Effect of systematic uncertainties [%] on observables used in the analysis and on the yield in the signal region for the signal SUEP(ggH, LH, 125, 3, 3).

	N_μ	$\overline{p_T(\mu)}$	$d_0^{sig}(\mu_1)$	N_{tracks}^c	#events SR
Muon track parameter resolution	± 0.04	± 0.04	± 0.27	± 0.03	± 0.14
Muon momentum scale	± 0.01	± 0.08	± 0.19	± 0.04	± 0.31
Muon reco. eff. (stat.)	± 0.59	± 0.16	± 0.04	± 0.03	± 0.65
Muon reco. eff. (syst.)	± 1.86	± 0.36	± 0.03	± 0.16	± 2.05
Track reco. material (global)	± 0.04	± 0.14	± 0.31	± 0.38	± 1.53
Track reco. material (IBL)	± 0.02	± 0.02	± 0.33	± 0.07	± 0.45
Track reco. material (PP0)	± 0.04	± 0.04	± 0.14	± 0.09	± 0.69
Track reco. phys. model	± 0.01	± 0.02	± 0.02	± 0.11	± 0.37
Track reco. fake rate	± 0.19	± 0.07	± 0.57	± 0.94	± 2.34
Trigger (stat.)	± 0.79	± 0.51	± 0.32	± 0.16	± 6.76
Trigger (syst.)	± 0.80	± 0.46	± 0.09	± 0.16	± 5.81

4.13.4 Overview of systematic uncertainties

The effect of systematic uncertainties is summarised in Table 4.12 for one signal benchmark model. The dominant systematic uncertainties come from the trigger efficiency.

4.14 Unblinding strategy

An incremental unblinding strategy is especially useful for new searches which target wide ranges of signal models, like the one presented in this thesis. In each unblinding step, some of the signal models can be probed and the search can be adapted to the remaining signal models. Another advantage is that one of the unblinding steps might unveil a feature of the background that was not visible before. Such incremental unblinding strategies have been done previously in ATLAS, for example, in a search for strong gravity in multijet final states [136]. There are several ways in which data can be unblinded incrementally. One might unblind only part of the total integrated luminosity in each unblinding step, in which case, the unblinded data that is used to adapt the search for future unblinding steps cannot be used further. Another approach was explored in the context of this search. The strategy is to unblind parts of the phase-space step by step and converting SRs of previous unblinding steps into CRs and VRs for the next unblinding step if no discrepancy is observed.

The procedure is schematically described in Figure 4.20. At the beginning (1), a setup which is well suited for signal models with small N^{c}_{tracks} distributions is defined, i.e., a setup that uses low N^{c}_{tracks} requirements for the CR, non-closure region, VR, and SR bins. Moreover, an upper limit is set on the SR that is to be unblinded. After performing the first step of unblinding, if no discrepancy is observed in the signal region, the previous signal region, which is now unblinded, can be used to extend the CR and VR and a new SR, with a higher N^{c}_{tracks} bound, is defined (2). This step is repeated, twice in the example shown in Figure 4.20, for a total of three unblinding steps. For the last unblinding step (3), no upper-limit on the signal region is applied. If a significant excess is observed in one of the unblinding steps, then instead of performing the next unblinding step, the upper-bound on the SR is removed without altering the strategy in order to increase the sensitivity. Once the last unblinding step is performed, the upper-bounds of the signal regions of the first and second steps can be removed as well, in order to increase sensitivity for signals with lower N^{c}_{tracks} distributions (1b, 2b, 3b). An example of a concrete implementation and a simulation of the unblinding procedure in the presence of signal is given in Appendix A.

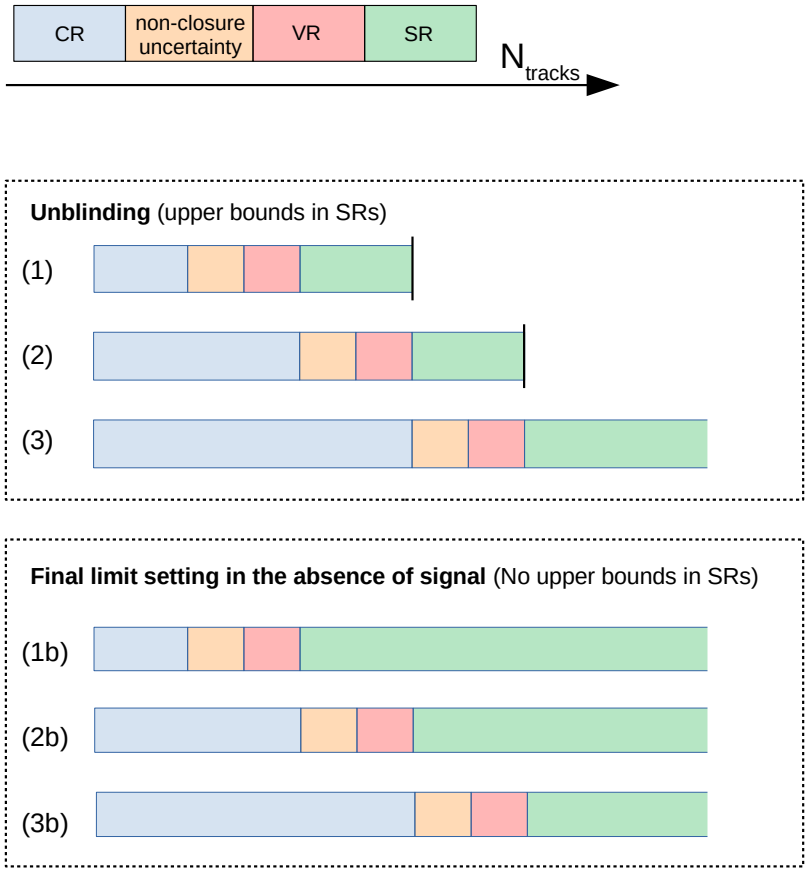

Figure 4.20: Schematic description of the incremental unblinding strategy.

Chapter 5

Results and Discussion

As will be shown in the next section, the background estimate in its present form could not be validated to the full extent within the ATLAS collaboration. Therefore, data is not yet unblinded and the final result of this search can not yet be shown. Nonetheless, expected exclusion limits are shown in Section 5.2.

5.1 Validation

The validation is performed assuming that no signal is in the observed data in the CRs and VRs. The expected yields in the VRs and their uncertainties can be computed using the standard ABCD-method described in Section 3.2 or with the likelihood-based method described in Section 3.2.1. Both methods give the same result.[†] For the preselection requiring $N_\mu \geq 5$, the yields in the CRs and the region D_{nc} are shown in Table 5.1,

Table 5.1: Observed number of events in CRs and non-closure uncertainty region D_{nc} for events passing $N_\mu \geq 5$

A	B	C_{nc}	D_{nc}	C_0	D_{V0}	B_{v}	C_1	C_2	C_3	C_4	C_5	C_6	C_7	C_8
7319	7503	1604	1713	1461	1518	1990	4159	2000	662	206	68	17	4	1

The number of expected events in the region $D_{\text{nc}} \cap D_{\text{V0}}$ is

$$N^{\text{exp}}_{D_{\text{nc}} \cap D_{\text{V0}}} = 3142 \pm 87 \ (\sigma_{\text{sys}} = 67, \ \sigma_{\text{stat}} = 56).$$

The number of observed events in the same region is $N^{\text{obs}}_{D_{\text{nc}} \cap D_{\text{V0}}} = 3231$, which is, accounting for the statistical uncertainty and the systematic uncertainty related to the ABCD-method, not within one standard deviation of the prediction. The non-closure uncertainty is therefore applied.

[†] Since the VRs are not used to constrain the background, the number of free parameters is equal to the number of observations in the likelihood-based method. In this case, the likelihood-based method is equivalent to the standard ABCD-method, because the fit is free to fulfil the relation $A/B = C/D$ exactly.

The relative non-closure uncertainty is

$$\sigma_{\text{nc}}^{r} = \frac{\left| N_{D_{\text{nc}}} - N_{D_{\text{nc}}}^{\text{exp}} \right|}{N_{D_{\text{nc}}}^{\text{exp}}} = 0.04.$$

A similar calculation is done for the regions defined in the $N_\mu = 3$ and $N_\mu = 4$ preselections. For $N_\mu = 3$ ($N_\mu = 4$), the relative non-closure uncertainty is $\sigma_{\text{nc}} = 4.3\%$ (0.5%). The background prediction in all VRs are compared to data in Table 5.2 and Figure 5.1.

Table 5.2: Expected and observed number of events in all VRs.

	ABCD expectation	observed events
D_{V0}	3140 ± 160	3231
D_{V1}	1130 ± 70	1125
D_{V2}	540 ± 40	479
D_{V3}	180 ± 17	183
D_{V4}	56 ± 9	60
D_{V5}	18 ± 5	12
D_{V6}	4.6 ± 2.4	4
D_{V7}	1.1 ± 1.2	0
D_{V8}	0.3 ± 0.6	1
$D_{V0}^{3\mu}$	483 000 ± 24 000	460 894
$D_{V1}^{3\mu}$	498 000 ± 24 000	483 130
$D_{V2}^{3\mu}$	151 000 ± 7000	152 260
$D_{V3}^{3\mu}$	37 200 ± 1800	38 957
$D_{V4}^{3\mu}$	8100 ± 400	8942
$D_{V5}^{3\mu}$	1600 ± 100	1794
$D_{V6}^{3\mu}$	315 ± 29	369
$D_{V7}^{3\mu}$	51 ± 10	69
$D_{V8}^{3\mu}$	13 ± 5	15
$D_{V0}^{4\mu}$	46 700 ± 400	46 173
$D_{V1}^{4\mu}$	54 800 ± 400	56 451
$D_{V2}^{4\mu}$	19 980 ± 220	21 502
$D_{V3}^{4\mu}$	5580 ± 100	6465
$D_{V4}^{4\mu}$	1380 ± 50	1750
$D_{V5}^{4\mu}$	300 ± 23	428
$D_{V6}^{4\mu}$	77 ± 12	66
$D_{V7}^{4\mu}$	11 ± 4	21
$D_{V8}^{4\mu}$	5.5 ± 3.1	5

As can be seen in Figure 5.1, deviations from the background prediction are compatible with statistical fluctuations in the VRs defined for the $N_\mu \geq 5$ preselection. For the $N_\mu = 3$ preselection, the background is slightly underestimated in the VRs $D_{V3}^{3\mu}$ to $D_{V7}^{3\mu}$, with the ratio of data over background increasing with increasing $N_{\text{tracks}}^{\text{c}}$, but data is only slightly outside the uncertainty

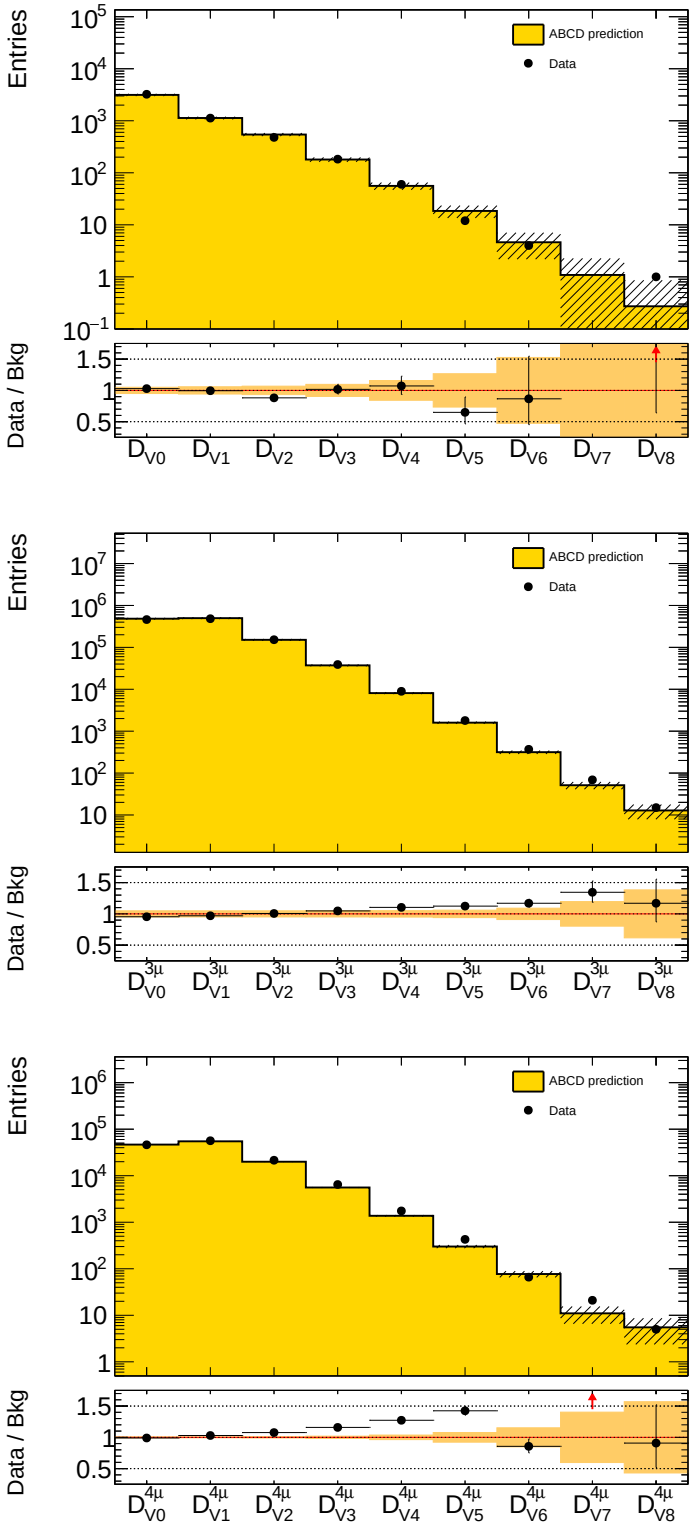

Figure 5.1: Data yields, background prediction and their ratio for all the VRs of the $N_\mu \geq 5$ (top), $N_\mu = 3$ (middle), and $N_\mu = 4$ (bottom) preselections.

bands of the estimate. For the $N_\mu = 4$ preselection, a similar trend in the data-over-background ratio can be seen, but the excesses in some regions are very significant. The highest discrepancy being 8.4 standard deviations in the region $D_{V3}^{4\mu}$. Such a deviation is very unlikely to occur by chance. Moreover, since a clear trend can be observed, we conclude that the background estimate is not valid for the VRs of the $N_\mu = 4$ preselection.

Possible explanations for these discrepancies have already been mentioned previously:

1) Different background flavours lead to different lifetimes and slightly different track multiplicities.

2) When the leading muon is displaced by more than the impact parameter requirements on tracks, the tracks stemming from the displaced decay are not counted in $N_{\text{tracks}}^{\text{c}}$.

If these caveats are at the origin of the discrepancy, the non-closure uncertainty is not sufficient to cover them. It is possible to roughly estimate the effect of points 1) and 2) by assuming that they correspond to a change in track multiplicity of the order of three tracks, which corresponds to the number of additional charged particles obtained in events containing a b-quark, compared to events containing only light-flavoured quarks [135]. The distribution of $N_{\text{tracks}}^{\text{c}}$ for data in the VR with the highest deviation from the expectation, $D_{V3}^{4\mu}$, is shown in Figure 5.2. A change of $N_{\text{tracks}}^{\text{c}}$ by three tracks leads to a migration from $V_3^{4\mu}$ to $V_2^{4\mu}$ of 1573 events and migration from $V_4^{4\mu}$ to $V_3^{4\mu}$ of 430 events. This means a net loss of 1133 events, which is of the order of the excess of 885 events seen in that bin, which makes both 1) and 2) plausible. However, it should be noted that the discrepancy is also compatible with signal models whose $N_{\text{tracks}}^{\text{c}}$ distribution peaks around $N_{\text{tracks}}^{\text{c}} = 100$. It could be either a signal model with low average N_μ or the lower tail in N_μ of a signal with higher average N_μ. More detailed studies are required in order to make sure that the effects cited above are indeed responsible for the deviations observed. If the flavour composition of the background was known, then 2) can be corrected for by adding to $N_{\text{tracks}}^{\text{c}}$ the number of tracks that are expected on average to be stemming from the displaced vertex, whenever the impact parameters of the leading muon are outside the track selection requirements. Reconstructing displaced vertices and counting associated tracks might be another possibility to estimate the number of missing tracks. It might also help to look at the invariant mass of muon pairs in order to see how much $J/\psi \to \mu\mu$ contributes.

Another possible explanation for the discrepancy is that for $N_\mu = 4$, the $t\bar{t}$ or $ZZ \to \mu\mu\mu\mu$ backgrounds, which contain prompt muons, contribute in the VRs of low $d_0^{\text{sig}}(\mu_1)$. But as shown in Table 4.9, according to the MC samples, these processes only contribute approximately 0.2% in the $N_\mu = 4$ preselection. Substracting these contributions from data before applying the ABCD-method was found to have a negligible effect.

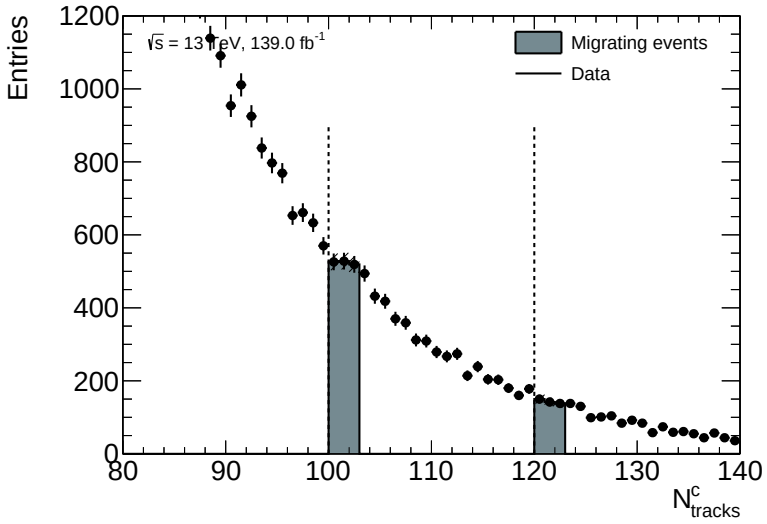

Figure 5.2: Data distribution of N^{c}_{tracks} for the preselection requiring $N_{\mu} = 4$ and for $d_0^{\text{sig}}(\mu_1) < 3$. The dotted lines indicate the position of the VR bin $D^{4\mu}_{V3}$ and the grey areas indicate events that are within $N^{c}_{\text{tracks}} = 3$ below the lower or upper limits of the bin.

5.2 Expected exclusion limits

Expected exclusion limits are obtained by computing CL_s, defined in Eqn. 3.7, but replacing the observed data in the SRs with the expected background under the H_b hypothesis. The background estimate is done using the likelihood-based ABCD-method and accounts for signal leakage in the CRs. HistFitter [137] is used to perform the statistical test. Figure 5.3 illustrates the two fits required to compute the negative log-likelihood ratio shown in Eqn. 3.4 using the signal model SUEP(ggH, LH, 400, 5, 5) as an example. Before the fit, the background yields are not defined, as the normalisation factors are not yet constrained. With a free floating signal strength, the maximum likelihood is obtained with a very small contribution of signal, as the ABCD-constraints of the background can otherwise not easily be fulfilled. With a fixed signal strength, the maximum likelihood is obtained with a slight adjustment of the shape and normalisation of the signal, obtained by pulls on the uncertainties affecting MC, and with a slight deviation from the ABCD constrains of the background, obtained with a pull on the non-closure uncertainty of the background. The total number of fitted events (signal + background) also slightly deviates from the observed number of events.

Table 5.3 shows the lowest cross-section expected to be excluded at 95% CL, together with $\pm 1\sigma$ variations and Figure 5.4 illustrates these results graphically. As expected, lower exclusion limits can be achieved for higher mediator masses, as the total amount of available energy allows for more particles of higher energy in the final state, which benefits the acceptance in the preselection and increases the separation to the background in $N^{\mathrm{c}}_{\mathrm{tracks}}$. There is no clear pattern between the sensitivity and the parameters m and T. Increasing either of them increases the average momentum of the final-state particles, which benefits the trigger acceptance, but on the other hand, decreases the final state particle multiplicity, which is detrimental for the separation to the background in $N^{\mathrm{c}}_{\mathrm{tracks}}$. For example, models with $M = 750$ GeV or $M = 400$ GeV and $m = 1.5$ GeV clearly benefit from an increased T, which increases trigger acceptance, whereas for $m = 5$ GeV, they clearly benefit from a reduced T, which increases $N^{\mathrm{c}}_{\mathrm{tracks}}$. Similar patterns that are seen for the lep-had signal models can be seen for the had and lep signal models. The sensitivity is lower for had models, by a factor of approximately two to ten compared to the lep-had signal models, depending on the signal model. For lep signal models, the sensitivity is increased by a factor of up to two compared to lep-had models.

Signal models with $M = 125$ GeV are expected to be excluded at 95% CL for production cross-sections $\mathcal{O}(100\,\mathrm{fb})$. This means that if the Higgs boson exhibits such an exotic decay mode, the search is sensitive for branching ratios above approximately 0.2%[†]. For $M = 400$ GeV ($M = 750$ GeV), cross-sections of $\mathcal{O}(1\,\mathrm{fb})$ ($\mathcal{O}(0.1\,\mathrm{fb})$) can be excluded at 95% CL. The limiting factor for most signal models is the acceptance of the HLT_3mu6 trigger, which for a lot of low-temperature signals requires the mediator to be boosted against ISR. The sensitivity could therefore be increased by accepting events passing HLT_4mu4 for the periods in which it is available. Another way to increase the sensitivity for signal models with high m and T is to do an additional binning in N_μ, since these models typically have low $N^{\mathrm{c}}_{\mathrm{tracks}}$ but high N_μ.

[†] Assuming the total Higgs-boson production cross-section to be 57 pb [28].

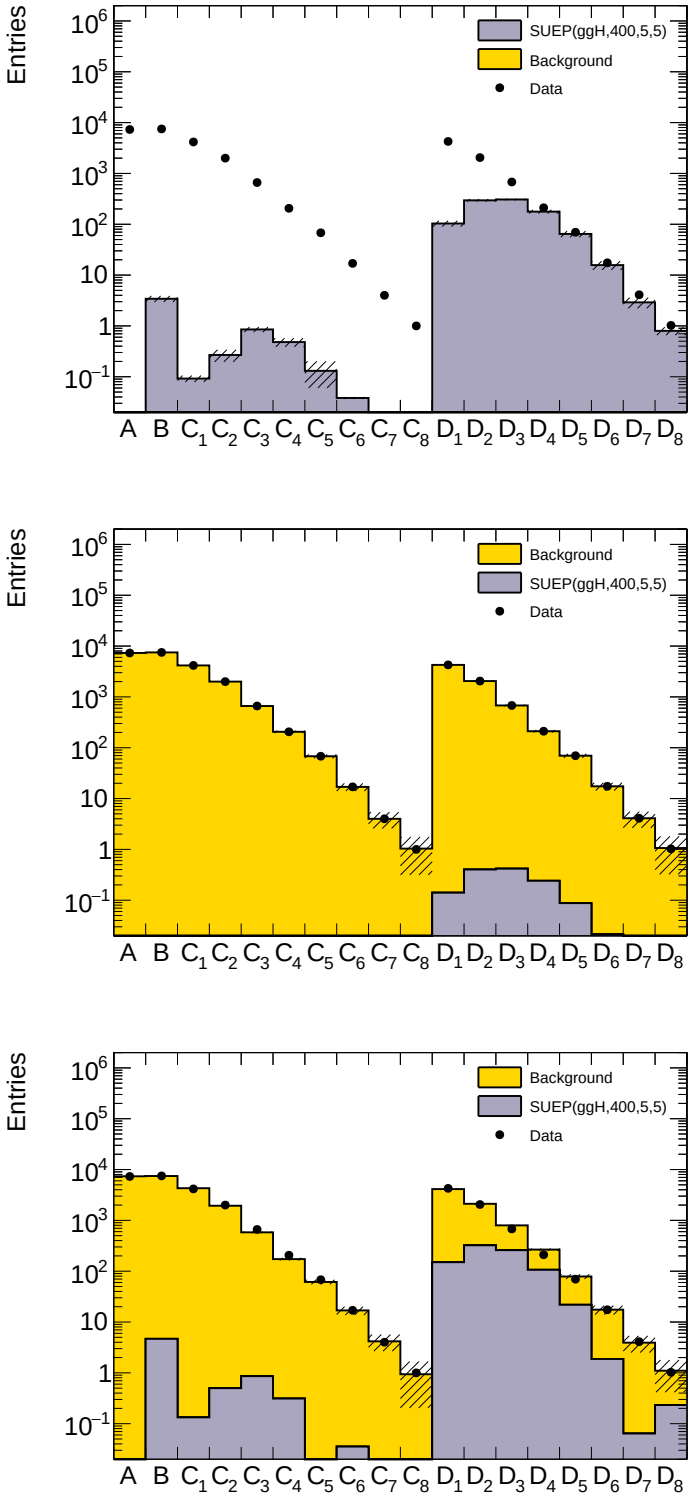

Figure 5.3: Background, SUEP(ggH, LH, 400, 5, 5) signal, and data yields before the fit (top), after the fit with free floating signal strength (middle), and after the fit with fixed signal strength (bottom). Data in the SRs is replaced by the expected background under the H_b hypothesis.

Table 5.3: Lowest excluded cross-sections expected at 95% CL (UL), together with $\pm 1\sigma$ variations.

Signal model	UL (fb)	UL-1σ (fb)	UL$+1\sigma$ (fb)
SUEP(ggH, LH, 125, 1.5, 1)	39.43	26.85	53.68
SUEP(ggH, LH, 125, 1.5, 1.5)	46.08	32.74	65.32
SUEP(ggH, LH, 125, 1.5, 2.25)	63.01	43.79	86.96
SUEP(ggH, LH, 125, 3, 2)	63.54	45.43	89.72
SUEP(ggH, LH, 125, 3, 3)	100.67	73.05	140.07
SUEP(ggH, LH, 125, 3, 4.5)	182.28	133.02	248.99
SUEP(ggH, LH, 125, 5, 3.33)	139.76	101.55	196.79
SUEP(ggH, LH, 125, 5, 5)	216.6	157.53	298.96
SUEP(ggH, LH, 125, 5, 7.5)	158.88	115.68	219.96
SUEP(ggH, LH, 400, 1.5, 1)	2.38	1.52	3.81
SUEP(ggH, LH, 400, 1.5, 1.5)	0.92	0.61	1.41
SUEP(ggH, LH, 400, 1.5, 2.25)	0.61	0.44	0.91
SUEP(ggH, LH, 400, 3, 2)	0.59	0.4	0.89
SUEP(ggH, LH, 400, 3, 3)	0.72	0.51	1.03
SUEP(ggH, LH, 400, 3, 4.5)	1.21	0.88	1.69
SUEP(ggH, LH, 400, 5, 3.33)	0.88	0.64	1.25
SUEP(ggH, LH, 400, 5, 5)	1.56	1.12	2.18
SUEP(ggH, LH, 400, 5, 7.5)	4.27	3.05	5.98
SUEP(ggH, LH, 750, 1.5, 1)	1.92	1.26	3.1
SUEP(ggH, LH, 750, 1.5, 1.5)	0.39	0.26	0.64
SUEP(ggH, LH, 750, 1.5, 2.25)	0.07	0.05	0.11
SUEP(ggH, LH, 750, 3, 2)	0.07	0.04	0.1
SUEP(ggH, LH, 750, 3, 3)	0.04	0.02	0.06
SUEP(ggH, LH, 750, 3, 4.5)	0.09	0.06	0.13
SUEP(ggH, LH, 750, 5, 3.33)	0.06	0.03	0.08
SUEP(ggH, LH, 750, 5, 7.5)	0.54	0.38	0.76
SUEP(ggH, H, 400, 1.5, 1)	14.66	9.71	23.71
SUEP(ggH, H, 400, 1.5, 1.5)	4.92	4.78	8.6
SUEP(ggH, H, 400, 1.5, 2.25)	2.43	1.61	3.86
SUEP(ggH, H, 400, 3, 2)	2.47	1.67	3.88
SUEP(ggH, H, 400, 3, 3)	3.02	2.13	4.42
SUEP(ggH, H, 400, 3, 4.5)	4.85	3.46	6.84
SUEP(ggH, H, 400, 5, 3.33)	3.94	2.81	5.61
SUEP(ggH, H, 400, 5, 5)	6.46	4.65	9.13
SUEP(ggH, H, 400, 5, 7.5)	17.36	12.8	24.04
SUEP(ggH, H, 750, 1.5, 1)	8.78	6.03	13.39
SUEP(ggH, H, 750, 1.5, 1.5)	3.28	3.21	5.46
SUEP(ggH, H, 750, 1.5, 2.25)	0.66	0.49	1.03
SUEP(ggH, H, 750, 3, 2)	0.33	0.32	0.6
SUEP(ggH, H, 750, 3, 3)	0.11	0.07	0.18
SUEP(ggH, H, 750, 3, 4.5)	0.15	0.1	0.23
SUEP(ggH, H, 750, 5, 3.33)	0.11	0.07	0.18
SUEP(ggH, H, 750, 5, 5)	0.25	0.18	0.37
SUEP(ggH, H, 750, 5, 7.5)	0.99	0.72	1.4
SUEP(ggH, L, 125, 1.5, 1)	32.35	22.89	47.3
SUEP(ggH, L, 125, 1.5, 1.5)	38.35	27.18	54.49
SUEP(ggH, L, 125, 1.5, 2.25)	58.22	41.7	82.54
SUEP(ggH, L, 125, 5, 3.33)	107.41	78.05	150.25
SUEP(ggH, L, 125, 5, 5)	135.28	100.13	187.11
SUEP(ggH, L, 125, 5, 7.5)	102.26	75.33	139.6

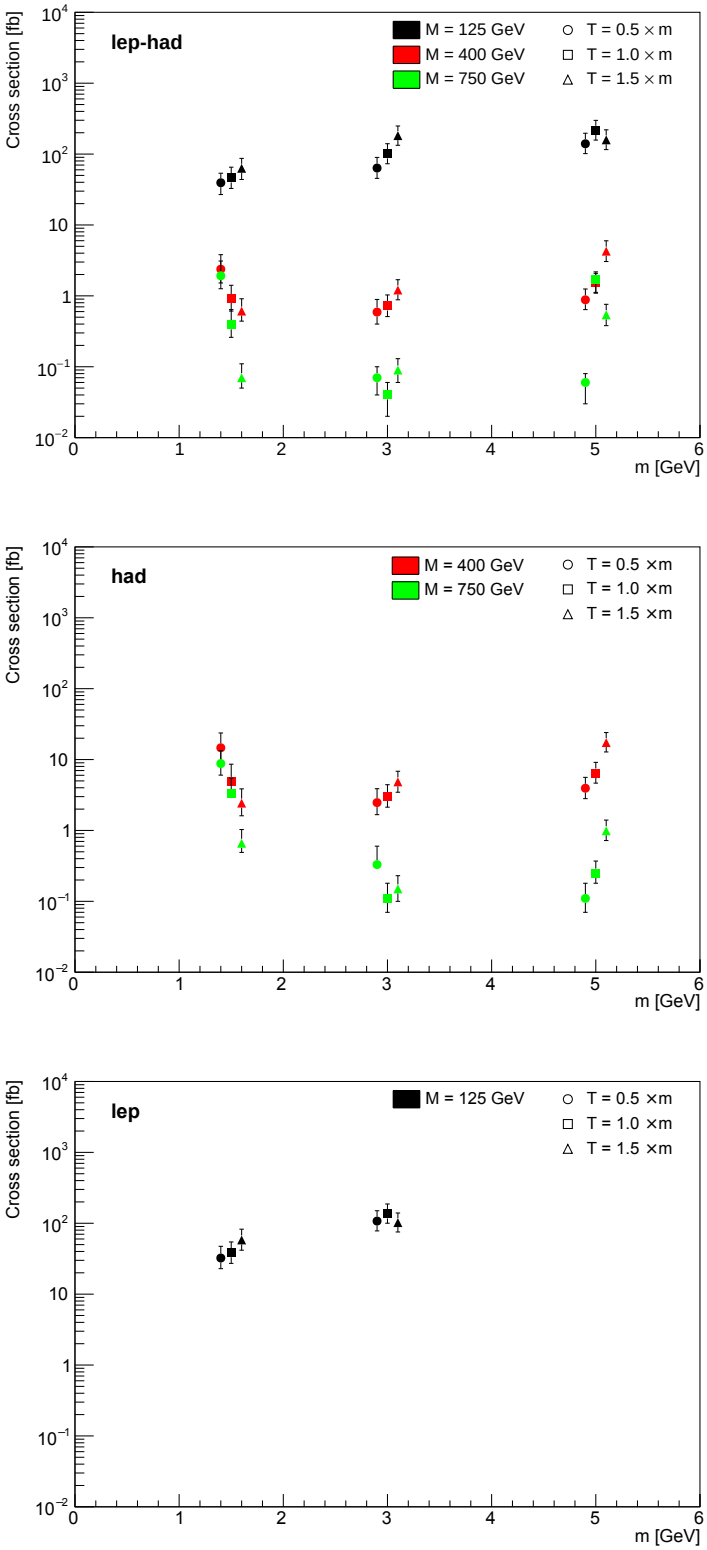

Figure 5.4: Lowest cross-section expected to be excluded at 95% CL for lep-had (top), had (middle) and lep (bottom) signal models. Signal models of different temperatures are shown slightly shifted horizontally to each other for a better visibility, but m is always either 1.5 GeV, 3 GeV or 5 GeV.

Chapter 6

Preliminary studies towards a cluster-based search strategy

As mentioned in Section 4.1, for SUEP signal models with very low temperatures or dark-pion masses, neither muon nor ID track reconstruction are efficient, but charged particles are still able to reach the IBL if their momenta are above approximately 10 MeV. As the final-state particle multiplicity is expected to be extremely high in this regime, a very high number of hits are expected in the IBL. The pixel-cluster multiplicity might therefore be used as a discriminating variable and form the basis of a search strategy.

In this section, preliminary studies on some elements of a pixel-cluster-based strategy are presented. Missing transverse energy triggers are discussed and their efficiencies are evaluated. Furthermore, selection requirements for pixel clusters are presented and the performance of the pixel-cluster multiplicity as a discriminating variable is compared to that of track multiplicity.

For these studies, an additional set of signal MC samples is used. These were produced outside of the official ATLAS simulation framework, but are simulated in the same way as described in Section 4.2. For all signal models, the production mechanism is gluon–gluon fusion and dark mesons decay with a branching ratio of 50% into electron or muon pairs, respectively. Furthermore, $T = m$ for all signal models. The parameters of the set of signal models considered are shown in Table 6.1.

Table 6.1: Signal model parameters used for cluster-based studies.

M (GeV)	$m = T$ (GeV)
125	0.1
125	0.25
125	1
400	0.1
400	0.25
400	1
750	0.1
750	0.25

6.1 Online event selection

At very low T or m, signal models are expected to have substantial missing transverse energy ($E_{\mathrm{T}}^{\mathrm{miss}}$), when the mediator recoils against ISR. This is expected for two reasons: First, charged particles of low momentum might never reach the calorimeters due to the strong magnetic field in the ID. Second, the energy deposits from a SUEP signal are, similar to pile-up noise, soft and unclustered. Since the algorithms used in $E_{\mathrm{T}}^{\mathrm{miss}}$ triggers typically suppress pile-up contributions, the energy deposits from SUEPs are not expected to contribute towards the transverse momentum balance either.

Several different algorithms [138] were used in $E_{\mathrm{T}}^{\mathrm{miss}}$ triggers during Run 2, including:

- The cell algorithm (xe) considers energy deposits in the calorimeters separately and computes the momentum for each cell assuming the deposit is caused by a massless particle. $E_{\mathrm{T}}^{\mathrm{miss}}$ is computed as the amplitude of the negative vector sum of the cell momenta. In order to be considered by the algorithm, the energy deposits need to be higher than twice the root-mean-square noise, which includes pile-up noise. The cell algorithm is mainly used at L1.
- The topo-cluster algorithm [139] builds topological clusters from the cell deposits by starting with a seed cell and adding neighbouring contributions if they are larger than twice the root-mean-square noise. Similarly to the cell algorithm, $E_{\mathrm{T}}^{\mathrm{miss}}$ is computed using the momenta obtained assuming massless particles.
- The pile-up fit algorithm (xe_pufit) divides the calorimeter system into 112 towers in which the energies of topo-clusters are added. If the energy deposit in a tower is below a threshold, its energy is assumed to be stemming from pile-up. A fit is then performed to estimate the pile-up contribution in each tower. The fit uses as constraint that the total $E_{\mathrm{T}}^{\mathrm{miss}}$ from all pile-up contributions has to be zero. The resulting pile-up contributions are then subtracted from towers in which the energy deposits are above the threshold. These towers are subsequently used to determine $E_{\mathrm{T}}^{\mathrm{miss}}$.
- The jet-based algorithm (xe_mht) computes the missing energy based on jets reconstructed using the anti-k_t algorithm [140].

The unprescaled triggers that are available change during each period of data-taking during Run 2. In the following, three $E_{\mathrm{T}}^{\mathrm{miss}}$ triggers are considered. Each of them was available and unprescaled during at least the majority of one year of data-taking. All use the cell algorithm at L1. The considered $E_{\mathrm{T}}^{\mathrm{miss}}$ triggers are:

- HLT_xe70_mht_L1XE50 (available in 2015), which uses the jet-based algorithm with a threshold of 70 GeV at HLT.
- HLT_xe110_mht_L1XE55 (available in 2016), which uses the jet-based algorithm with a threshold of 110 GeV at HLT.
- HLT_xe110_pufit_L1XE55 (available in 2017), which uses the pile-up fit algorithm with a threshold of 110 GeV at HLT.

Table 6.2: $E_{\mathrm{T}}^{\mathrm{miss}}$ trigger efficiencies [%] for various signal models. Statistical uncertainties are $\mathcal{O}(0.1\%)$.

M (GeV)	$m = T$ (GeV)	HLT_xe70_mht_L1XE50	HLT_xe110_mht_L1XE55	HLT_xe110_pufit_L1XE55	Total
125	0.1	16.2	11.6	10.2	16.2
125	0.25	8.2	2.2	1.8	8.2
125	1	2.4	0.8	0.5	2.4
400	0.1	24.7	21.1	19.5	24.7
400	0.25	23.1	16.2	15.2	23.2
400	1	4.3	1.1	1.1	4.4
750	0.1	27.5	24.3	22.7	27.5
750	0.25	28.4	21.8	21.0	28.4

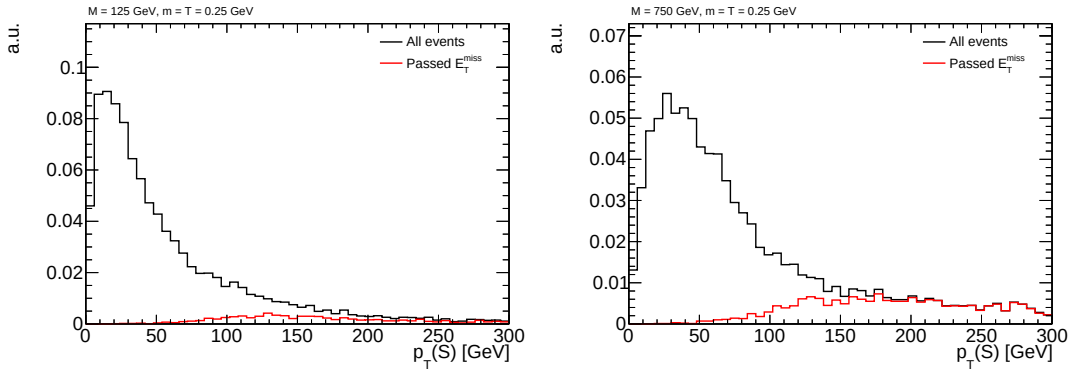

Figure 6.1: Transverse momentum of the mediator S for all events (black) and for events passing a $E_{\mathrm{T}}^{\mathrm{miss}}$ trigger (red) for signal models with $m = T = 0.25$ GeV and $M = 125$ GeV (left) and $M = 750$ GeV (right).

Table 6.2 shows the efficiencies obtained for the signal models considered in this section, together with the total efficiency obtained when requiring any of the triggers to have fired. The highest efficiencies are obtained with the jet-based algorithm of lower threshold that is only available in 2015. Unsurprisingly, slightly lower efficiencies are obtained for the higher threshold trigger. The trigger which uses the pile-up fit algorithm also gives slightly lower efficiencies. The highest efficiencies are obtained for lower values of m and T, for which the final state particles have lower p_{T}. Interestingly, a higher mediator mass yields a higher efficiency. This can – at least partly – be explained by the fact that more ISR is expected for higher mediator masses. Figure 6.1 shows the p_{T} of the mediator before and after requiring events to pass HLT_xe70_mht_L1XE50, for a signal model with $M = 125$ GeV and one with $M = 750$ GeV. It shows that a mediator with a higher mass has in general higher boost in the transverse plane. The figure also confirms that the mediator needs some transverse boost for the events to pass the $E_{\mathrm{T}}^{\mathrm{miss}}$ trigger.

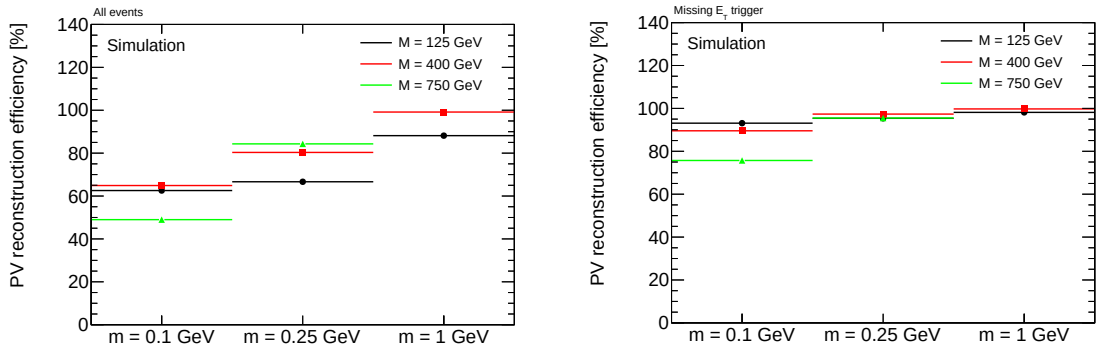

(a) All events.

(b) Events that passed a $E_{\mathrm{T}}^{\mathrm{miss}}$ trigger.

Figure 6.2: PV reconstruction efficiency for various signal models before and after the trigger selection.

6.2 Primary-vertex reconstruction and selection

How well can the PV be reconstructed and the SUEP production vertex be identified if track reconstruction is inefficient? In this study, the PV is reconstructed and selected in the same way as for the muon-based strategy: It is required to have at least two tracks associated to it and the PV is selected amongst all vertices as the one for which the sum of the squares of the p_{T} of the associated tracks is maximal. In order to assess how well it is selected, the truth information on the simulated collision is used to identify the true position of the SUEP interaction vertex. The PV is considered to be successfully selected if it is longitudinally within 1 mm of the true interaction vertex. Figure 6.2(a) shows the resulting efficiency for various signal models. For signal models with low m or T, the PV reconstruction is less efficient. However, it is much higher after the trigger selection, as shown in Figure 6.2(b). This is expected, as the additional ISR required to fire the trigger also leads to a higher number of successfully reconstructed tracks associated to the PV.

6.3 Pixel-cluster selection

Pile-up interactions also contribute to the pixel cluster multiplicity. When using ID tracks as discriminating variable, this contribution can be mitigated by requiring the impact parameters of the tracks to be compatible with the PV. There are no impact parameters for pixel clusters, but the contribution from pile-up can still be mitigated to some extent: If the location of the SUEP interaction vertex can be identified, at least the pixel clusters that are associated to tracks stemming from pile-up interactions can be rejected by requiring their impact parameters to be compatible with the PV. Individual pixel clusters can also be associated to a production vertex to the extent that the number of pixels that compose a cluster depends on the angle of incidence of the particle into the module. A particle traversing a pixel module perpendicularly typically interacts with only one pixel, whereas a particle that traverses the module with a flatter angle of incidence will traverse multiple pixels, as illustrated schematically in Figure 6.3. This feature has already been used in ATLAS to associate pixel clusters to the PV in the context of a luminosity measurement [141].

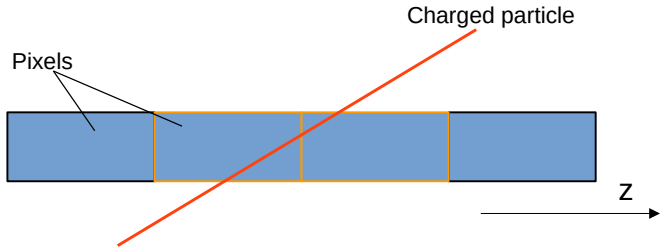

Figure 6.3: Schematic description of a charged particle traversing a pixel cluster module and producing a cluster of a longitudinal size of two pixel clusters.

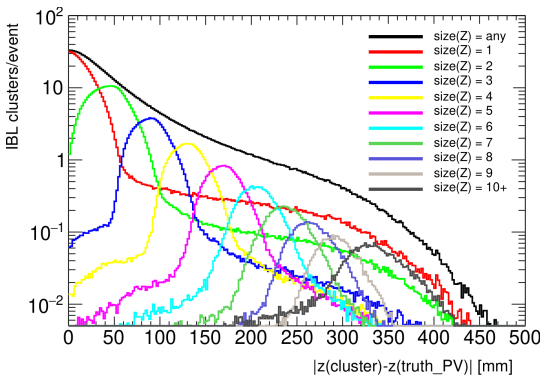

(a) Longitudinal separation between the primary production vertex and pixel clusters in the IBL that are caused by the passage of particle stemming from the production vertex for pixel clusters grouped by their size in the z-direction, measured in number of pixels.

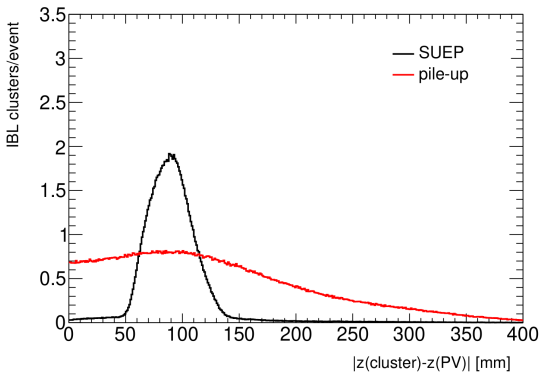

(b) Longitudinal separation between the primary production vertex and pixel clusters in the IBL of a size of 3 pixels in z-direction, caused by the passage of either particles produced at the primary production vertex or produced by a pile-up vertex.

Figure 6.4: Longitudinal pixel cluster distributions from SUEP simulations.

Figure 6.4(a) shows, using the truth information of a SUEP simulation, that for each longitudinal pixel cluster size, measured in number of pixels (size(z)), the pixel cluster multiplicity in the IBL peaks at a different longitudinal separation from the interaction vertex ($|z(\text{cluster}) - z(\text{PV})|$). Using clusters of size(z) = 3 as an example, Figure 6.4(b) shows that a large portion of the pixel clusters stemming from pile-up interactions can be removed with a requirement on the longitudinal separation between the production vertex and the position of the pixel cluster. Therefore, for each size(z), a window of acceptance in $|z(\text{cluster}) - z(\text{PV})|$ was defined. The windows of acceptance were chosen to be the full width at half maximum of the distributions plotted in Figure 6.4(a) and are given in Table 6.3. The contributions from pixel clusters with size(z) $\geq$ 10 are grouped together. Pixel clusters are rejected if they touch the edge of a module longitudinally, since in that case, pixel clusters might be shorter than what they would have been, if additional pixels were available on the path of the charged particle.

Figure 6.5 shows a cutflow of the requirements mentioned above for IBL pixel clusters that are caused by the passage of a decay product of the SUEP and for all other pixel clusters, which includes pile-up, secondary radiation and ISR.

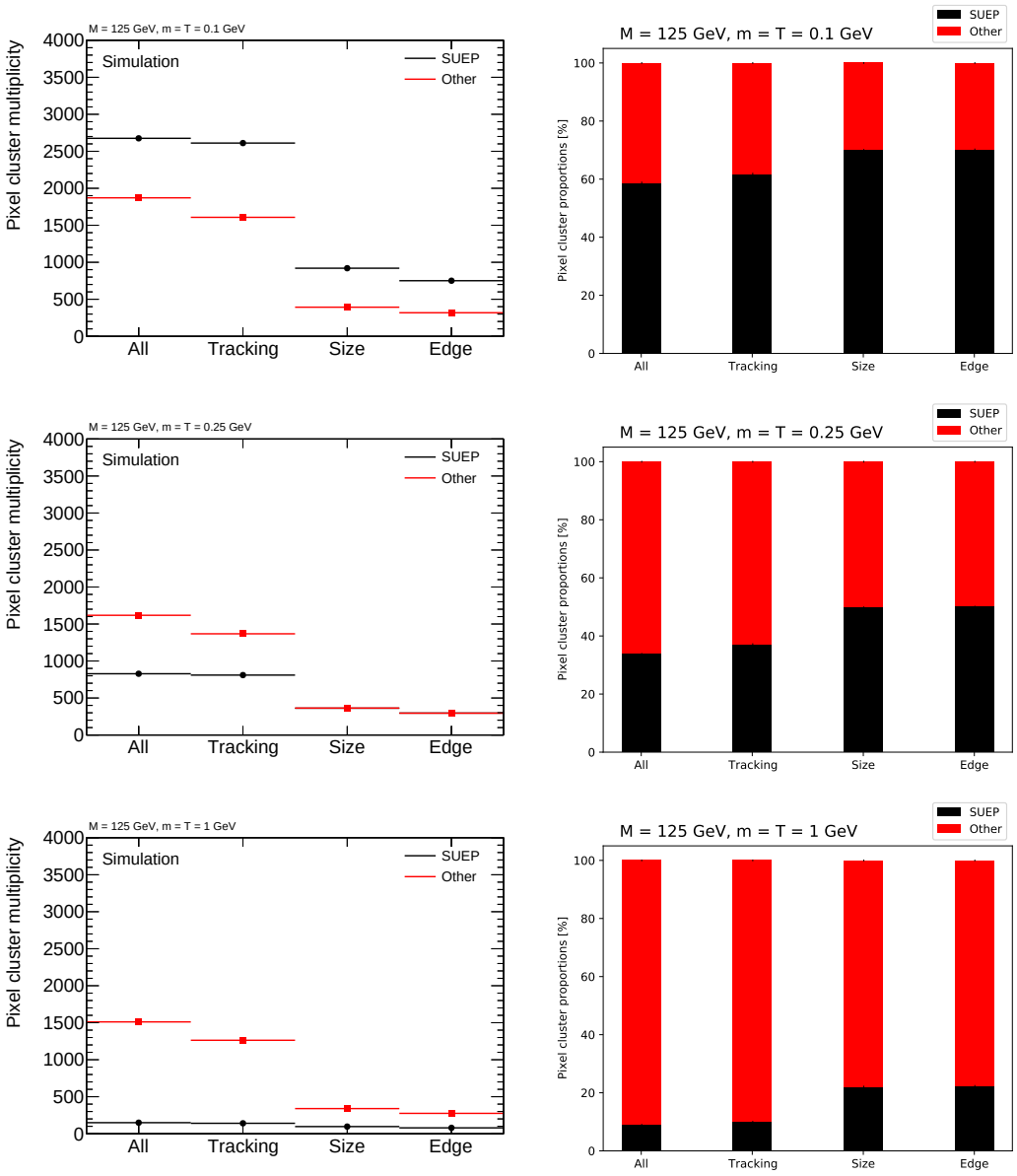

Figure 6.5: Cutflow of the pixel cluster selection for pixel clusters that are caused by a SUEP decay product and other clusters. The first cut (Tracking) rejects pixel clusters which are part of an ID track whose impact parameters are not compatible with the PV. The track reconstruction and selection used for this is the same as the one used in the muon-based strategy and is described in Section 4.5. The second cut (Size) rejects pixel clusters if $|z(\text{cluster}) - z(\text{PV})|$ is not within the acceptance for the size(z) of the cluster defined in Table 6.3. The last cut (Edge) rejects pixel clusters that are on the edge of a module. The total number of selected clusters are shown on the left and the relative contributions are shown on the right. All distributions are for $M = 125$ GeV. $m = T = 0.1$ GeV is shown at the top, $m = T = 0.25$ GeV in the middle, and $m = T = 1$ GeV at the bottom.

Table 6.3: Windows of acceptance for the pixel cluster selection.

size(z)	$\lvert z(\text{cluster}) - z(\text{PV})\rvert_{\text{min}}$	$\lvert z(\text{cluster}) - z(\text{PV})\rvert_{\text{max}}$
1	0.0	23.7
2	13.2	67.8
3	63.8	110.3
4	105.9	151.6
5	144.8	191.3
6	169.4	227.7
7	211.1	260.9
8	236.6	288.4
9	267.4	313.1
10+	299.8	363.3

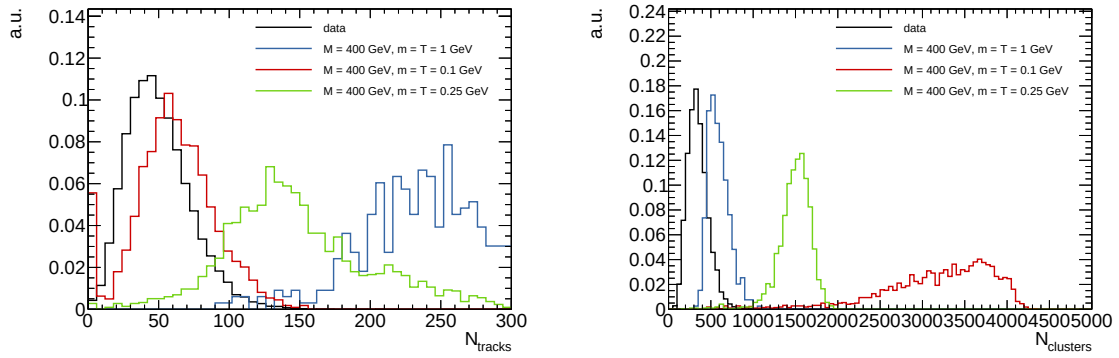

(a) Track multiplicity.

(b) Pixel cluster multiplicity.

Figure 6.6: Track and cluster multiplicity for SUEP signal models with $M = 400$ GeV passing an $E_{\text{T}}^{\text{miss}}$ trigger and 11 067 events of data recorded in 2016 passing any trigger.

6.4 Performance of the pixel cluster observable

In order to assess the performance of the pixel-cluster multiplicity as a discriminating variable, it is compared to the performance of the track multiplicity. As this analysis needs to be done in a special data format that contains pixel-cluster information, the number of readily available datasets is scarce. For this reason, no background MC samples were used here. A rough, qualitative estimate is done by using 11 067 events from 2016 data, which are selected by any of the triggers online during that time, and for which $\mu = 20$. This sample is composed of various processes that are most likely not representative of the background that could play a role in a cluster-based analysis. Nevertheless, it can be used as a substitute to a more realistic background dataset. As can be seen in Figure 6.6, which shows the pixel and track multiplicity for signal models with $M = 400$ GeV, the pixel cluster multiplicity is very well separated from data for $m = T = 0.1$ GeV, whereas for the same model parameters, the signal distribution of track multiplicity is barely separated from data. The opposite can be said for $m = T = 1$ GeV. For $m = T = 0.25$ GeV, pixel cluster multiplicity performs slightly better than track multiplicity. Similar observations can be made for other mediator masses that are not shown here.

6.5 Discussion and outlook

SUEP simulations suggest that $E_{\mathrm{T}}^{\mathrm{miss}}$ triggers can be used to select events for $m = T \lessapprox 0.5$ GeV with efficiencies of the order of 10%. Further studies are required to understand exactly how the $E_{\mathrm{T}}^{\mathrm{miss}}$ is formed. Simulations might show what portion of the final state is trapped in the magnetic field, how much and in what form it reaches the calorimeters. It would be interesting to see if the unclustered nature of SUEPs helps the trigger efficiency. The trigger efficiency might be better understood by a detailed comparison of the response of the algorithms to pile-up simulation and minimum-bias data. If it is clear that a substantial part of the decay products of SUEPs do not reach the calorimeters, then the efficiency of the triggers should be very similar to that observed in $Z \rightarrow \mu\mu$ events for the same amount of ISR radiation. Reconstructing ISR jets might be very useful for this reason.

A selection of pixel clusters has been presented, which increases the purity of pixel clusters induced by signal. With that selection, the pixel cluster multiplicity seems to outperform the track multiplicity as a discriminating variable for $m = T \lessapprox 0.25$ GeV. Certainly, the selection can be further optimised. It is possible that a more sophisticated observable can be built from the pixel cluster distribution in the IBL. For example, instead of just rejecting pixel clusters that are not compatible with the PV, they might be used to estimate how much pile-up contributes to the multiplicity of clusters that pass the selection. This could be achieved in a similar way as is done in the calorimeters by the xe_pufit algorithm.

The main open question which has not been addressed so far is the background composition and how it can be estimated. After the online selection, processes that can contain neutrinos in the final state are expected to contribute. Simulation might be used to get a better idea of the background composition. In order to estimate the background, it is possible that an additional observable that is uncorrelated to the pixel cluster multiplicity can be found. This could be a property of the ISR jet that has been reconstructed.

The data formats meant to be used for physics analyses do not store information about pixel clusters, as this would increase the size of the format significantly. Therefore, the selection of pixel clusters and the computation of event-level observables based on pixel clusters needs to be done at an early stage of data processing, when all detector information is still available. An algorithm that computes these variables has already been prepared.

A dedicated trigger can be developed for future runs of data-taking. A conceivable trigger was presented in Ref. [18]. It would select events based on the presence of a 'belt of fire' in the IBL, i.e. an accumulation of pixel clusters localised longitudinally. Such a trigger is expected to be more efficient than $E_{\mathrm{T}}^{\mathrm{miss}}$ triggers. However, an analysis with Run-2 data would be very useful in order to get first results. In this way, future searches can be more tailored towards signal models that have not been probed yet.

Conclusion

In this thesis, a novel search for new physics was presented. The analysed signatures, SUEPs, are characteristic of strongly-coupled, quasi-conformal HV models and are inspired by the dynamics of low-energy QCD.

The search uses 139 fb^{-1} of pp collisions at 13 TeV recorded by the ATLAS detector, and targets signal models with dark-meson masses and temperatures between 1.5 and 5 GeV, where the dark mesons decay promptly and the final states contain muons. A multi-muon trigger and a new muon reconstruction algorithm optimised to be efficient at low momentum were used. The event selection capitalises on the high multiplicity of muons, their low p_{T}, and the high multiplicity of tracks that are expected in the SUEPs. In order to estimate the dominant heavy-flavour multijet background, a standard method of particle physics, the ABCD-method, was used. The method can be applied under the assumption that the displacement of the leading muon is uncorrelated with the track multiplicity in the event. To first approximation, this was shown to be the case. A non-closure uncertainty was added in order to catch potential small correlations that were expected. Large deviations between the background estimate and data are observed in some validation regions. These deviations suggest that the non-closure uncertainty is not sufficient to cover some of the correlations, but the observed excess is also compatible with the tail of a signal distribution. Further studies are required in order to fully understand the background. Some suggestions were given.

If the particle mediating the access to the HV is the Higgs boson, then signal models are expected to be excluded at 95% CL for production cross-sections $\mathcal{O}(100\text{ fb})$, corresponding to a branching-ratio of 0.2%. If the mediator is a new scalar particle with $M = 400$ GeV ($M = 750$ GeV), cross-sections of $\mathcal{O}(1\text{ fb})$ ($\mathcal{O}(0.1\text{ fb})$) are expected to be excluded at 95% CL. The sensitivity further depends on the fraction of muons composing the final state and on the momenta and multiplicity of the final state particles.

In this thesis, it was also shown that a pixel-cluster-based search strategy, which targets SUEPs with final state particles of very low momenta, is a promising approach. The studies shown suggest efficiencies of the order of 10% can be obtained from $E_{\text{T}}^{\text{miss}}$ triggers that were available in Run 2, and that the pixel-cluster multiplicity outperforms track multiplicity as a discriminating variable for $T \lessapprox 0.25$ GeV.

Appendix A

Simulating the unblinding procedure through signal injection

In order to illustrate the functionality of the unblinding procedure in the presence of signal, the unblinding procedure is simulated through the use of signal injection. The region definitions used for the three unblinding steps are given in Table A.1 and illustrated in Figure A.1. The resulting background estimate for the first unblinding step is given in Table A.2 In order to simulate the unblinding procedure in the presence of a signal, the observed data yields in B, D^{cl}, D^{val} and D of any unblinding step are replaced by the sum of the expected signal and background yields in these regions, using the already unblinded regions A and B of the first step to calculate the background expectation. For example, we replace the observed yield in the region D of the second step, $N_{D_2}^{\text{obs}}$, by

$$N_{D_2}^{\text{obs}} = \frac{N_{B_1}}{N_{A_1}} N_{C_2} + N_{D_2}^{\text{obs,signal}}.$$

Once these fake observed yields are calculated, the actual expected yields in $D^{(\text{cl,val})}$ for each step are calculated using the fake observed yield in B and the actual observed yields in region A and $C^{(\text{cl,val})}$.

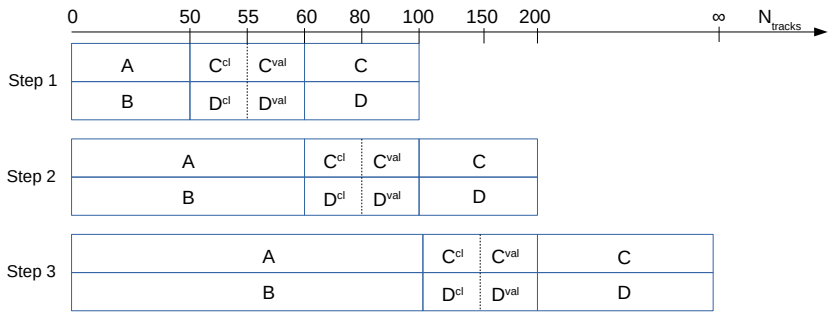

Figure A.1: ABCD regions for each unblinding step

Table A.1: Definition of regions in the ABCD plane for each unblinding step.

	Step 1		Step 2		Step 3	
	$N^{\mathrm{c}}_{\mathrm{tracks}}$	$d_0^{\mathrm{sig}}(\mu_1)$	$N^{\mathrm{c}}_{\mathrm{tracks}}$	$d_0^{\mathrm{sig}}(\mu_1)$	$N^{\mathrm{c}}_{\mathrm{tracks}}$	$d_0^{\mathrm{sig}}(\mu_1)$
A	$[0, 50]$	> 3.5	$[0, 60]$	> 3.5	$[0, 100]$	> 3.5
C^{cl}	$[50, 55]$	> 3.5	$[60, 80]$	> 3.5	$[100, 150]$	> 3.5
C^{val}	$[55, 60]$	> 3.5	$[80, 100]$	> 3.5	$[150, 200]$	> 3.5
C	$[60, 100]$	> 3.5	$[100, 200]$	> 3.5	> 200	> 3.5
B	$[0, 50]$	< 3.0	$[0, 60]$	< 3.0	$[0, 100]$	< 3.0
D^{cl}	$[50, 55]$	< 3.0	$[60, 80]$	< 3.0	$[100, 150]$	< 3.0
D^{val}	$[55, 60]$	< 3.0	$[80, 100]$	< 3.0	$[150, 200]$	< 3.0
D	$[60, 100]$	< 3.0	$[100, 200]$	< 3.0	> 200	< 3.0

Table A.2: Result of the background estimate for unblinding Step 1.

N_A	8701.0
N_B	7503.0
$N_{C^{val}}$	3238.0
$N^{exp}_{D^{val}}$	2792.17 ± 65.9 (sys) ± 52.84 (stat)
$N^{obs}_{D^{val}}$	2885.0
closure?	no
$N_{C^{cl}}$	1506.0
$N^{exp}_{D^{cl}}$	1298.65
$N^{obs}_{D^{cl}}$	1367.0
$N_{C^{val'}}$	1403.0
$N^{exp}_{D^{val'}}$	1209.83 ± 37.5 (sys) ± 34.78 (stat) ± 63.68 (cl)
$N^{obs}_{D^{val'}}$	1202.0
N_C	6917.0
N^{exp}_D	5964.63 ± 118.21 (sys) ± 77.23 (stat) ± 313.95 (cl)
N^{obs}_D	blinded

Tables A.3 and A.4 show the results of the study for two benchmark signals and Table A.5 summarises the results for all lep-had benchmark signal models, by showing the number of standard deviations that are observed in SRs and VRs for each unblinding step. Apart from some signal models with very low $N^{\mathrm{c}}_{\mathrm{tracks}}$ multiplicities, there is always one unblinding setup that provides a high sensitivity in the signal region and a good agreement in the validation region. If there is a large excess in a VR of one unblinding step, then there would have been a large excess in the SR of the previous unblinding step.

Table A.3: Results of the unblinding simulation when injecting the signal SUEP(ggH,LH,400,1.5,1.5)

step	1	2	3
N_A	8701.0	12335.0	19615.0
N_B	7503.0	10636.65	16914.3
$N_{C^{val}}$	3238.0	6917.0	1064.0
$N^{exp}_{D^{val}}$	2792.17 ± 65.9 (sys) ± 52.84 (stat)	5964.63 ± 106.64 (sys) ± 77.23 (stat)	917.5 ± 29.73 (sys) ± 30.29 (stat)
$N^{obs}_{D^{val}}$	2792.17	5964.63	9524.52
closure?	yes	yes	no
$N_{C^{cl}}$	–	–	1015.0
$N^{exp}_{D^{cl}}$	–	–	875.25
$N^{obs}_{D^{cl}}$	–	–	1519.31
$N_{C^{val'}}$	–	–	47.0
$N^{exp}_{D^{val'}}$	–	–	40.53 ± 5.93 (sys) ± 6.37 (stat) ± 29.82 (cl)
$N^{obs}_{D^{val'}}$	–	–	8003.49
N_C	6917.0	1064.0	2.0
N^{exp}_D	5964.63 ± 118.21 (sys) ± 77.23 (stat)	917.5 ± 30.64 (sys) ± 30.29 (stat)	1.72 ± 1.22 (sys) ± 1.31 (stat) ± 1.27 (cl)
N^{obs}_D	5964.63	9524.52	42911.04

Table A.4: Results of the unblinding simulation when injecting the signal SUEP(ggH,LH,750,1.5,1.5)

step	1	2	3
N_A	8701.0	12335.0	19615.0
N_B	7503.0	10636.65	16916.32
$N_{C^{val}}$	3238.0	6917.0	1064.0
$N^{exp}_{D^{val}}$	2792.17 ± 65.9 (sys) ± 52.84 (stat)	5964.63 ± 106.64 (sys) ± 77.23 (stat)	917.61 ± 29.73 (sys) ± 30.29 (stat)
$N^{obs}_{D^{val}}$	2792.17	5966.65	922.4
closure?	yes	yes	yes
$N_{C^{cl}}$	–	–	–
$N^{exp}_{D^{cl}}$	–	–	–
$N^{obs}_{D^{cl}}$	–	–	–
$N_{C^{val'}}$	–	–	–
$N^{exp}_{D^{val'}}$	–	–	–
$N^{obs}_{D^{val'}}$	–	–	–
N_C	6917.0	1064.0	2.0
N^{exp}_D	5964.63 ± 118.21 (sys) ± 77.23 (stat)	917.5 ± 30.64 (sys) ± 30.29 (stat)	1.72 ± 1.22 (sys) ± 1.31 (stat)
N^{obs}_D	5966.65	922.4	6218.42

Table A.5: Expected Z-scores in the presence of signal in the validation and signal regions for the three unblinding steps. The validation region refers to the full validation region when a non-closure uncertainty is not needed and to the *upper* half of the validation region otherwise. The signal region used to determine the Z-scores are without upper-limits.

signal	VR1	SR1	VR2	SR2	VR3	SR3
SUEP(ggH,LH,125,1.5,1)	0	36.81	4.14	118.53	12.58	21.34
SUEP(ggH,LH,125,1.5,1.5)	0.61	71.38	7.35	41.98	2.62	0.79
SUEP(ggH,LH,125,1.5,2.25)	1.81	13.98	2.45	6.46	1.04	-0.11
SUEP(ggH,LH,125,3,2)	2.01	12.55	2.69	5.09	0.59	-0.14
SUEP(ggH,LH,125,3,3)	1.25	3.51	1.88	1.62	0.01	-0.56
SUEP(ggH,LH,125,3,4.5)	1.98	2.42	0.81	-0.2	-2.55	-0.92
SUEP(ggH,LH,125,5,3.33)	2.09	3.34	1.07	1.08	0.19	-0.78
SUEP(ggH,LH,125,5,5)	1.72	0.22	-0.68	-5.16	-0.66	-0.9
SUEP(ggH,LH,125,5,7.5)	-0.7	-2.88	-2.21	-3.49	-1.14	-0.77
SUEP(ggH,LH,400,1.5,1)	0	97.49	0	356.83	11.85	8528.81
SUEP(ggH,LH,400,1.5,1.5)	0	328.34	0	1201.76	256.32	19539.2
SUEP(ggH,LH,400,1.5,2.25)	0	1371.54	10.55	3620.48	65.01	623.21
SUEP(ggH,LH,400,3,2)	0	1526.11	8.63	2668.25	54.82	427.15
SUEP(ggH,LH,400,3,3)	2.08	1334.15	10.67	486.36	10.61	16.91
SUEP(ggH,LH,400,3,4.5)	1.75	121.78	9.04	59.85	2.43	1.08
SUEP(ggH,LH,400,5,3.33)	2.85	525.87	11.68	206.62	5.36	4.72
SUEP(ggH,LH,400,5,5)	3.68	143.22	6.19	24.28	1.58	0.75
SUEP(ggH,LH,400,5,7.5)	1.85	11.52	2.65	4.53	0.54	0.15
SUEP(ggH,LH,750,1.5,1)	0	8.11	0.03	29.61	-0	712.34
SUEP(ggH,LH,750,1.5,1.5)	0	39.43	0.02	144.27	0.11	3468.37
SUEP(ggH,LH,750,1.5,2.25)	-0.02	218.16	-0	798.65	40.72	18993.2
SUEP(ggH,LH,750,3,2)	-0.05	238.62	-0.05	873.93	59.29	20667.9
SUEP(ggH,LH,750,3,3)	0	474.7	0.18	1736.82	291.18	27871.5
SUEP(ggH,LH,750,3,4.5)	-0	533.32	3.3	1914.43	162.29	1537.44
SUEP(ggH,LH,750,5,3.33)	0	517.17	0.63	1890.91	387.01	12753.9
SUEP(ggH,LH,750,5,7.5)	0.42	436.98	16.58	616.26	7.71	5.57

Appendix B

Monte Carlo Datasets

Table B.1 and B.2 show the dataset identifiers (DSIDs) and names of the used background and signal samples, respectively.

Table B.1: Background MC sample names and identifiers

process	DSID	sample name
$t\bar{t}$	410470	PhPy8EG_A14_ttbar_hdamp258p75_nonallhad
$t\bar{t} + Z$	410219	aMcAtNloPythia8EvtGen_MEN30NLO_A14N23LO_ttmumu
$Z \rightarrow \mu\mu$	361107	PowhegPythia8EvtGen_AZNLOCTEQ6L1_Zmumu
$ZZ \rightarrow \mu\mu\mu\mu$	364250	Sherpa_222_NNPDF30NNLO_llll
WWZ	346904	aMcAtNloPy8EG_NNPDF30NLO_WWZ_4l2v
	427000	Pythia8EvtGen_A14NNPDF23LO_jetjet_JZ0W_mufilter
	427030	Pythia8EvtGen_A14NNPDF23LO_jetjet_JZ1WA_mufilter
	427031	Pythia8EvtGen_A14NNPDF23LO_jetjet_JZRW1B_mufilter
QCD multijet	427032	Pythia8EvtGen_A14NNPDF23LO_jetjet_JZRW2_mufilter
	427033	Pythia8EvtGen_A14NNPDF23LO_jetjet_JZRW3_mufilter
	427034	Pythia8EvtGen_A14NNPDF23LO_jetjet_JZRW4_mufilter
	427005	Pythia8EvtGen_A14NNPDF23LO_jetjet_JZ5W_mufilter

Table B.2: Signal MC sample names and identifiers

process	DSID	sample name	Simulated events
SUEP(ggH,LH,125,1.5,1)	800456	Py8_HtoSUEP_ggH_lephad_125_1p50_1p00	40 000
SUEP(ggH,LH,125,1.5,1.5)	800457	Py8_HtoSUEP_ggH_lephad_125_1p50_1p50	40 000
SUEP(ggH,LH,125,1.5,2.25)	800458	Py8_HtoSUEP_ggH_lephad_125_1p50_2p25	40 000
SUEP(ggH,LH,125,3,2)	800459	Py8_HtoSUEP_ggH_lephad_125_3p00_2p00	20 000
SUEP(ggH,LH,125,3,3)	800460	Py8_HtoSUEP_ggH_lephad_125_3p00_3p00	20 000
SUEP(ggH,LH,125,3,4.5)	800461	Py8_HtoSUEP_ggH_lephad_125_3p00_4p50	20 000
SUEP(ggH,LH,125,5,3.33)	800462	Py8_HtoSUEP_ggH_lephad_125_5p00_3p33	10 000
SUEP(ggH,LH,125,5,5)	800463	Py8_HtoSUEP_ggH_lephad_125_5p00_5p00	10 000
SUEP(ggH,LH,125,5,7.5)	800464	Py8_HtoSUEP_ggH_lephad_125_5p00_7p50	10 000
SUEP(ggH,LH,400,1.5,1)	800483	Py8_HtoSUEP_ggH_lephad_400_1p50_1p00	40 000
SUEP(ggH,LH,400,1.5,1.5)	800484	Py8_HtoSUEP_ggH_lephad_400_1p50_1p50	40 000
SUEP(ggH,LH,400,1.5,2.25)	800485	Py8_HtoSUEP_ggH_lephad_400_1p50_2p25	40 000
SUEP(ggH,LH,400,3,2)	800486	Py8_HtoSUEP_ggH_lephad_400_3p00_2p00	20 000
SUEP(ggH,LH,400,3,3)	800487	Py8_HtoSUEP_ggH_lephad_400_3p00_3p00	20 000
SUEP(ggH,LH,400,3,4.5)	800488	Py8_HtoSUEP_ggH_lephad_400_3p00_4p50	20 000
SUEP(ggH,LH,400,5,3.33)	800489	Py8_HtoSUEP_ggH_lephad_400_5p00_3p33	10 000
SUEP(ggH,LH,400,5,35,5)	800490	Py8_HtoSUEP_ggH_lephad_400_5p00_5p00	10 000
SUEP(ggH,LH,400,5,35,7.5)	800491	Py8_HtoSUEP_ggH_lephad_400_5p00_7p50	10 000
SUEP(ggH,LH,750,1.5,1)	800492	Py8_HtoSUEP_ggH_lephad_750_1p50_1p00	10 000
SUEP(ggH,LH,750,1.5,1.5)	800493	Py8_HtoSUEP_ggH_lephad_750_1p50_1p50	10 000
SUEP(ggH,LH,750,1.5,2.25)	800494	Py8_HtoSUEP_ggH_lephad_750_1p50_2p25	10 000
SUEP(ggH,LH,750,3,2)	800495	Py8_HtoSUEP_ggH_lephad_750_3p00_2p00	10 000
SUEP(ggH,LH,750,3,3)	800496	Py8_HtoSUEP_ggH_lephad_750_3p00_3p00	10 000
SUEP(ggH,LH,750,3,4.5)	800497	Py8_HtoSUEP_ggH_lephad_750_3p00_4p50	10 000
SUEP(ggH,LH,750,5,3.33)	800498	Py8_HtoSUEP_ggH_lephad_750_5p00_3p33	10 000
SUEP(ggH,LH,750,5,5)	800499	Py8_HtoSUEP_ggH_lephad_750_5p00_5p00	10 000
SUEP(ggH,LH,750,5,7.5)	800500	Py8_HtoSUEP_ggH_lephad_750_5p00_7p50	10 000
SUEP(ggH,L,125,1.5,1)	800501	Py8_HtoSUEP_ggH_lep_125_1p50_1p00	40 000
SUEP(ggH,L,125,1.5,1.5)	800502	Py8_HtoSUEP_ggH_lep_125_1p50_1p50	40 000
SUEP(ggH,L,125,1.5,2.25)	800503	Py8_HtoSUEP_ggH_lep_125_1p50_2p25	40 000
SUEP(ggH,L,125,5,3.33)	800504	Py8_HtoSUEP_ggH_lep_125_5p00_3p33	10 000
SUEP(ggH,L,125,5,5)	800505	Py8_HtoSUEP_ggH_lep_125_5p00_5p00	10 000
SUEP(ggH,L,125,5,7.5)	800506	Py8_HtoSUEP_ggH_lep_125_5p00_7p50	10 000
SUEP(ggH,H,400,1.5,1)	800519	Py8_HtoSUEP_ggH_had_400_1p50_1p00	40 000
SUEP(ggH,H,400,1.5,1.5)	800520	Py8_HtoSUEP_ggH_had_400_1p50_1p50	40 000
SUEP(ggH,H,400,1.5,2.25)	800521	Py8_HtoSUEP_ggH_had_400_1p50_2p25	40 000
SUEP(ggH,H,400,3,2)	800522	Py8_HtoSUEP_ggH_had_400_3p00_2p00	20 000
SUEP(ggH,H,400,3,3)	800523	Py8_HtoSUEP_ggH_had_400_3p00_3p00	20 000
SUEP(ggH,H,400,3,4.5)	800524	Py8_HtoSUEP_ggH_had_400_3p00_4p50	20 000
SUEP(ggH,H,400,5,3.33)	800525	Py8_HtoSUEP_ggH_had_400_5p00_3p33	10 000
SUEP(ggH,H,400,5,5)	800526	Py8_HtoSUEP_ggH_had_400_5p00_5p00	10 000
SUEP(ggH,H,400,5,7.5)	800527	Py8_HtoSUEP_ggH_had_400_5p00_7p50	10 000
SUEP(ggH,H,750,1.5,1)	800528	Py8_HtoSUEP_ggH_had_750_1p50_1p00	10 000
SUEP(ggH,H,750,1.5,1.5)	800529	Py8_HtoSUEP_ggH_had_750_1p50_1p50	10 000
SUEP(ggH,H,750,1.5,2.25)	800530	Py8_HtoSUEP_ggH_had_750_1p50_2p25	10 000
SUEP(ggH,H,750,3,2)	800531	Py8_HtoSUEP_ggH_had_750_3p00_2p00	10 000
SUEP(ggH,H,750,3,3)	800532	Py8_HtoSUEP_ggH_had_750_3p00_3p00	10 000
SUEP(ggH,H,750,3,4.5)	800533	Py8_HtoSUEP_ggH_had_750_3p00_4p50	10 000
SUEP(ggH,H,750,5,3.33)	800534	Py8_HtoSUEP_ggH_had_750_5p00_3p33	10 000
SUEP(ggH,H,750,5,5)	800535	Py8_HtoSUEP_ggH_had_750_5p00_5p00	10 000
SUEP(ggH,H,750,5,7.5)	800536	Py8_HtoSUEP_ggH_had_750_5p00_7p50	10 000

Abbreviations

pp proton–proton 1, 17

BS Beam-Spot 19

BSM beyond the Standard Model 39

CB Combined 45

CDM Cold Dark Matter 1, 11

CL Confidence Level 4

CR control region 29

CSC Cathode Strip Chamber 27

DM Dark Matter 1, 11

FCal Forward Calorimeter 25

HLT High-Level Trigger 20, 27

HV Hidden Valley 1, 13

IBL Insertable B-Layer 24

ID Inner Detector 21

IO Inside-Out combined 45

ISR initial state radiation 14

L1 Level 1 27

LAr Lead/Liquid Argon 25

LEP Large Electron Positron 17

LHC Large Hadron Collider 1, 17

LUCID-2 Luminosity Cherenkov Integrating Detector 2 19

MC Monte Carlo 28

MDT Monitored Drift Tube 27

MS Muon Spectrometer 21

PDF parton distribution function 28

pdf probability density function 31

PP0 Patch Panel 0 64

PV Primary Vertex 44

QCD quantum chromodynamics 2, 6

QFT quantum field theory 5

ROI region of interest 27

RPC Resistive Plate Chamber 27

SCT Silicon Microstip Tracker 25

SIDM Strongly-Interacting Dark Matter 12

SM Standard Model 1, 3

SR signal region 29

ST Segment-Tagged 45

SUEP Soft Unclusted Energy Pattern iii, v, 1, 14

TGC Thin Gap Chamber 27

TGC-EI TGC End-cap Inner 27

TGC-FI TGC Forward Inner 27

TRT Transition Radiation Tracker 25

vdM van der Meer 19

VR validation region 29

WIMP weakly interacting massive particle 12

Bibliography

[1] ATLAS Collaboration, "Observation of a new particle in the search for the standard model higgs boson with the ATLAS detector at the LHC," *Physics Letters B* **716** no. 1, (Sep, 2012) 1–29. https://doi.org/10.1016%2Fj.physletb.2012.08.020.

[2] CMS Collaboration, "Observation of a new boson at a mass of 125 GeV with the CMS experiment at the LHC," *Physics Letters B* **716** no. 1, (Sep, 2012) 30–61. https://doi.org/10.1016%2Fj.physletb.2012.08.021.

[3] ATLAS, CMS and LHCB Collaborations Collaboration, P. Azzurri, "Review of recent standard model measurements," tech. rep., CERN, Geneva, Sep, 2021. https://cds.cern.ch/record/2797541.

[4] L. Susskind, "Dynamics of spontaneous symmetry breaking in the weinberg-salam theory," *Phys. Rev. D* **20** (Nov, 1979) 2619–2625. https://link.aps.org/doi/10.1103/PhysRevD.20.2619.

[5] W. Adam and I. Vivarelli, "Status of searches for electroweak-scale supersymmetry after LHC run 2," *International Journal of Modern Physics A* **37** no. 02, (Jan, 2022) . https://doi.org/10.1142%2Fs0217751x21300222.

[6] M. J. Strassler and K. M. Zurek, "Echoes of a hidden valley at hadron colliders," *Physics Letters B* **651** no. 5-6, (Aug, 2007) 374–379. https://doi.org/10.1016%2Fj.physletb.2007.06.055.

[7] P. Schwaller, D. Stolarski, and A. Weiler, "Emerging jets," *Journal of High Energy Physics* **2015** no. 5, (May, 2015) . https://doi.org/10.1007%2Fjhep05%282015%29059.

[8] T. Cohen, M. Lisanti, and H. K. Lou, "Semivisible jets: Dark matter undercover at the LHC," *Physical Review Letters* **115** no. 17, (Oct, 2015) . https://doi.org/10.1103%2Fphysrevlett.115.171804.

[9] T. Han, Z. Si, K. M. Zurek, and M. J. Strassler, "Phenomenology of hidden valleys at hadron colliders," *Journal of High Energy Physics* **2008** no. 07, (Jul, 2008) 008–008. https://doi.org/10.1088%2F1126-6708%2F2008%2F07%2F008.

[10] M. Buschmann, J. Kopp, J. Liu, and P. A. N. Machado, "Lepton jets from radiating dark matter," *Journal of High Energy Physics* **2015** no. 7, (Jul, 2015) . https://doi.org/10.1007%2Fjhep07%282015%29045.

[11] J. Kang and M. A. Luty, "Macroscopic strings and ``quirks'' at colliders," *Journal of High Energy Physics* **2009** no. 11, (Nov, 2009) 065–065. https://doi.org/10.1088%2F1126-6708%2F2009%2F11%2F065.

[12] M. Rocha, A. H. G. Peter, J. S. Bullock, *et al.*, "Cosmological simulations with self-interacting dark matter – i. constant-density cores and substructure," *Monthly Notices of the Royal Astronomical Society* **430** no. 1, (Jan, 2013) 81–104. https://doi.org/10.1093%2Fmnras%2Fsts514.

[13] M. Cvetič, P. Langacker, and G. Shiu, "Phenomenology of a three-family standardlike string model," *Physical Review D* **66** no. 6, (Sep, 2002) . https://doi.org/10.1103%2Fphysrevd.66.066004.

[14] R. Barbieri, S. Ferrara, and C. Savoy, "Gauge models with spontaneously broken local supersymmetry," *Physics Letters B* **119** no. 4, (1982) 343–347. https://www.sciencedirect.com/science/article/pii/0370269382906852.

[15] M. Dine and A. E. Nelson, "Dynamical supersymmetry breaking at low energies," *Physical Review D* **48** no. 3, (Aug, 1993) 1277–1287. https://doi.org/10.1103%2Fphysrevd.48.1277.

[16] Z. Chacko, H.-S. Goh, and R. Harnik, "Natural electroweak breaking from a mirror symmetry," *Physical Review Letters* **96** no. 23, (Jun, 2006) . https://doi.org/10.1103%2Fphysrevlett.96.231802.

[17] J. Fan, M. Reece, and J. T. Ruderman, "Stealth supersymmetry," *Journal of High Energy Physics* **2011** no. 11, (Nov, 2011) . https://doi.org/10.1007%2Fjhep11%282011%29012.

[18] S. Knapen, S. P. Griso, M. Papucci, and D. J. Robinson, "Triggering soft bombs at the LHC," *Journal of High Energy Physics* **2017** no. 8, (Aug, 2017) . https://doi.org/10.1007%2Fjhep08%282017%29076.

[19] D. Hartill, D. Lüke, F. Pierre, and F. Vannucci, "Evidence for jet structure in hadron production by e+e- annihilation," *Physical Review Letters* **35** (12, 1975) .

[20] Y. Hatta and T. Matsuo, "Thermal hadron spectrum from gauge-string duality," *Physical Review Letters* **102** no. 6, (Feb, 2009) . https://doi.org/10.1103%2Fphysrevlett.102.062001.

[21] D. Turgeman, M. Pitt, I. Roth, and E. Duchovni, "On the modelling of energetic multi-jet QCD events," *The European Physical Journal C* **80** no. 12, (Dec, 2020) . https://doi.org/10.1140%2Fepjc%2Fs10052-020-08758-2.

[22] K. Cranmer, "Practical Statistics for the LHC," in *2011 European School of High-Energy Physics*, pp. 267–308. 2014. arXiv:1503.07622 [physics.data-an].

[23] I. C. Brock and T. Schorner-Sadenius, *Physics at the terascale.* Wiley, Weinheim, 2011. https://cds.cern.ch/record/1354959.

[24] M. E. Peskin and D. V. Schroeder, *An Introduction to quantum field theory.* Addison-Wesley, Reading, USA, 1995.

[25] A. Salam, *Weak and electromagnetic interactions*, pp. 244–254. https://www.worldscientific.com/doi/abs/10.1142/9789812795915_0034.

[26] F. Englert and R. Brout, "Broken symmetry and the mass of gauge vector mesons," *Phys. Rev. Lett.* **13** (Aug, 1964) 321–323. https://link.aps.org/doi/10.1103/PhysRevLett.13.321.

[27] P. W. Higgs, "Broken symmetries and the masses of gauge bosons," *Phys. Rev. Lett.* **13** (Oct, 1964) 508–509. https://link.aps.org/doi/10.1103/PhysRevLett.13.508.

[28] P. D. Group, P. A. Zyla, R. M. Barnett, *et al.*, "Review of Particle Physics," *Progress of Theoretical and Experimental Physics* **2020** no. 8, (08, 2020) , https://academic.oup.com/ptep/article-pdf/2020/8/083C01/34673722/ptaa104.pdf. https://doi.org/10.1093/ptep/ptaa104. 083C01.

[29] Z. Bern, *Quantum Field Theory in a Nutshell.* Physics Today, 2004. https://doi.org/10.1063/1.1752429. https://doi.org/10.1063/1.1752429.

[30] G. Hooft, "Renormalizable lagrangians for massive yang-mills fields," *Nuclear Physics B* **35** no. 1, (1971) 167–188. https://www.sciencedirect.com/science/article/pii/0550321371901398.

[31] C. N. Yang and R. L. Mills, "Conservation of isotopic spin and isotopic gauge invariance," *Phys. Rev.* **96** (Oct, 1954) 191–195. https://link.aps.org/doi/10.1103/PhysRev.96.191.

[32] D. P. A. Maurice, "The quantum theory of the electron," *Proceedings of the Royal Society A* **117** no. 778, (1928) .

[33] G. Dissertori, I. Knowles, and M. Schmelling, *Quantum Chromodynamics: High Energy Experiments and Theory*. Oxford University Press, 2009. https://oxford.universitypressscholarship.com/view/10.1093/acprof:oso/9780199566419.001.0001/acprof-9780199566419.

[34] M. Thomson, *Modern Particle Physics*. Cambridge University Press, 2013.

[35] K. G. Wilson, "Confinement of quarks," *Phys. Rev. D* **10** (Oct, 1974) 2445–2459. https://link.aps.org/doi/10.1103/PhysRevD.10.2445.

[36] S. Coleman and D. J. Gross, "Price of asymptotic freedom," *Phys. Rev. Lett.* **31** (Sep, 1973) 851–854. https://link.aps.org/doi/10.1103/PhysRevLett.31.851.

[37] F. Becattini, P. Castorina, J. Manninen, and H. Satz, "The thermal production of strange and non-strange hadrons in *ee*- collisions," *The European Physical Journal C* **56** no. 4, (Aug, 2008) 493–510. https://doi.org/10.1140%2Fepjc%2Fs10052-008-0671-x.

[38] E. Fermi, "High Energy Nuclear Events," *Progress of Theoretical Physics* **5** no. 4, (07, 1950) 570–583, `https://academic.oup.com/ptp/article-pdf/5/4/570/5430247/5-4-570.pdf`. https://doi.org/10.1143/ptp/5.4.570.

[39] R. Hagedorn, "Statistical thermodynamics of strong interactions at high energies," *Nuovo Cimento, Suppl.* **3** (1965) 147–186. https://cds.cern.ch/record/346206.

[40] F. Becattini, "An introduction to the statistical hadronization model," 2009. https://arxiv.org/abs/0901.3643.

[41] O. Aharony, S. S. Gubser, J. Maldacena, *et al.*, "Large n field theories, string theory and gravity," *Physics Reports* **323** no. 3-4, (Jan, 2000) 183–386. https://doi.org/10.1016%2Fs0370-1573%2899%2900083-6.

[42] D. Meschini, "Planck-scale physics: Facts and beliefs," *Foundations of Science* **12** no. 4, (Sep, 2006) 277–294. https://doi.org/10.1007%2Fs10699-006-9102-3.

[43] L. Allwicher, "*b*-physics anomalies: Eft analyses and simplified models," 2022. https://arxiv.org/abs/2201.04995.

[44] Muon g-2 Collaboration, "Measurement of the Positive Muon Anomalous Magnetic Moment to 0.46 ppm," *Phys. Rev. Lett.* **126** no. 14, (2021) 141801, `arXiv:2104.03281 [hep-ex]`.

[45] CDF Collaboration, "High-precision measurement of the w boson mass with the cdf ii detector," *Science* **376** no. 6589, (2022) 170–176. https://www.science.org/doi/abs/10.1126/science.abk1781.

[46] F. Zwicky, "Die rotverschiebung von extragalaktischen nebeln," *Helv. Phys. Acta* **6** no. 110–127, (1933) , `https://doi.org/10.1007/s10714-008-0706-5`. https://doi.org/10.1007/s10714-008-0706-5.

[47] S. M. Faber and R. E. Jackson, "Velocity dispersions and mass-to-light ratios for elliptical galaxies.," *apj* **204** (Mar., 1976) 668–683.

[48] A. N. Taylor, S. Dye, T. J. Broadhurst, *et al.*, "Gravitational lens magnification and the mass of abell 1689," *The Astrophysical Journal* **501** no. 2, (Jul, 1998) 539–553. https://doi.org/10.1086%2F305827.

[49] D. Clowe, M. Bradač, A. H. Gonzalez, *et al.*, "A direct empirical proof of the existence of dark matter," *The Astrophysical Journal* **648** no. 2, (Aug, 2006) L109–L113. https://doi.org/10.1086%2F508162.

[50] J. R. Primack, "Dark matter and structure formation in the universe," 1997. https://arxiv.org/abs/astro-ph/9707285.

[51] B. Pontecorvo, "Neutrino Experiments and the Problem of Conservation of Leptonic Charge," *Zh. Eksp. Teor. Fiz.* **53** (1967) 1717–1725.

[52] S. D. M. White, C. S. Frenk, and M. Davis, "Clustering in a neutrino-dominated universe," *apjl* **274** (Nov., 1983) L1–L5.

[53] P. J. E. Peebles, "Large-scale background temperature and mass fluctuations due to scale-invariant primeval perturbations," *apjl* **263** (Dec., 1982) L1–L5.

[54] G. Blumenthal, S. Faber, J. Primack, and et al., "Formation of galaxies and large-scale structure with cold dark matter," *Nature* **311** (1984) 517–525.

[55] M. Davis, G. Efstathiou, C. S. Frenk, and S. D. M. White, "The evolution of large-scale structure in a universe dominated by cold dark matter," *apj* **292** (May, 1985) 371–394.

[56] A. Einstein, "Cosmological Considerations in the General Theory of Relativity," *Sitzungsber. Preuss. Akad. Wiss. Berlin (Math. Phys.)* **1917** (1917) 142–152.

[57] A. H. Guth, "Inflationary universe: A possible solution to the horizon and flatness problems," *Phys. Rev. D* **23** (Jan, 1981) 347–356. https://link.aps.org/doi/10.1103/PhysRevD.23.347.

[58] P. J. E. Peebles and B. Ratra, "The cosmological constant and dark energy," *Reviews of Modern Physics* **75** no. 2, (Apr, 2003) 559–606. https://doi.org/10.1103%2Frevmodphys.75.559.

[59] and N. Aghanim, Y. Akrami, M. Ashdown, *et al.*, "Planck 2018 results," *Astronomy & Astrophysics* **641** (Sep, 2020) A6. https://doi.org/10.1051%2F0004-6361%2F201833910.

[60] R. J. Scherrer and M. S. Turner, "On the relic, cosmic abundance of stable, weakly interacting massive particles," *Phys. Rev. D* **33** (Mar, 1986) 1585–1589. https://link.aps.org/doi/10.1103/PhysRevD.33.1585.

[61] J. L. Feng and J. Kumar, "Dark-matter particles without weak-scale masses or weak interactions," *Physical Review Letters* **101** no. 23, (Dec, 2008) . https://doi.org/10.1103%2Fphysrevlett.101.231301.

[62] M. Bustamante, L. Cieri, and J. Ellis, "Beyond the Standard Model for Montaneros," in *5th CERN - Latin American School of High-Energy Physics*. 11, 2009. `arXiv:0911.4409 [hep-ph]`.

[63] D. H. Weinberg, J. S. Bullock, F. Governato, *et al.*, "Cold dark matter: Controversies on small scales," *Proceedings of the National Academy of Sciences* **112** no. 40, (Feb, 2015) 12249–12255. https://doi.org/10.1073%2Fpnas.1308716112.

[64] B. Moore, S. Ghigna, F. Governato, *et al.*, "Dark Matter Substructure within Galactic Halos," *apjl* **524** no. 1, (Oct., 1999) L19–L22, arXiv:astro-ph/9907411 [astro-ph].

[65] V. Avila-Reese, P. Colin, O. Valenzuela, *et al.*, "Formation and structure of halos in a warm dark matter cosmology," *The Astrophysical Journal* **559** no. 2, (Oct, 2001) 516–530. https://doi.org/10.1086/322411.

[66] A. Garzilli, A. Magalich, O. Ruchayskiy, and A. Boyarsky, "How to constrain warm dark matter with the Lyman-α forest," *Monthly Notices of the Royal Astronomical Society* **502** no. 2, (01, 2021) 2356–2363, https://academic.oup.com/mnras/article-pdf/502/2/2356/36218015/stab192.pdf. https://doi.org/10.1093/mnras/stab192.

[67] A. G. Cohen, D. B. Kaplan, and A. E. Nelson, "Progress in electroweak baryogenesis," *Annual Review of Nuclear and Particle Science* **43** no. 1, (Dec, 1993) 27–70. https://doi.org/10.1146%2Fannurev.ns.43.120193.000331.

[68] K. M. Zurek, "Asymmetric dark matter: Theories, signatures, and constraints," *Physics Reports* **537** no. 3, (Apr, 2014) 91–121. https://doi.org/10.1016%2Fj.physrep.2013.12.001.

[69] Y. Bai and P. Schwaller, "Scale of dark QCD," *Physical Review D* **89** no. 6, (Mar, 2014) . https://doi.org/10.1103%2Fphysrevd.89.063522.

[70] P. Langacker, "The physics of heavy gauge bosons," *Reviews of Modern Physics* **81** no. 3, (Aug, 2009) 1199–1228. https://doi.org/10.1103%2Frevmodphys.81.1199.

[71] S. Knapen, J. Shelton, and D. Xu, "Perturbative benchmark models for a dark shower search program," *Physical Review D* **103** no. 11, (Jun, 2021) . https://doi.org/10.1103%2Fphysrevd.103.115013.

[72] M. J. Strassler, "Why unparticle models with mass gaps are examples of hidden valleys," 2008. https://arxiv.org/abs/0801.0629.

[73] Y. Hatta and T. Matsuo, "Jet fragmentation and gauge/string duality," *Physics Letters B* **670** no. 2, (Dec, 2008) 150–153. https://doi.org/10.1016%2Fj.physletb.2008.10.043.

[74] O. S. Bruning, P. Collier, P. Lebrun, *et al.*, "LHC Design Report," *CERN Yellow Reports: Monographs* (2004) . https://cds.cern.ch/record/782076.

[75] ATLAS Collaboration, "The ATLAS Experiment at the CERN Large Hadron Collider," *JINST* **3** (2008) S08003.

[76] CMS Collaboration, "The CMS Experiment at the CERN LHC," *JINST* **3** (2008) S08004.

[77] LHCb Collaboration, "The LHCb Detector at the LHC," *JINST* **3** (2008) S08005.

[78] TOTEM Collaboration, "The TOTEM experiment at the CERN Large Hadron Collider," *JINST* **3** (2008) S08007.

[79] LHCf Collaboration, "LHCf experiment: Technical Design Report." LHCF-TDR-001, 2006. https://cds.cern.ch/record/926196.

[80] MoEDAL Collaboration, "Technical Design Report of the MoEDAL Experiment." MoEDAL-TDR-001, Jun, 2009. https://cds.cern.ch/record/1181486.

[81] M. Vretenar, J. Vollaire, R. Scrivens, *et al.*, "Linac4 design report," *CERN Yellow Reports: Monographs* **6** (2020) . https://cds.cern.ch/record/2736208.

[82] E. Mobs, "The CERN accelerator complex - 2019. Complexe des accélérateurs du CERN - 2019." CERN-GRAPHICS-2019-002, Jul, 2019. https://cds.cern.ch/record/2684277.

[83] ATLAS Collaboration, "Luminosity determination in pp collisions at $\sqrt{s}$ = 13 TeV using the ATLAS detector at the LHC." ATLAS-CONF-2019-021, Jun, 2019. https://cds.cern.ch/record/2677054.

[84] G. Avoni, M. Bruschi, G. Cabras, *et al.*, "The new LUCID-2 detector for luminosity measurement and monitoring in ATLAS," *JINST* **13** no. 07, (2018) P07017.

[85] S. van der Meer, "Calibration of the effective beam height in the ISR." CERN-ISR-PO-68-31, 1968. https://cds.cern.ch/record/296752.

[86] ATLAS Collaboration, "Luminosity determination in pp collisions at $\sqrt{s}$ = 8 TeV using the ATLAS detector at the LHC," *Eur. Phys. J. C* **76** no. 12, (2016) 653, arXiv:1608.03953 [hep-ex].

[87] CERN, "HL-LHC Project Schedule." cern.ch. https://project-hl-lhc-industry.web.cern.ch/content/project-schedule. Accessed: 2022-06-20.

[88] ATLAS Collaboration, "ATLAS Public Results - Luminosity Public Results Run 2,". https://twiki.cern.ch/twiki/bin/view/AtlasPublic/LuminosityPublicResultsRun2. Accessed: 2021-01-17.

[89] ATLAS Collaboration, "Characterization of Interaction-Point Beam Parameters Using the pp Event-Vertex Distribution Reconstructed in the ATLAS Detector at the LHC." ATLAS-CONF-2010-027, 2010. https://cds.cern.ch/record/1277659.

[90] The TOTEM Collaboration, . Antchev, P. Aspell, *et al.*, "First measurement of elastic, inelastic and total cross-section at $\sqrt{s}$ = 13 TeV by TOTEM and overview of cross-section data at LHC energies," 2017. https://arxiv.org/abs/1712.06153.

[91] ATLAS Collaboration, Z. Marshall, "Simulation of Pile-up in the ATLAS Experiment," *J. Phys. Conf. Ser.* **513** (2014) 022024.

[92] ATLAS Collaboration, "ATLAS detector and physics performance: Technical Design Report, 1." ATLAS-TDR-14, 1999. https://cds.cern.ch/record/391176.

[93] J. Pequenao, "Computer generated image of the whole ATLAS detector," Mar, 2008. https://cds.cern.ch/record/1095924.

[94] J. Pequenao, "Computer generated image of the ATLAS inner detector," Mar, 2008. https://cds.cern.ch/record/1095926.

[95] J. Pequenao, "Computer Generated image of the ATLAS calorimeter," Mar, 2008. https://cds.cern.ch/record/1095927.

[96] J. Pequenao, "Computer generated image of the ATLAS Muons subsystem," Mar, 2008. https://cds.cern.ch/record/1095929.

[97] ATLAS Collaboration, "ATLAS level-1 trigger: Technical Design Report." CERN-LHCC-98-014, 1998. https://cds.cern.ch/record/381429.

[98] ATLAS Collaboration, "ATLAS high-level trigger, data-acquisition and controls: Technical Design Report,". https://cds.cern.ch/record/616089.

[99] J. D. Bjorken and E. A. Paschos, "Inelastic electron-proton and γ-proton scattering and the structure of the nucleon," *Phys. Rev.* **185** (Sep, 1969) 1975–1982. https://link.aps.org/doi/10.1103/PhysRev.185.1975.

[100] B. Andersson, G. Gustafson, G. Ingelman, and T. Sjöstrand, "Parton fragmentation and string dynamics," *Physics Reports* **97** no. 2, (1983) 31–145. https://www.sciencedirect.com/science/article/pii/0370157383900807.

[101] T. Sjostrand, S. Mrenna, and P. Z. Skands, "PYTHIA 6.4 Physics and Manual," *JHEP* **05** (2006) 026, arXiv:hep-ph/0603175 [hep-ph].

[102] J. Bellm *et al.*, "Herwig 7.0/Herwig++ 3.0 release note," *Eur. Phys. J.* **C76** no. 4, (2016) 196, arXiv:1512.01178 [hep-ph].

[103] P. Biddulph and G. Thompson, "Improved modelling of independent parton hadronization," *Computer Physics Communications* **54** no. 1, (1989) 13–21. https://www.sciencedirect.com/science/article/pii/0010465589900283.

[104] GEANT4 Collaboration, "GEANT4: A Simulation toolkit," *Nucl. Instrum. Meth.* **A506** (2003) 250–303.

[105] K. Cranmer, "Statistical challenges for searches for new physics at the LHC," in *Statistical Problems in Particle Physics, Astrophysics and Cosmology*. Published by Imperial College Press and distributed by World Scientific Publishing Co., May, 2006. https://doi.org/10.1142%2F9781860948985_0026.

[106] G. Cowan, K. Cranmer, E. Gross, and O. Vitells, "Asymptotic formulae for likelihood-based tests of new physics," *The European Physical Journal C* **71** no. 2, (Feb, 2011) . https://doi.org/10.1140%2Fepjc%2Fs10052-011-1554-0.

[107] ATLAS Collaboration, "Muon reconstruction and identification efficiency in ATLAS using the full Run 2 pp collision data set at $\sqrt{s}$ = 13 TeV," *Eur. Phys. J. C* **81** no. 7, (2021) 578, arXiv:2012.00578 [hep-ex].

[108] ATLAS Collaboration, "Electron reconstruction and identification in the ATLAS experiment using the 2015 and 2016 LHC proton–proton collision data at $\sqrt{s}$ = 13 TeV," *The European Physical Journal C* **79** no. 8, (Aug, 2019) . https://doi.org/10.1140%2Fepjc%2Fs10052-019-7140-6.

[109] ATLAS Collaboration, "Search for microscopic black holes and string balls in final states with leptons and jets with the ATLAS detector at $\sqrt{s}$ = 8 TeV," *Journal of High Energy Physics* **2014** no. 8, (Aug, 2014) . https://doi.org/10.1007%2Fjhep08%282014%29103.

[110] CMS Collaboration, "Search for microscopic black hole signatures at the large hadron collider," *Physics Letters B* **697** no. 5, (Mar, 2011) 434–453. https://doi.org/10.1016%2Fj.physletb.2011.02.032.

[111] S. W. Hawking, "Particle Creation by Black Holes," *Commun. Math. Phys.* **43** (1975) 199–220. [Erratum: Commun.Math.Phys. 46, 206 (1976)].

[112] "Early Inner Detector Tracking Performance in the 2015 data at $\sqrt{s}$ = 13 TeV," tech. rep., CERN, Geneva, Dec, 2015. http://cds.cern.ch/record/2110140. All figures including auxiliary figures are available at https://atlas.web.cern.ch/Atlas/GROUPS/PHYSICS/PUBNOTES/ATL-PHYS-PUB-2015-051.

[113] ATLAS Collaboration Collaboration, Z. Zheng, "Identification of very-low transverse momentum muons with the ATLAS experiment," tech. rep., CERN, Geneva, Nov, 2018. https://cds.cern.ch/record/2649299.

[114] S. Knapen, "Suep generator," 2022. gitlab.com/simonknapen/suep_generator.

[115] B. Holdom, "Two u(1)'s and ϵ charge shifts," *Physics Letters B* **166** no. 2, (1986) 196–198. https://www.sciencedirect.com/science/article/pii/0370269386913778.

[116] S. Alekhin, W. Altmannshofer, T. Asaka, *et al.*, "A facility to search for hidden particles at the CERN SPS: the SHiP physics case," *Reports on Progress in Physics* **79** no. 12, (Oct, 2016) 124201. https://doi.org/10.1088%2F0034-4885%2F79%2F12%2F124201.

[117] M. Pospelov and A. Ritz, "Astrophysical signatures of secluded dark matter," *Physics Letters B* **671** no. 3, (Jan, 2009) 391–397. https://doi.org/10.1016%2Fj.physletb.2008.12.012.

[118] M. Endo, K. Hamaguchi, and G. Mishima, "Constraints on hidden photon models from electron g-2 and hydrogen spectroscopy," *Physical Review D* **86** no. 9, (Nov, 2012) . https://doi.org/10.1103%2Fphysrevd.86.095029.

[119] T. Sjöstrand, S. Ask, J. R. Christiansen, *et al.*, "An Introduction to PYTHIA 8.2," *Comput. Phys. Commun.* **191** (2015) 159–177, arXiv:1410.3012 [hep-ph].

[120] W. Lukas, "Fast Simulation for ATLAS: Atlfast-II and ISF," tech. rep., CERN, Geneva, Jun, 2012. https://cds.cern.ch/record/1458503.

[121] Particle Data Group, "Review of Particle Physics," *Prog. Theor. Exp. Phys* **2020** no. 8, (08, 2020) .

[122] C. T. Potter, H. Mantler, S. Lehti, *et al.*, "Handbook of lhc higgs cross sections: 3. higgs properties: Report of the lhc higgs cross section working group," 2013. http://cds.cern.ch/record/1559921.

[123] ATLAS Collaboration, "Improvements in $t\bar{t}$ modelling using NLO+PS Monte Carlo generators for Run 2." ATL-PHYS-PUB-2018-009, 2018. https://cds.cern.ch/record/2630327.

[124] ATLAS Collaboration, "Modelling of the $t\bar{t}H$ and $t\bar{t}V(V = W, Z)$ processes for $\sqrt{s} = 13$ TeV ATLAS analyses." ATL-PHYS-PUB-2016-005, 2016. https://cds.cern.ch/record/2120826.

[125] ATLAS Collaboration, "ATLAS simulation of boson plus jets processes in Run 2." ATL-PHYS-PUB-2017-006, 2017. https://cds.cern.ch/record/2261937.

[126] ATLAS Collaboration, "Multi-Boson Simulation for 13 TeV ATLAS Analyses." ATL-PHYS-PUB-2017-005, 2017. https://cds.cern.ch/record/2261933.

[127] ATLAS Collaboration, "The Pythia 8 A3 tune description of ATLAS minimum bias and inelastic measurements incorporating the Donnachie–Landshoff diffractive model." ATL-PHYS-PUB-2016-017, 2016. https://cds.cern.ch/record/2206965.

[128] ATLAS Collaboration, "Performance of the ATLAS muon triggers in run 2," *Journal of Instrumentation* **15** no. 09, (Sep, 2020) P09015–P09015. https://doi.org/10.1088%2F1748-0221%2F15%2F09%2Fp09015.

[129] R. Frühwirth, "Application of kalman filtering to track and vertex fitting," *Nuclear Instruments and Methods in Physics Research Section A: Accelerators, Spectrometers, Detectors and Associated Equipment* **262** no. 2, (1987) 444–450. https://www.sciencedirect.com/science/article/pii/0168900287908874.

[130] ATLAS Collaboration Collaboration, M. Capeans, G. Darbo, K. Einsweiller, *et al.*, "ATLAS Insertable B-Layer Technical Design Report," tech. rep., Sep, 2010. https://cds.cern.ch/record/1291633.

[131] ATLAS Collaboration, "Reconstruction of primary vertices at the ATLAS experiment in run 1 proton–proton collisions at the LHC," *The European Physical Journal C* **77** no. 5, (May, 2017) . https://doi.org/10.1140%2Fepjc%2Fs10052-017-4887-5.

[132] J. Illingworth and J. Kittler, "A survey of the hough transform," *Computer Vision, Graphics, and Image Processing* **44** no. 1, (1988) 87–116. https://www.sciencedirect.com/science/article/pii/S0734189X88800331.

[133] Y. H. Wang, "On the number of successes in independent trials," *Statistica Sinica* no. 03, . http://www3.stat.sinica.edu.tw/statistica/oldpdf/A3n23.pdf.

[134] ATLAS Collaboration, "ATLAS data quality operations and performance for 2015–2018 data-taking," *JINST* **15** (2020) P04003, arXiv:1911.04632 [physics.ins-det].

[135] OPAL Collaboration, "A measurement of charged particle multiplicity in $Z^0 \to c\bar{c}$ and $Z^0 \to b\bar{b}$ events," *Physics Letters B* **352** no. 1, (1995) 176–186. https://www.sciencedirect.com/science/article/pii/037026939500510R.

[136] ATLAS Collaboration, "Search for strong gravity in multijet final states produced in pp collisions at $$ \sqrt{s}=13 $$ TeV using the ATLAS detector at the LHC," *Journal of High Energy Physics* **2016** no. 3, (Mar, 2016) . https://doi.org/10.1007%2Fjhep03%282016%29026.

[137] M. Baak, G. J. Besjes, D. Côte, A. Koutsman, J. Lorenz, D. Short, "HistFitter software framework for statistical data analysis," *Eur. Phys. J.* **C75** (2015) 153, arXiv:1410.1280 [hep-ex].

[138] ATLAS Collaboration, "Performance of the ATLAS Trigger System in 2015," tech. rep., CERN, Geneva, Mar, 2016. https://cds.cern.ch/record/2140103.

[139] ATLAS Collaboration, "Topological cell clustering in the ATLAS calorimeters and its performance in LHC run 1," *The European Physical Journal C* **77** no. 7, (Jul, 2017) . https://doi.org/10.1140%2Fepjc%2Fs10052-017-5004-5.

[140] M. Cacciari, G. P. Salam, and G. Soyez, "The anti-k_t jet clustering algorithm," *JHEP* **04** (2008) 063, arXiv:0802.1189 [hep-ph].

[141] P. Liu, "Novel technique for luminosity measurement using 3D pixel modules in the ATLAS detector," tech. rep., CERN, Geneva, Sep, 2017. https://cds.cern.ch/record/2284010.

Acknowledgements

I want to start by expressing my gratitude towards Simone, Simon and Sascha, who ignited the SUEP analysis effort in ATLAS and accompanied me throughout my PhD. Thank you for the guidance and for answering all of my questions. I also want to thank Ece and Elena, with whom the analysis was developed. It was a pleasure working with all of you!

Thank you Sascha, for supervising my PhD and for all the advice and support I got from you. It was a lot of fun discussing physics with you, even though it could lead to quite a headache to try and figure out how SUEPs distribute in the inner detector.

I also want to thank my colleagues at the LMU for the great time I had there, and Michael, Thomas, Katrin, Fabian and Nikolai in particular, for proofreading this thesis.

A special thanks must also go to Dorothee, who woke my interest for particle physics with her interesting lectures and seminars. Your passion for the subject always showed and it was inspiring. Thank you for taking me down this rabbit hole.

Thank you also Otmar for everything you taught me, for all the interesting discussions, the support, and your positive attitude and pragmatism, which helped me in the most difficult times.

Most importantly, I want to thank my wife Katrin who supported my decision to start a PhD and, as a matter of fact, always supported anything that I wanted to do. During my PhD, you were the one needing support. But even then, all you wanted is to give and not take. The time I had with you was so precious. I am thankful for every minute I could spend with you.

I want to thank everyone who made it possible for me to pursue my PhD while also supporting the decisions I made in my private life. Thank you for the patience and kindness.